JUN 13 1958
ST. LOUIS

JOURNAL OF THE

# AERONAUTICAL SCIENCES

VOLUME 25 JUNE, 1958 NUMBER 6

## CONTENTS

The Interaction of Shock Waves and Turbulent Boundary Layers ..... ANDREW G. HAMMITT 345

The Laminar Free-Convective Heat Transfer From the Outer Surface of a Vertical Circular Cylinder ..... KNOX MILLSAPS AND KARL POHLHAUSEN 357

A Pilot Analog for Airplane Pitch Control ..... N. D. DIAMANTIDES 361

Theoretical Considerations of Flutter at High Mach Numbers ..... HOMER G. MORGAN, HARRY L. RUNYAN, AND VERA HUCKEL 371

Compressive Buckling of a Long Simply Supported Plate on an Elastic Foundation .... PAUL SEIDE 382

A Simple Method of Matric Structural Analysis: Part III—Analysis of Flexible Frames and Stiffened Cylindrical Shells ..... BERTRAM KLEIN 385

Readers' Forum ..... 395

*Published by*
INSTITUTE OF THE AERONAUTICAL SCIENCES, INC.

# JOURNAL OF THE AERONAUTICAL SCIENCES

*Editor:* W. R. Sears
*Director, Graduate School of Aeronautical Engineering, Cornell University*

*Associate Editor:* Robert R. Dexter *Managing Editor:* Rita J. Turino
*Editorial Assistant:* Caroline Taylor

## Editorial Committee

**Aerodynamics and Fluid Mechanics**

Holt Ashley
H. Julian Allen
Dean R. Chapman
Francis H. Clauser
Hugh L. Dryden
John C. Evvard
Antonio Ferri
Alexander Flax
Wallace D. Hayes
R. T. Jones
Carl Kaplan
H. W. Liepmann
C. C. Lin
H. F. Ludloff
Harold Luskin
Clark B. Millikan
Henry T. Nagamatsu
H. J. E. Reid
George S. Schairer
G. B. Schubauer
John Stack
Theodore Theodorsen
Arthur N. Tifford
Th. von Kármán

**Flight Testing**

R. R. Gilruth
Melvin N. Gough
W. L. Howland
W. F. Milliken, Jr.

**Rotating Wing Aircraft**

F. B. Gustafson
K. H. Hohenemser
Bartram Kelley
R. B. Maloy
Ralph McClarren
R. H. Miller
R. H. Prewitt
Igor I. Sikorsky

**Structures**

John E. Duberg
R. R. Heldenfels
N. J. Hoff
Samuel Levy
J. F. McBrearty
W. Ramberg
E. E. Sechler
F. R. Shanley
C. R. Strang
S. Timoshenko

**Meteorology**

C. F. Brooks
D. M. Little
F. W. Reichelderfer
K. C. Spengler

**Vibration and Flutter**

Lee Arnold
M. A. Biot
R. L. Bisplinghoff
Harold A. Cheilek
I. E. Garrick
Martin Goland

**Aircraft Design**

W. E. Beall
E. H. Heinemann
Hall L. Hibbard
Richard Hutton
C. L. Johnson
A. A. Kartveli
F. K. Teichmann

**Electronics**

K. C. Black
M. V. Kiebert, Jr.
David S. Little
Paul Rosenberg
Giles J. Strickroth

**Physiologic Problems**

H. G. Armstrong
Louis H. Bauer
Robert J. Benford
W. Randolph Lovelace, II
Ross A. MacFarland

**Flight Propulsion**

William Bollay
George W. Brady
R. P. Kroon
Frank E. Marble
Abe Silverstein
E. S. Taylor

**Instruments**

Alan G. Binnie
Charles H. Colvin
Frank R. Cook
C. S. Draper
S. G. Eskin
C. F. Savage
R. C. Sylvander

## SUBSCRIPTION RATES

Journal of the Aeronautical Sciences, Published Monthly. United States and Possessions: 1 Year, $15.00; Single Copies, $1.50. Foreign Countries Including Canada (American Currency Rates): 1 Year, $16.00; Single Copies, $1.50.

Aero/Space Engineering, Published Monthly. United States and Possessions: 1 Year, $5.00; Single Copies, $0.50. Foreign Countries Including Canada (American Currency Rates): 1 Year, $6.00; Single Copies, $0.50.

Notices of change of address should be sent to the Institute at least 30 days prior to actual change of address.

Manuscripts for publication, proofs, and all correspondence should be addressed to the Editorial Office of the Journal.

Publication Office, 20th and Northampton Sts., Easton, Pa. Correspondence regarding subscriptions may be addressed to the Editorial Office of the Journal of the Aeronautical Sciences, 2 East 64th Street, New York 21, N.Y.

© *Copyright, 1958, by the Institute of the Aeronautical Sciences, Inc.*

Second-Class Mail Privileges Authorized at Easton, Pa. Acceptance for mailing at a special rate of Postage provided for in the Act of August 24, 1912. Authorized April 29, 1937.

JOURNAL OF THE AERONAUTICAL SCIENCES

VOLUME 25 JUNE, 1958 NUMBER 6

# The Interaction of Shock Waves and Turbulent Boundary Layers†

ANDREW G. HAMMITT*

*Princeton University*

SUMMARY

An examination of experimental data on the interaction of shock waves with a turbulent boundary layer shows that the transport of mass and momentum between the free stream and the boundary layer are small. Based on this experimental evidence and the characteristics of a turbulent boundary layer, a theory is presented to predict the overall boundary-layer changes through an interaction. The calculated results compare favorably with the available experimental data.

SYMBOLS

$a$ = speed of sound
$A$ = parameter defined by Eq. (12a)
$f$ = average boundary-layer parameter
$I$ = momentum flux
$m$ = mass flux
$M$ = Mach Number
$p$ = pressure
$R$ = gas constant
$Re_\theta$ = Reynolds Number based on momentum thickness
$T$ = temperature
$u$ = velocity
$w$ = nondimensional velocity
$\beta$ = shock-wave angle
$\gamma$ = specific heat ratio
$\delta$ = boundary-layer thickness
$\theta$ = deflection angle of flow
$\kappa$ = average boundary-layer parameter
$\rho$ = density

***Subscripts and Superscripts***

1 = conditions ahead of interaction
2 = conditions behind interaction
0 = incompressible
$e$ = condition at edge of boundary layer
$i$ = condition between two shock waves
$s$ = stagnation
$u$ = undisturbed
$(\bar{})$ = average condition for boundary layer

Received April 5, 1957. Revised and received February 26, 1958.

† This work was carried out at the Gas Dynamics Laboratory, Princeton University, under Air Force Contract No. AF 18(600)-498.

* Research Associate, Gas Dynamics Laboratory.

## INTRODUCTION

THE BEHAVIOR of boundary layers in flows with pressure gradients has been the subject of many investigations. Some theoretical solutions are available for both the laminar incompressible and compressible boundary layers, but there are none for either case of the turbulent boundary layer; however, a considerable body of experimental data from measurements on the incompressible turbulent boundary layers forms the basis for several semiempirical turbulent theories. Some attempts to extend these theories to compressible turbulent layers have been made but the lack of experimental data hampers these extrapolations.

An important case in which a supersonic boundary layer is subject to an adverse pressure gradient occurs when a shock wave approaches a solid boundary. This problem has been the subject of considerable experimental investigation. The rapid pressure rise which takes place is the distinguishing feature of the shock-wave-boundary-layer interaction and makes it somewhat different from the usual boundary-layer problem. The main differences are that the pressure forces acting on the boundary layer are much larger than the usual values associated with the shear forces at the wall and at the outer edge of the boundary layer, and the pressure gradient normal to the wall may be large through the interaction region.

Several analyses have been presented considering the problem of separation of a boundary layer on a flat surface.[1–6] Results which correlate reasonably well with the interactions in front of forward facing steps have been found. However, it has not been possible by these techniques to predict the higher pressure ratios experienced without separation in the flow in concave corners and through incident-reflected shock configurations.

Because of the large normal pressure gradients, the boundary-layer approximations cannot be applied in

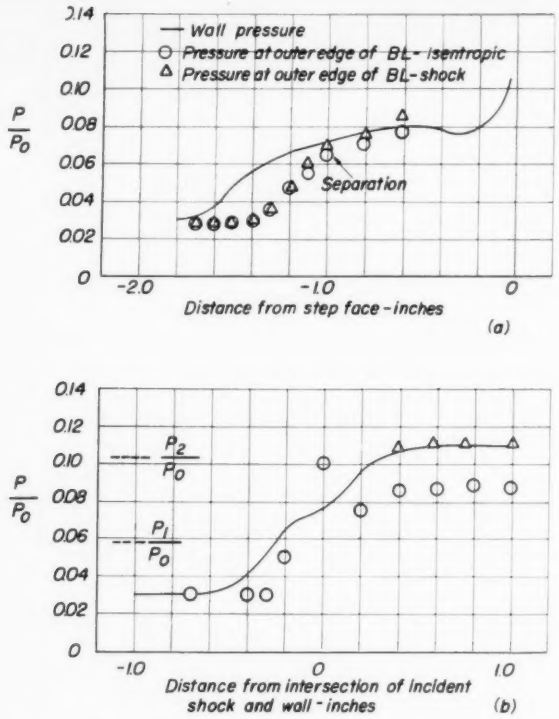


FIG. 1. Static pressures on the wall and at the outer edge of the boundary layer. (a) Forward-facing step, $M=2.92$; (b) incident-reflected shock wave, $M=2.92$.

the interaction region; however, some simplification can be made based on the relative magnitude of pressure forces and shear forces. Some experimental data are available which can be used to test the validity of these basic assumptions when applied to the various interaction configurations. These experimental results can be used to determine where the boundary-layer assumptions may be applied and the importance of shear forces through the interaction region. Based on these results, an analytical treatment of these shock-wave-boundary-layer configurations can be developed.

## Analysis of Experiments

The experimental investigations of shock-wave - boundary-layer interactions have shown several interesting features. If a boundary layer is caused to separate by placing a forward-facing step along a wall, there appears to be a characteristic pressure rise associated with this separation. However, if a given pressure rise is imposed on the boundary layer, by a shock wave impinging and reflecting from the wall, pressure ratios in excess of the separation pressure ratio found in front of a forward facing step can be obtained without separation. When separation does occur, it is limited to a small region followed by reattachment. Also, for the case of an interaction caused by a concave corner, pressure ratios without separation in excess of the separation pressure ratio for a forward-facing step seem to be possible. Some experimental studies of the flow in front of the forward-facing step and through an incident-reflected shock wave are available which are useful in arriving at an understanding of the mechanism involved in these interactions.

In references 9, 11, 16, and 19, the results of several boundary-layer total head surveys have been presented through some shock-wave - boundary-layer interaction configurations. These surveys are for forward-facing steps at $M = 2.3$, 2.92, and 3.85 and for an incident-reflected type shock wave interaction at $M = 2.92$. The first step in interpreting these results is to determine the variation of static pressure across the boundary layer. The static pressure outside of the boundary layer may be inferred from the total head tube readings, if the local stagnation pressure is known. The static pressures at the outside edge of the layer have been calculated under the assumption that the flow up to the point considered obeyed (1) the isentropic law and (2) the oblique shock law. The results of such calculations for the step and shock-wave case at $M = 2.92$ are shown in Fig. 1. These results are typical of the other two Mach Numbers. This Figure shows that the static pressure across the boundary layer is approximately constant before and beh nd the interaction region but may vary by factors of two or more in the interaction region. The static pressure calculated by considering the stagnation pressure losses through the shock waves are in much better agreement with the wall static pressures measured behind the interaction region, especially in the case of the incident-reflected shock interaction.

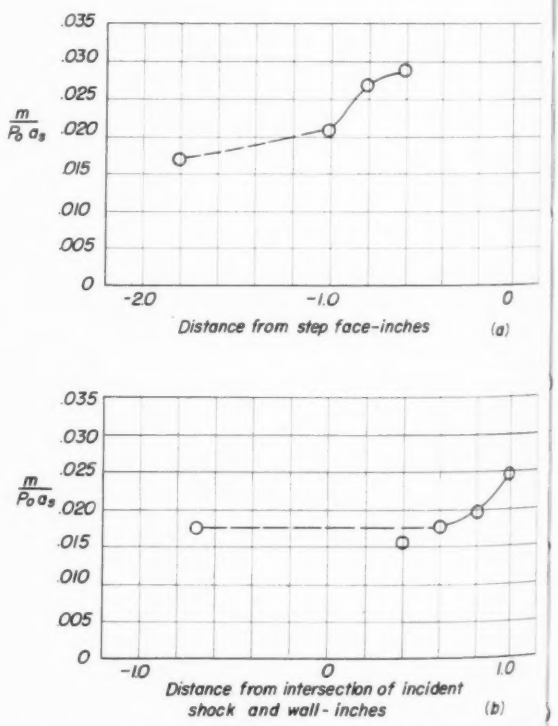


FIG. 2. Mass flow in boundary layer through shock-wave interactions. (a) Forward-facing step, $M=2.92$; (b) incident-reflected shock wave, $M=2.92$.

An analysis of the mass and momentum in the boundary layer on each side of the interaction can be made based on these boundary-layer surveys. The mass in the boundary layer through the interaction region for both the case of the step and shock wave is shown in Fig. 2. This Figure shows that the change of mass in the boundary layer is relatively small. If the momentum in the stream tube comprising the initial boundary layer is calculated, the results shown in Fig. 3 are found. The momentum change in the stream tube is caused both by shear forces and the component of the pressure forces acting on the outside streamline in the direction along the wall. If the step type pressure distribution shown in Fig. 5 is assumed, the pressure contribution may be subtracted out. These flow models are based on a study of surface pressure distributions and schlieren pictures such as those shown in Fig. 4. The corrected curves, in Fig. 3 show that there is very little momentum change due to shear forces in this stream tube.

This analysis of the experiments suggests that it may be possible to treat the shock-wave - turbulent boundary-layer interaction in the following way. The dissipative flow is considered as a boundary layer in the regions both before and behind the interaction. The equations of conservation of mass and momentum between these two regions are satisfied in the absence of mass or momentum transfer from the free stream or the wall. A flow model of the type shown in Fig. 5 is adopted to give the pressure distribution along the outer edge of the boundary layer.

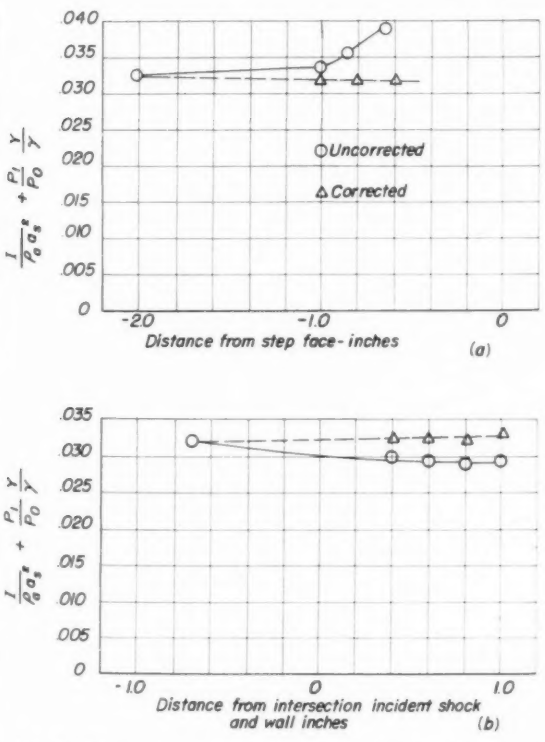


FIG. 3. Momentum in boundary layer through shock-wave interactions. (a) Forward-facing step, $M=2.92$; (b) incident-reflected shock wave, $M=2.92$.

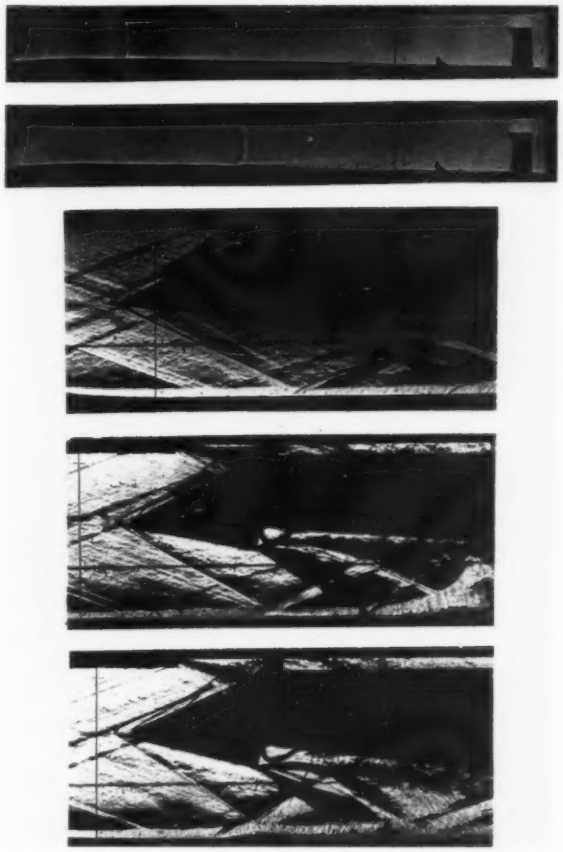

FIG. 4. Schlieren pictures of shock-wave interactions. *Top to bottom:* (a) weak normal shock, $M=1.2$; (b) strong normal shock $M=1.35$; (c) weak oblique shock, $M=2.92$, $\theta=7°$; (d) medium oblique shock, $M=2.92$, $\theta=9°$; (e) strong oblique shock, $M=2.92$, $\theta=12°$.

This method neglects the skin friction and the mass and momentum transfer along the outer edge of the boundary layer, but does not restrict the shear forces between adjacent parts of the boundary layer. Further analysis of the experimental results shows that, while there appears to be little momentum transfer in the outer part of the boundary layer, relatively important momentum transfer occurs in the inner part of the layer. However, if average parameters are used to represent the boundary layer, this shear distribution within the layer need not be considered in detail.

## Boundary-Layer Representation

The parameters which will be used to represent the boundary layer are those introduced in reference 22. An average velocity in the boundary layer is defined as the ratio of the momentum to the mass $\bar{u} = I/m$. A quantity $\kappa$ is now defined as the ratio of $\bar{u}$ to $u_e$, the free-stream velocity, $\kappa = \bar{u}/u_e$. A mean density and mean temperature may be defined by the continuity relation and equation of state

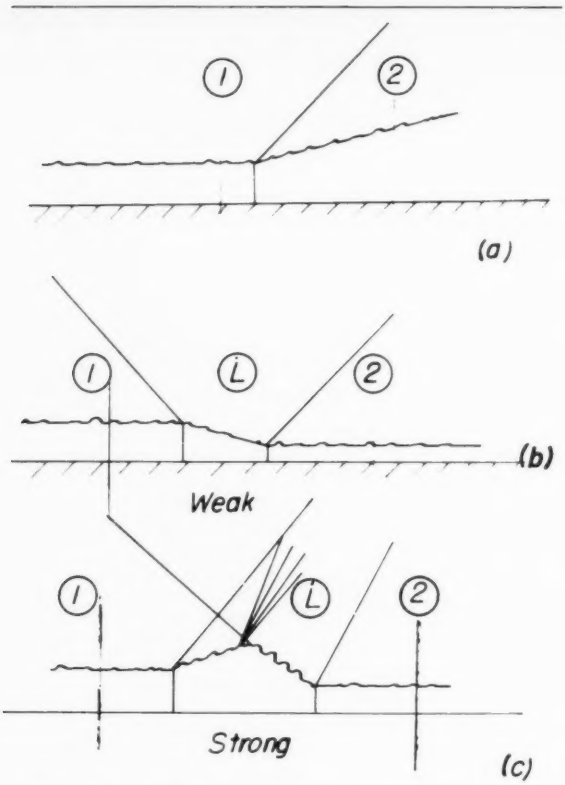


FIG. 5. Shock-wave boundary-layer models used for calculating momentum changes in the boundary layer. (a) Forward facing step; (b) weak incident-reflected wave; (c) strong incident-reflected wave.

$$m = \bar{\rho}\bar{u}\delta = p\bar{u}\delta/R\bar{T}$$

The quantity $f$ is introduced to satisfy the relation

$$\bar{T}/T_s = f - [(\gamma - 1)/2]\bar{w}^2 = f - [(\gamma - 1)/2]\kappa^2 w_e^2$$

where $w = u/a_s$. The quantities $f$ and $\kappa$ are the two parameters which will be used to describe the boundary layer.

In order to determine the boundary-layer conditions behind the interaction region, an additional relation is needed. The available experimental data give some suggestions on what this relation should be. If schlieren pictures of relatively weak interactions are examined, Figs. 4(a) and 4(c), it can be seen that the changes appear to take place in finite jumps over most of the boundary layer, and that the edge of the boundary layer may be turned, but not displaced, through these discontinuities. These observations suggest that these waves may be treated in an analogous way to shock waves in uniform flow if average properties are used to describe the boundary layer. If this type of model is adopted, it is the same as prescribing the boundary-layer thickness behind the interaction. Such a model might be expected to be correct for the cases of shock-wave interactions of insufficient strength to separate the layer.

Once separation occurs, Fig. 4(e), the location of the shock waves bears no simple relation to the location of the incident shock wave or to the contour of the wall. The streamline contours are free to adjust themselves to form a shock pattern or pressure distribution compatible with the boundary-layer requirements. For this case, many of the changes do not appear to take place in finite jumps but in a continuous manner. The interactions spread out over sufficient distance so that the boundary-layer thickness can change. For this case, the discontinuity assumption is not appropriate and no assumption can be made about the boundary-layer thickness.

Many measurements have been made of incompressible turbulent boundary layers under pressure gradients. These measurements show a tendency for the boundary layer to follow a certain class of profile. To a reasonable approximation, it has been possible to describe these profiles by a single parameter. The shear forces within the layer, when given sufficient time, create a boundary-layer profile similar to the equilibrium profiles. If pressure changes occur very quickly, as in a discontinuous jump, the boundary-layer profile can be radically altered from the equilibrium profile; but when the pressure changes occur more gradually, there is a better chance of profiles similar to equilibrium profiles.

For the case where separation occurs, the boundary layer may have a chance to approach the one-param-

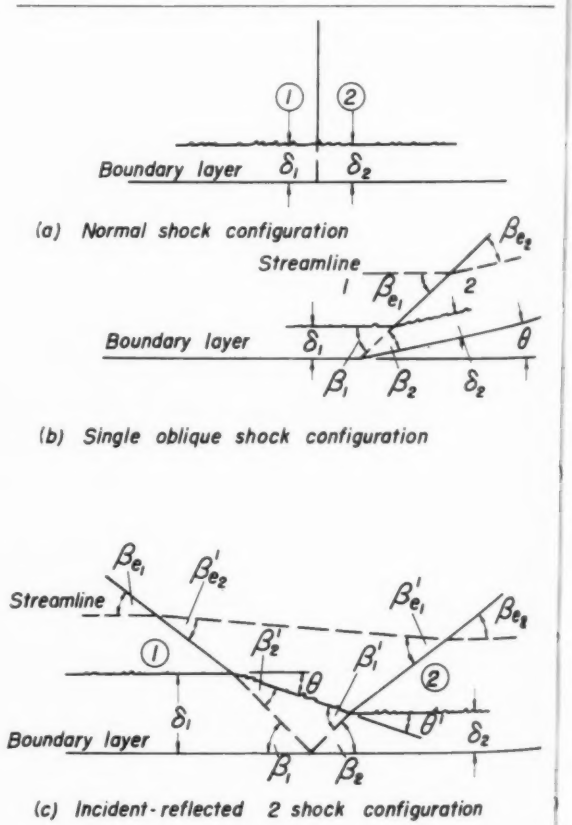


FIG. 6. Shock-wave boundary-layer models for discontinuity analysis.

eter family, and this assumption will be made. For the weaker shocks, where a discontinuity exists, and location of the edge of the boundary layer can be fairly well fixed, all empirical assumption of the shape of the profile is not necessary. However, for the cases when separation occurs, the location of the edge of the boundary layer cannot be specified.

## Discontinuity Analysis

The discontinuity analysis can be made for both normal and oblique shock waves impinging on the boundary layer. Equations analogous to the shock-wave equations may be developed using the average boundary-layer parameters. If the pressure, flow direction, and velocity at the edge of the boundary layer are now assumed equal to the free-stream conditions, the equations developed can be used to determine the boundary-layer parameters $f$ and $\kappa$ behind the interaction.

## Normal Shock

The general configuration and notation considered for the normal shock analysis are shown in Fig. 6(a). In terms of the average parameters, the continuity equation may be written

$$\frac{p_1}{p_2} = \frac{\{f_1 - [(\gamma-1)/2]\kappa_1^2 w_{e_1}^2\}}{\{f_2 - [(\gamma-1)/2]\kappa_2^2 w_{e_2}^2\}} \left(\frac{\kappa_2 w_{e_2}}{\kappa_1 w_{e_1}}\right) \tag{1}$$

since $\delta_1 = \delta_2$ for the normal shock configuration.

The momentum equation becomes

$$I_1 + p_1\delta_1 = I_2 + p_2\delta_2$$

and may be reduced to the form

$$\frac{p_1}{p_2} = \frac{\{f_1 - [(\gamma-1)/2]\kappa_1^2 w_{e_1}^2\}}{\{f_2 - [(\gamma-1)/2]\kappa_2^2 w_{e_2}^2\}} \times \frac{\{\gamma\kappa_2^2 w_{e_2}^2 + f_2 - [(\gamma-1)/2]\kappa_2^2 w_{e_2}^2\}}{\{\gamma\kappa_1^2 w_{e_1}^2 + f_1 - [(\gamma-1)/2]\kappa_1^2 w_{e_1}^2\}} \tag{2}$$

Eqs. (1) and (2) may be combined to give

$$\frac{\gamma+1}{2}\kappa_1 w_{e_1}\kappa_2 w_{e_2} = \frac{f_2\kappa_1 w_{e_1} - f_1\kappa_2 w_{e_2}}{\kappa_1 w_{e_1} - \kappa_2 w_{e_2}} \tag{3}$$

If $f_1$ and $f_2$, $\kappa_1$ and $\kappa_2 = 1$, this relation reduces to the classic velocity relation across the normal shock,

$$[(\gamma+1)/2] w_{e_1} w_{e_2} = 1 \tag{4}$$

By substituting Eq. (4) in Eq. (1) and setting $f_1$, $f_2$, $\kappa_1$ and $\kappa_2 = 1$,

$$\frac{p_2}{p_1} = \frac{[(\gamma+1)/2] w_{e_1}^2 - [(\gamma-1)/(\gamma+1)]}{1 - [(\gamma-1)/2] w_{e_1}^2} \tag{5}$$

If the pressure is required to be equal to the free-stream value and the boundary-layer properties are based on the free-stream velocity, Eqs. (4) and (5) may now be used to eliminate $w_{e_2}$ and $p_2$ in Eqs. (1) and (2), and these two relations may be solved simultaneously for $f_2$ and $\kappa_2$. When this process is carried through,

$$\frac{\kappa_2}{\kappa_1} = \frac{[(\gamma+1)/2]\{1 - [(\gamma-1)/2] w_{e_1}^2\}\{w_{e_1}^2 + [2/(\gamma+1)](f_1/\kappa_1^2)\} - \{[(\gamma+1)/2] w_{e_1}^2 - [(\gamma-1)/(\gamma+1)]\}\{(f_1/\kappa_1^2) - [(\gamma-1)/2] w_{e_1}^2\}}{[2\gamma/(\gamma+1)]\{1 - [(\gamma-1)/2] w_{e_1}^2\}} \tag{6}$$

$$f_2/\kappa_2^2 = (\kappa_1/\kappa_2) + [2/(\gamma+1)](1/w_{e_1}^2)[(\kappa_1 f_1/\kappa_2\kappa_1^2) - 1] \tag{7}$$

These relations define the boundary-layer parameters behind the normal shock.

## Oblique Shock

The development for the oblique shock is similar to that used in the case of the normal shock. An average angle of the shock wave within the boundary layer and an average flow deflection angle are defined in the usual way. The requirement is imposed that the boundary-layer flow deflection angle equals the external flow deflection angle, and that the pressure in the boundary layer is equal to the free-stream pressure. No restriction is placed on the average boundary-layer shock-wave angle. This general oblique shock configuration is shown in Fig. 6(b). The integration required to obtain the average boundary-layer parameters is always performed perpendicular to the streamlines.

The continuity equation may now be written

$$\frac{p_2}{p_1} = \left(\frac{f_1 - [(\gamma-1)/2]\kappa_1^2 w_{e_1}^2}{f_2 - [(\gamma-1)/2]\kappa_2^2 w_{e_2}^2}\right)\left(\frac{\kappa_2 w_{e_2}\sin\beta_2}{\kappa_1 w_{e_1}\sin\beta_1}\right) \tag{8}$$

and the momentum equation normal to the discontinuity

$$\frac{p_1}{p_2} = \left(\frac{\gamma\kappa_2^2 w_{e_2}^2\sin^2\beta_2 + f_2 - [(\gamma-1)/2]\kappa_2^2 w_{e_2}^2}{\gamma\kappa_1^2 w_{e_1}^2\sin^2\beta_1 + f_1 - [(\gamma-1)/2]\kappa_1^2 w_{e_1}^2}\right)\left(\frac{f_1 - [(\gamma-1)/2]\kappa_1^2 w_{e_1}^2}{f_2 - [(\gamma-1)/2]\kappa_2^2 w_{e_2}^2}\right) \tag{9}$$

These equations, with the additional fact that the velocity parallel to the discontinuity is preserved, may be combined to give

$$\kappa_1 w_{e_1}\sin\beta_1\kappa_2 w_{e_2}\sin\beta_2 = [2/(\gamma+1)]A - [(\gamma-1)/(\gamma+1)]\kappa_1^2 w_{e_1}^2\cos^2\beta_1 \tag{10}$$

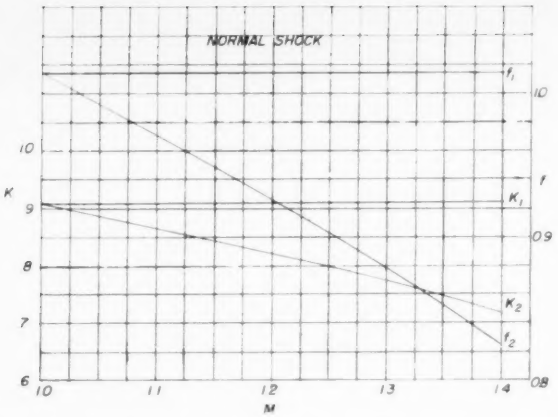


FIG. 7. Boundary-layer parameters behind normal shock.

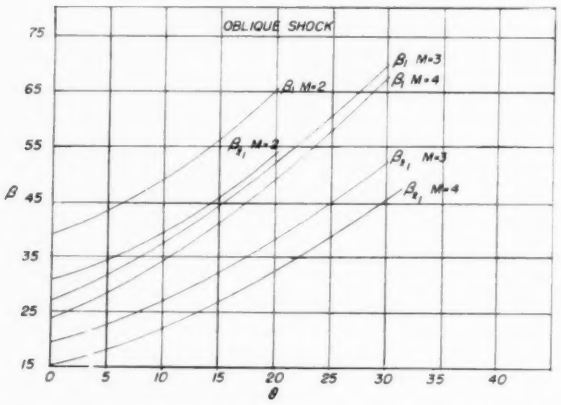


FIG. 8. Boundary-layer and free-stream shock-wave angles for oblique shock.

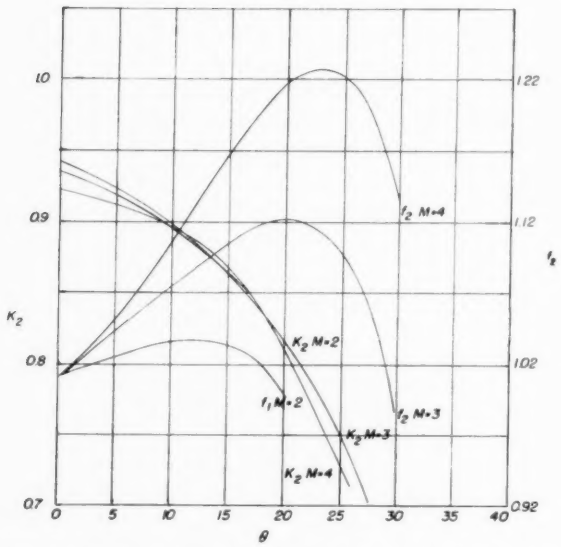


FIG. 9. Boundary-layer parameters behind oblique shocks as a function of deflection angle.

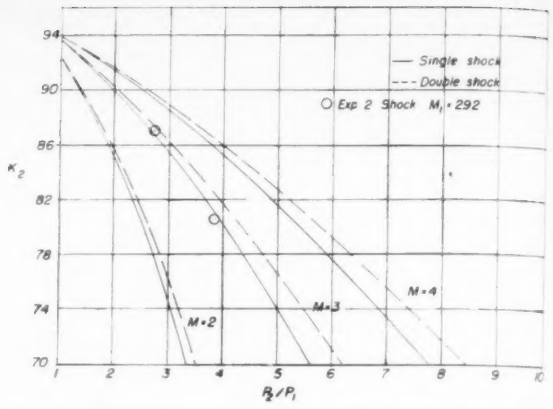


FIG. 10. Boundary-layer parameter behind single and double oblique shocks as a function of pressure ratio.

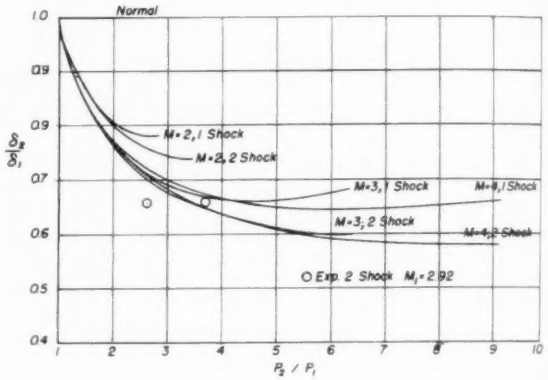


FIG. 11. Boundary-layer thickness behind single and double oblique shocks as a function of pressure ratio.

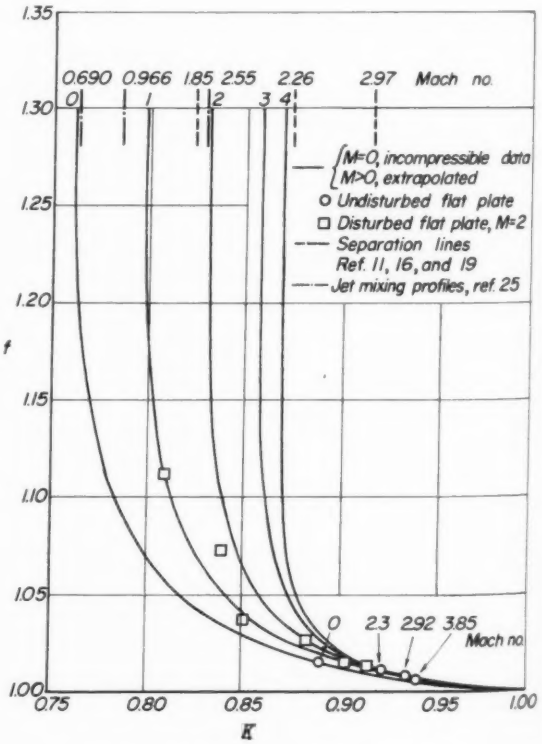


FIG. 12. $f$-$\kappa$ curves based on empirical data.

$$\frac{p_2}{p_1} = \left(\frac{\kappa_1 w_{e_1}^2 \sin^2 \beta_1}{f_1 - [(\gamma-1)/2]\kappa_1^2 w_{e_1}^2}\right)\left\{\frac{\gamma+1}{2}\left(\frac{f_2 - [(\gamma-1)/2]\kappa_1^2 w_{e_1}^2 \cos^2\beta_1}{A - [(\gamma-1)/2]\kappa_1^2 w_{e_1}^2 \cos^2\beta_1}\right) - \frac{(\gamma-1)^2}{2(\gamma+1)}\right\} - \frac{\gamma-1}{\gamma+1}\left(\frac{A - [(\gamma-1)/2]\kappa_1^2 w_{e_1}^2}{f_1 - [(\gamma-1)/2]\kappa_1^2 w_{e_1}^2}\right) \tag{11}$$

$$\tan\theta = \frac{2\left(\kappa_1^2 w_{e_1}^2 \sin\beta_1 \cos\beta_1 - \left\{A - [(\gamma-1)/2]\kappa_1^2 w_{e_1}^2\right\}\cot\beta_1\right)}{2\left\{A - [(\gamma-1)/2]\kappa_1^2 w_{e_1}^2\right\} + \kappa_1^2 w_{e_1}^2(\gamma + 1 - 2\sin^2\beta_1)} \tag{12}$$

where

$$A = \frac{f_2\kappa_1 w_{e_1}\sin\beta_1 - f_1\kappa_2 w_{e_2}\sin\beta_2}{\kappa_1 w_{e_1}\sin\beta_1 - \kappa_2 w_{e_2}\sin\beta_2} \tag{12a}$$

These relations reduce to the usual relations for the inviscid flow with the $f$'s and $\kappa$'s equal to 1.

$$w_{e_1}\sin\beta_{e_1} w_{e_2}\sin\beta_{e_2} = [2/(\gamma+1)] - [(\gamma-1)/(\gamma+1)]w_{e_1}^2\cos\beta_{e_1} \tag{13}$$

$$\frac{p_2}{p_1} = \frac{2\gamma}{\gamma+1}\frac{w_{e_1}^2\sin^2\beta_{e_1}}{1 - [(\gamma-1)/2]w_{e_1}^2} - \frac{\gamma-1}{\gamma+1} \tag{14}$$

$$\tan\theta = \frac{2(w_{e_1}^2\sin\beta_{e_1}\cos\beta_{e_1} - \left\{1 - [(\gamma-1)/2]w_{e_1}^2\right\}\cot\beta_{e_1})}{2\left\{1 - [(\gamma-1)/2]w_{e_1}^2\right\} + w_{e_1}^2(\gamma + 1 - 2\sin^2\beta_{e_1})} \tag{15}$$

The quantities $w_{e_2}$, $p_2$, and $\theta$ from Eqs. (13), (14), and (15) may now be substituted into Eqs. (10), (11), and (12). The unknowns $\beta_1$, $f_2$, and $\kappa_2$ may be determined by the remaining three equations

$$\frac{\cot\beta_1}{\cot\beta_{e_1}} = \left\{\frac{(\gamma+1)\kappa_1^2 w_{e_1}^2\left\{\frac{1 - [(\gamma-1)/2]w_{e_1}^2}{f_1 - [(\gamma-1)/2]\kappa_1^2 w_{e_1}^2}\right\} - 2w_{e_1}^2\sin\beta_{e_1} - (\gamma-1)w_{e_1}^2 + 2}{(\gamma+1)w_{e_1}^2 - 2w_{e_1}^2\sin^2\beta_{e_1} - (\gamma-1)w_{e_1}^2 + 2}\right\} \tag{16}$$

$$\frac{\kappa_2}{\kappa_1} = \left(1 - \frac{p_2}{p_1}\right)\frac{(f_1/\kappa_1^2) - [(\gamma-1)/2]w_{e_1}^2}{\gamma w_{e_1}\sin\beta_1 w_{e_2}\sin\beta_2} + \frac{w_{e_1}\sin\beta_1}{w_{e_2}\sin\beta_2} \tag{17}$$

$$\frac{f_2}{\kappa_2^2} = \frac{\gamma+1}{2}\frac{\kappa_1}{\kappa_2}w_{e_1}\sin\beta_1 w_{e_2}\sin\beta_2 - \frac{\gamma+1}{2}w_{e_2}^2\sin\beta_2^2 + \frac{\gamma-1}{2}\left(\frac{\kappa_1}{\kappa_2}\right)^2 w_{e_1}^2\cos^2\beta_1 + \frac{\kappa_1}{\kappa_2}\left(\frac{f_1}{\kappa_1^2} - \frac{\gamma-1}{2}w_{e_1}^2\cos^2\beta_1\right)\frac{w_{e_2}\sin\beta_1}{w_{e_1}\sin\beta_2} \tag{18}$$

Eqs. (13), (14), and (15) provide the relations for the external flow and for a given external shock wave. Eqs. (16), (17), and (18) may be used to calculate the change in boundary-layer average properties.

## Calculations

Using Eqs. (6) and (7) the boundary-layer parameters behind a normal shock wave have been calculated. The variation of these parameters is shown in Fig. 7. The calculation has been performed in the region of Mach Number 1.0 to 1.4, the range in which the experiments indicate that this configuration is likely to occur. The initial boundary-layer parameters as a function of Mach Number have been chosen equal to the values found for flat plate boundary layers shown in Fig. 13.

A similar calculation has been made for the oblique shock case, and the results are shown in Figs. 8 to 11. The initial value of the boundary-layer parameters is again taken from Fig. 13. Fig. 8 shows the variation of $\beta_1$ and $\beta_{e_1}$ with shock deflection angle $\theta$. This Figure shows that the boundary-layer shock-wave angle is always somewhat greater than the shock-wave angle in the free stream. This result is expected since the average Mach Number is lower in the boundary layer. Fig. 9 shows the effects of $f$ and $\kappa$ for various deflection angles and Mach Numbers. Fig. 10 is a similar plot of $\kappa$ against pressure ratio at various Mach Numbers. This plot shows both the case of a single shock and an incident-reflected shock. The initial parameters for the reflected shock are taken equal to the parameters behind the incident shock, and the deflection angles through the two shocks are taken equal but of opposite signs. This configuration is shown in Fig. 6(c). The calculation shows that the effect on the boundary layer is almost the same for the one or two shock configurations if the same overall pressure ratio is obtained. This result is similar to the result for the free stream, as might be expected considering the similarity of the equations, where the difference between one and two shock systems is small when the shocks are weak.

Fig. 11 shows the change in boundary-layer thickness caused by the various shock configurations. A change in boundary-layer thickness is only possible for the oblique shocks and is caused by the change in direction of the flow. The boundary layer becomes thinner in every case in the range considered, except for the normal shock. The calculations have been limited to this range since the experiments indicate that the assumed shock configurations are incorrect at greater shock strengths. As the later discussion will show, the analysis is probably in error for the stronger shock strengths which are shown in these Figures.

TABLE 1
Properties of the Flat Plate Boundary Layer at Variable $M$

| $M$ | $Re_\theta$ | $\kappa$ | $f$ | Reference |
|---|---|---|---|---|
| 2.3 | 17.1 ($10^3$) | 0.9276 | 1.0111 | 19 |
| 2.92 | 11.6 ($10^3$) | 0.9345 | 1.009 | 9 |
| 3.85 | 21.5 ($10^3$) | 0.9393 | 1.0079 | 16 |
| 1.97 | 2.98 ($10^3$) | 0.8951 | 1.018 | 24, Test 28 |
| 2.6 | 2.19 ($10^3$) | 0.9187 | 1.014 | 24, Test 25 |
| 3.7 | 4.10 ($10^3$) | 0.9281 | 1.013 | 24, Test 20 |
| 4.5 | 6.59 ($10^3$) | 0.9250 | 1.011 | 24, Test 22 |

A few experimental results are available for comparison with these calculations. Boundary-layer profiles are available behind incident-reflected shock wave interactions at $M = 2.92$ and total pressure ratios of 3.8 and 2.8. From these experiments, values of $\kappa_2/\kappa_1$ and $\delta_2/\delta_1$ can be calculated. The experimental values of these quantities, shown in Figs. 10 and 11, compare favorably with the calculated values.

For the configurations involving large separated regions, some means of relating the boundary-layer parameters is required. Lacking a sound theoretical model of the turbulent boundary layer, it is necessary to fall back on an empirical correlation of these properties. A fair body of experimental data exists, especially for incompressible flow, that indicates that, to a reasonable approximation, $f$ and $\kappa$ may be related and the boundary layer may be described by a single parameter, at least in the regions of mild pressure gradients. Such a correlation was first suggested in reference 22, and in reference 29 it has been shown that the boundary-layer measurements in reference 23 for equilibrium boundary layers under three different pressure gradients can be described as a one-parameter family with only small error.

This type of assumption has been used in treating the problem of shock-induced separation on a flat plate in references 1, 5, and 6. References 1 and 6 use different single parameters to describe the separated and unseparated layer and reference 5 uses the $f$-$\kappa$ nomenclature and a single $f$-$\kappa$ curve. All of these methods are essentially based on the idea that separation can be described by a single parameter. Reasonable correlation was obtained with experiment. These analyses would lead one to believe that the boundary layer had expended itself in overcoming this pressure rise associated with separation, and that it was incapable of further pressure rise without influx of momentum. This interpretation leaves unexplained the mechanism by which the boundary layer is capable of reattaching through an additional pressure rise only a short distance after separation was occurred, as is observed in the incident-reflected type of shock-wave interaction. However, an explanation can be obtained of how the boundary layer can overcome an additional pressure rise without influx of momentum by considering flow models appropriate to the configuration being considered. In order to demonstrate this point, it will be necessary to adopt a one-parameter boundary-layer description as was done in previous work. An $f$-$\kappa$ relation, somewhat modified from that used in reference 5, which did not fit the boundary-layer profiles measured in shock-wave boundary experiments, will be used. By assuming the $f$-$\kappa$ relation to be a function of Mach Number, it appears to be possible to obtain a better representation of the experimental data. Using these same $f$-$\kappa$ relations, it will be shown that different flow models can be used to describe both the large separated region on a flat plate and separating-reattaching flow which takes place in strong incident-reflected shock-wave interactions.

The $f$-$\kappa$ relation which will be adopted for the incompressible flow is that presented in reference 29 based on the experiments of reference 23. This curve is shown in Fig. 12 labeled $M = 0$. At higher Mach Number, there is some data available to show that for the zero pressure gradient boundary layer the value of $f$ decreases and the value of $\kappa$ increases with Mach Number. These data are shown in Fig. 13 along with curves for a velocity profile of the form $u/u_e = (y/\delta)^{1/N}$ for values of $N = 7$ and 9 and listed in Table 1. Not enough reliable information is available to draw definite conclusions in this matter. For the purposes of the present analysis, a set of curves will be constructed which are in agreement with the boundary-layer profiles measured in the shock-wave boundary-layer experiments. These curves are constructed by transforming the incompressible $f$-$\kappa$ curve by the relations

$$(1 - \kappa)/(1 - \kappa_0) = (1 - \kappa_u)/(1 - \kappa_{u0})$$

$$(f - 1)/(f_0 - 1) = (f_u - 1)/(f_{u0} - 1)$$

These relations assure that the transformed curves will pass through the measured zero pressure gradient point and the $\kappa = 1, f = 1$ point, and have a shape similar to the incompressible curve. These curves are shown in Fig. 12 and compared with various boundary-layer measurements behind shock-wave interactions and in the separated region in front of forward-facing steps. The values used for $\kappa_0$ and $f_0$ are those measured in references 9, 16, and 19. These values are used so that the results may be compared with the measured results of these experiments. These curves are not thought to be universal but a reasonable representation of the boundary-layer behavior through these shock-wave interaction experiments. The comparison with the measurements behind the interaction region shows that although the argument is not so good as might be desired, the present curves represent a reasonable approximation of the data.

## SEPARATION ON A STRAIGHT WALL

To treat the case of separation on a straight wall, similar to the flow ahead of the forward-facing step, the flow model shown in Fig. 5a and found appropriate for this case will be used.

The mass and momentum equations written in the direction parallel to the wall in $f$-$\kappa$ terminology are

$$\frac{p_1\kappa_1 w_{e_1}\delta_1}{f - [(\gamma - 1)/2]\kappa_1^2 w_{e_1}^2} = \frac{p_2\kappa_2 w_{e_2}\delta_2}{f_2 - [(\gamma - 1)/2]\kappa_2^2 w_{e_2}^2} \quad (19)$$

$$p_1\delta_1\left[\frac{\gamma\kappa_1^2 w_{e_1}^2}{f_1 - [(\gamma-1)/2]\kappa_1^2 w_{e_1}^2} + \left(1 - \frac{p_2}{p_1}\right)\right] = p_2\delta_2 \frac{\gamma\kappa_2^2 w_{e_2}^2}{f_2[(\gamma-1)/2]\kappa_2^2 w_{e_2}^2} \quad (20)$$

These equations can be combined to eliminate $\delta_1$ and $\delta_2$

$$\frac{p_2}{p_1} = 1 + \frac{\gamma w_{e_1}^2}{(f_1/\kappa_1^2) - [(\gamma-1)/2]w_{e_1}^2} \times \left(1 - \frac{\kappa_2}{\kappa_1}\frac{w_{e_2}}{w_{e_1}}\right) \quad (21)$$

Together with the $f$-$\kappa$ relation of Fig. 12 and the inviscid shock relation to prescribe $w_{e_2}$ this equation can be used to give $\kappa_2/\kappa_1$ as a function of $p_2/p_1$. The maximum values of $p_2/p_1$ correspond to the minimum values of $\kappa_2/\kappa_1$. Therefore, the maximum pressure ratio possible will be the separation pressure ratio. A similar analysis was carried out in reference 5; the basic method of the present calculation is the same but the numerical details are different.

## Incident-Reflected Shock Wave With Separation and Reattachment

In the case of the incident-reflected shock wave, a similar analysis may be made. Here a flow model of the type shown in Figs. 5(b) and 5(c) may be used. In both these models, the pressure $p_i$ is constant throughout the region between the initial and final pressure rise, so both models are equivalent as far as the mass and momentum equations parallel to the wall are concerned.

For this case, the continuity equation is the same as Eq. (19) and the momentum equation becomes

$$I_1 + p_1\delta_1 = I_2 + p_2\delta_2 + p_i(\delta_1 - \delta_2)$$

$$p_1\delta_1\left[\left(1 - \frac{p_i}{p_1}\right) + \frac{\gamma\kappa_1^2 w_{e_1}^2}{f_1 - [(\gamma-1)/2]\kappa_1^2 w_{e_1}^2}\right] = p_2\delta_2\left[\left(1 - \frac{p_i}{p_2}\right) + \frac{\gamma\kappa_2^2 w_{e_2}^2}{f_2 - [(\gamma-1)/2]\kappa_2^2 w_{e_2}^2}\right] \quad (22)$$

$\delta_2$ and $\delta_1$ may be eliminated to give

$$\frac{\kappa_2[1 - (p_i/p_2)]\{(f_2/\kappa_2^2) - [(\gamma-1)/2]w_{e_2}^2\} + \gamma w_{e_2}^2}{\kappa_1[1 - (p_i/p_1)]\{(f_1/\kappa_1^2) - [(\gamma-1)/2]w_{e_1}^2\} + \gamma w_{e_1}^2} = \frac{w_{e_2}}{w_{e_1}} \quad (23)$$

For a given incident shock strength, $p_2$ and $w_{e_2}$ may be calculated from the inviscid shock relation. $p_i$ for the configuration shown in Fig. 5(b) should be taken as the value behind the incident shock wave, and for the configuration shown in Fig. 5(c) for the value associated with the separation pressure rise on a flat surface. As stronger shock waves are considered, the value $p_i$ should be taken equal to the value behind the incident shock wave until this value becomes equal to the value associated with the separation value. At higher incident shock strengths, the pressure $p_i$ should be kept constant at this separation value. Eq. (23), together with the $f$-$\kappa$ curve and the inviscid shock relations, is sufficient to determine the conditions behind the interaction region. Once $f_2$ and $\kappa_2$ are found, $\delta_2/\delta_1$ can be found from Eq. (19).

## Calculated Results

The separation pressure ratios were calculated using Eq. (21) and are shown by the curve in Fig. 14, which is compared to the experimental values of references 20 and 28. The maximum pressure ratio obtained through the separation in front of steps has been used, and not the pressure ratio at the point of separation, since this analysis should not be applied until after conditions have reached their final value and constant static pressure exists across the boundary layer. Since it is not known if the initial boundary-layer conditions for the experiments of reference 28 are the same as those used in the computations, there is some question about the comparison with these results.

Using Eq. (23) and the $f$-$\kappa$ curve, the results shown in Fig. 15 have been found for the incident-reflected shock-wave case. These results are presented for all pressure ratios but should not be correct for pressure ratios for which separation and reattachment do not occur. Using the $f$-$\kappa$ curves of Fig. 12, it is found that a solution is no longer possible for higher values of incident shock strength than those presented. This limit occurs at a higher value of $\kappa_2$ than the separation value, which might be expected to be the limiting value. It is questionable how much significance should be attached to this feature since the $f$-$\kappa$ curves themselves are questionable. The important result of this calculation is that, by using the same $f$-$\kappa$ relation, it is possible to obtain much higher pressure ratios with the incident-reflected shock configuration than the separation pressure ratio associated with the single shock on a flat plate. Even though separation occurs within the interaction region, it is possible for the boundary layer to reattach without the addition of momentum from the free stream. This result is consistent with the experimental observations.

## General Results and Discussion

In the first part of this analysis, the boundary-layer properties behind a shock-wave - boundary-layer interaction were calculated by the assumption of a discontinuity. By this method, both the $f$ and $\kappa$ boundary-layer parameters behind the interaction could be predicted. For interactions involving large separated regions, where the boundary layer thickness was given time to adjust, an empirical $f$-$\kappa$ relation based on measurements of equilibrium boundary layers was used.

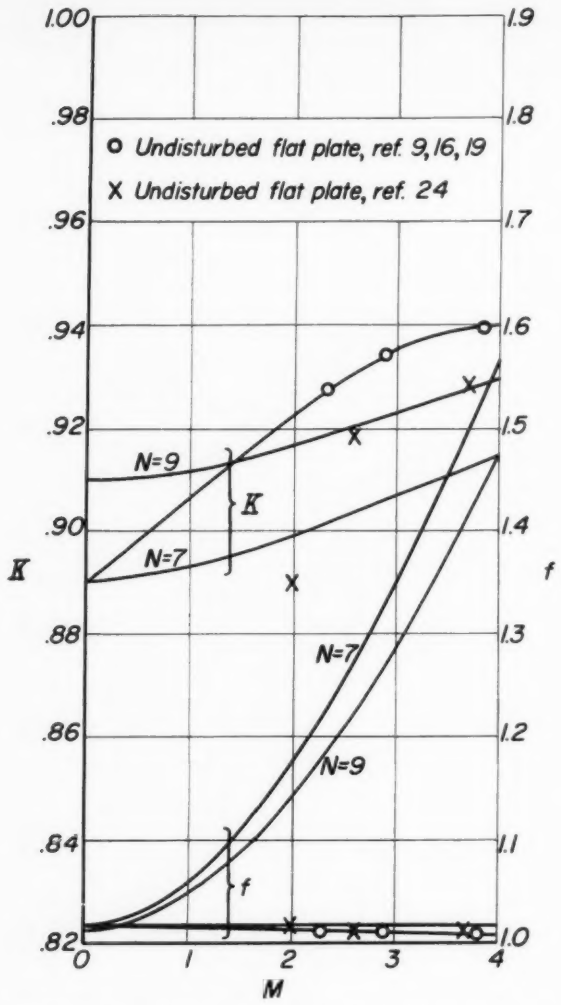


FIG. 13. $f$-$\kappa$ value for flat-plate boundary layers as a function of Mach Number.

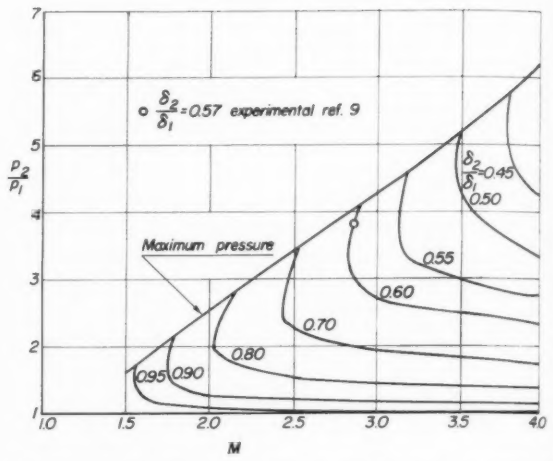


FIG. 15. Boundary-layer thickness behind incident-reflected shock waves based on empirical $f$-$\kappa$ curves.

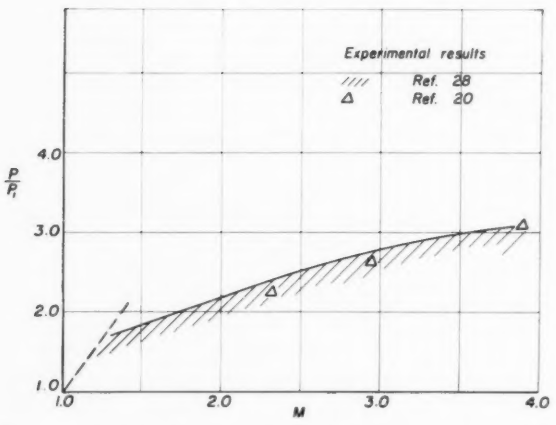


FIG. 14. Separation pressure ratio for large separated regions.

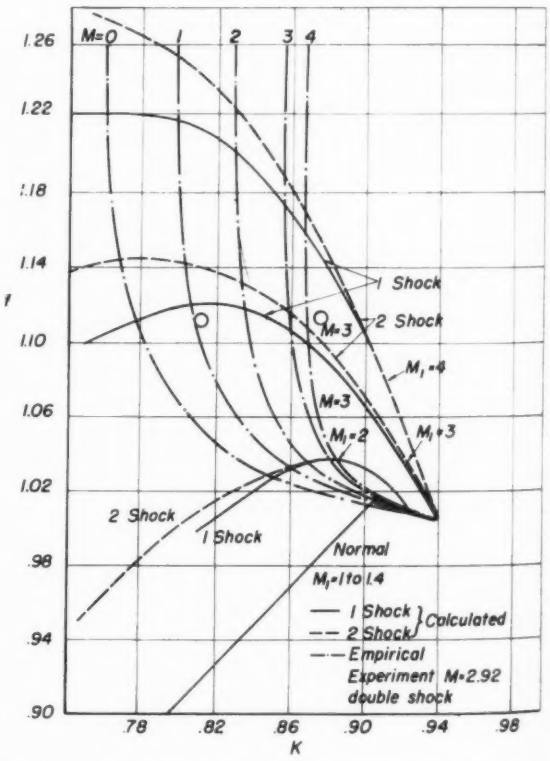


FIG. 16. Comparison of empirical and computed $f$-$\kappa$ curves.

Both the empirical $f$-$\kappa$ curves from Fig. 12 and those calculated by the discontinuity analysis are shown in Fig. 16. These curves are of considerably different shape. The experimental values of $f$ and $\kappa$ behind incident-reflected shock waves at $M = 2.92$ are shown in this Figure. The flow at the lower pressure ratio is definitely unseparated and, at the higher pressure ratio, separation is just beginning to occur. The point for the lower pressure ratio is close to the calculated curve while the point for the higher pressure ratio lies close to both curves. These two experimental points show that the discontinuity relations predict the $f$-$\kappa$ relations up to separation conditions fairly well and that the $f$-$\kappa$ values behind the interactions are considerably different from what might be expected from the incompressible equilibrium characteristics.

Empirical studies of incompressible boundary layers suggest that there is a connection between the value of $\kappa$ and the separation of the boundary layer. The analysis presented for the case of separation on a flat plate shows that this relation holds for compressible boundary layers if time is given for the boundary layer to follow an equilibrium type of $f$-$\kappa$ relation. It is interesting to see whether the same $\kappa$ values are associated with the appearance of separation when the boundary-layer parameters follow the calculated $f$-$\kappa$ curves. The values of $\kappa$ calculated by the discontinuity analysis for the pressure ratios at which separation is first observed experimentally, and the $\kappa$ separation values from the empirical curves are shown in Table 2. All these values agree surprisingly well, except for the last, and indicate that $\kappa$ may be a valid separation criterion for all turbulent boundary layers.

In this analysis, two different $f$-$\kappa$ relations have been considered. One relation is based on the equilibrium incompressible boundary-layer profiles. This relation is for the cases where the changes are gradual and the shear forces have sufficient time to reach an equilibrium distribution. The other relation describes the case behind a discontinuity. This result is obtained when the pressure change takes place so rapidly that the pressure forces completely dominate the shear forces. These two cases represent the extreme cases, and should bracket the actual physical changes.

For the case of a weak shock wave, when the phenomenon approaches a discontinuity, the discontinuity analysis appears to predict the correct $f$-$\kappa$ curves. For the stronger shock waves involving large separated regions, the empirical $f$-$\kappa$ relation is as reasonable an assumption as can be made at the present time. The important feature of this part of the analysis is that, by using the same empirical boundary-layer law, it is possible to show that much larger pressure ratios are possible with the incident-reflected type of shock-wave configuration and an attached boundary layer behind the interaction than the pressure ratio associated with separation in front of the forward-facing step. This analysis shows the difference in the physical flow model which makes the phenomenon possible.

In this whole analysis, the boundary layer is described by average parameters. It seems to be satisfactory to apply the continuity relations to the layer as a whole and neglect the shear forces, but this cannot be done in detail throughout the boundary layer. The controlling factor in the process is not found in the outer boundary layer but in the thin layer near the surface. The rate of momentum transport into this layer governs the pressure ratio which can be achieved before separation and the spreading out of the pressure rise in the direction along the wall. As long as only average parameters are used, an empirical correlation between these parameters and details of the flow near the wall will be needed, and the spreading out of the phenomenon in the direction along the wall cannot be predicted. The next step in a more complete analysis would be to include the shear forces in the region near the wall.

TABLE 2

| Configuration | $p_2/p_1$ Experimental* | $\kappa_2$ Calculated for $p_2/p_1$ sep. | $f_2$ Calculated for $p_2/p_1$ sep. | $\kappa_{sep.}$ Empirical† Fig. 12 |
|---|---|---|---|---|
| Normal shock | 1.95 | 0.790 | 0.85 | 0.79 |
| Incident-reflected $M = 3$ | 4.3 | 0.854 | 1.118 | 0.83 |
| Incident-reflected $M = 4$ | 4.1 | 0.855 | 1.195 | 0.85 |
| Single shock $M = 1.4$ | 1.8 | 0.811 | 0.945 | 0.80 |
| Single shock $M = 2.8$ | 3.5 | 0.818 | 1.101 | 0.82 |
| Single shock $M = 3.3$ | 5.5 | 0.751 | 1.139 | 0.82 |

* Highest pressure ratio obtainable before separation. First 3, reference 20; last 3, reference 28.
† Base on Mach Number behind interaction.

## CONCLUSIONS

A theory of shock-wave - boundary-layer interaction consistent with available experimental data can be formulated on the basis of no external mixing and no skin friction.

For shock waves not strong enough to cause separation, the boundary-layer properties behind the interaction can be calculated.

For strong interactions where large separated regions exist, the possibility of the different types of interactions which have been observed can be demonstrated by using the appropriate flow models and describing the boundary layer as a one-parameter family.

For all configurations, the pressure ratio at which separation occurs can be correlated by a boundary-layer form factor.

## REFERENCES

[1] Tyler, R. D., and Shapiro, A. H., *Pressure Rise Required for Separation in Interaction Between Turbulent Layer and Shock Wave*, Journal of the Aeronautical Sciences, Vol. 20, No. 12, pp. 858–860, December, 1953.

[2] Mager, A., *Prediction of Shock-Induced Turbulent Boundary-Layer Separation*, Journal of the Aeronautical Sciences, Vol. 22, No. 3, p. 201, March, 1955.

[3] Mager, A., *On the Model of the Free, Shock-Separated, Turbulent Boundary Layer*, Journal of the Aeronautical Sciences, Vol. 23, No. 2, p. 181, February, 1956.

[4] Schuh, H., *On Determining Turbulent Boundary-Layer Separation in Incompressible and Compressible Flow*, Journal of the Aeronautical Sciences, Vol. 22, No. 5, p. 343, May, 1955.

[5] Crocco, L., and Probstein, R. F., *The Peak Pressure Rise Across an Oblique Shock Emerging From a Turbulent Boundary Layer Over a Plane Surface*, Princeton University DAE Report 254, March, 1954

[6] Tucker, M., and Reshotko, E., *Effect of Discontinuity on Turbulent Boundary Layer Thickness Parameter With Application to Shock Induced Separation*, NACA TN 3454, May, 1955.

[7] Bogdonoff, S. M., and Solarski, A. H., *A Preliminary Investigation of a Shock Wave Turbulent Boundary Layer Interaction*, Princeton University DAE Report 184, November, 1951.

[8] Gadd, G. E., *Interactions Between Wholly Laminar or Wholly Turbulent Boundary Layers and Shock Waves Strong Enough to Cause Separation*, Journal of the Aeronautical Sciences, Vol. 20, No. 11, pp. 729–739, November, 1953.

[9] Bogdonoff, S. M., Kepler, C. E., and Sanlorenzo, E., *A Study of Shock Wave Turbulent Boundary Layer Interaction at $M = 3$*, Princeton University DAE Report 222, July, 1953.

[10] Donaldson, C. duP., and Lange, R. H., *Study of the Pressure Rise Across Shock Waves Required to Separate Laminar and Turbulent Boundary Layers*, NACA TN 2770, September, 1952.

[11] Kepler, C. E., and Bogdonoff, S. M., *Interaction of a Turbulent Boundary Layer With a Step at $M = 3$*, Princeton University DAE Report 238, September, 1953.

[12] Ackeret, J., Feldmann, F., and Rott, N., *Investigation of Compression Shocks and Boundary Layers in Gases Moving at High Speed*, NACA TN 1113, 1947.

[13] Barry, F. W., *A Review of Experimental Results on Boundary Layer - Shock Wave Interactions*, North American Aviation Rpt. No. AL 1599, 1952.

[14] Drougge, G., *An Experimental Investigation of the Influence of Strong Adverse Pressure Gradients on Turbulent Boundary Layers at Supersonic Speeds*, Aeronautical Research Institute of Sweden, Report #46, 1953.

[15] Bogdonoff, S. M., and Kepler, C. E., *Separation of a Supersonic Turbulent Boundary Layer*, Princeton University DAE Report 249, January, 1954.

[16] Vas, I., and Bogdonoff, S. M., *The Interaction of a Turbulent Boundary Layer With a Step at $M = 3.85$*, Princeton University DAE report 295 (to be published).

[17] Vas, I., and Bogdonoff, S. M., *The Interaction of a Shock Wave With a Turbulent Boundary Layer at $M = 3.85$*, Princeton DAE Report 294 (to be published).

[18] Vas, I., *A Detailed Study of the Interactions of a 14° Shock Wave With a Turbulent Boundary Layer at $M = 2.9$*, Princeton University DAE Report 296 (to be published).

[19] Wooten, G. G., Hight, S., and Vas, I., *Interaction of a Turbulent Boundary Layer With a Step at $M = 2.3$*, Princeton University DAE Report 297 (to be published).

[20] Bogdonoff, S. M., *Some Experimental Studies of the Separation of Supersonic Turbulent Boundary Layers*, Princeton University DAE Report 336, June, 1955.

[21] Love, E. S., *On the Effect of Reynolds Number Upon the Peak Pressure-Rise Coefficient Associated With the Separation of a Turbulent Boundary Layer in Supersonic Flow*, Journal of the Aeronautical Sciences, Vol. 22, No. 5, p. 345, May, 1955.

[22] Crocco, L., and Lees, L., *A Mixing Theory for the Interaction Between Dissipative Flow and Nearly Isentropic Streams*, Princeton University DAE Report 187, January, 1952.

[23] Clauser, F. H., *Turbulent Boundary Layers in Adverse Pressure Gradients*, Journal of the Aeronautical Sciences, Vol. 21, No. 2, pp. 91–108, February, 1954.

[24] Coles, D., *Measurements in the Boundary Layer on a Smooth Flat Plate in Supersonic Flow*, CIT JPL Report 20-69, 20-70, 20-71, June, 1953.

[25] Glassman, I., and John, J., *Private Communication*, Jet Propulsion Laboratory, Princeton University.

[26] Hammitt, A. G., *An Approximate Theory of Turbulent Boundary Layer Shock Wave Interaction*, Princeton University DAE Report 340, April, 1956.

[27] Hammitt, A. G., *An Analysis of the Interaction of Shock Waves With Unseparated Turbulent Boundary Layers*, Princeton University DAE Report 371, February, 1947.

[28] Chapman, Dean R., Kuehn, Donald M., and Larson, Howard K., *Preliminary Report on a Study of Separate Flows in Supersonic and Subsonic Streams*, NACA RM A55L14, June 12, 1956.

[29] Bray, K., *The Application of the Theory of Crocco and Lees in Shock Boundary Layer Interactions*, Princeton University DAE Report 322, July, 1955.

[30] Love, E. S., *Pressure Rise Associated with Shock-Induced Boundary Layer Separation*, NACA TN 3601, 1955.

*Notice*

Consistent with the general trend of Institute coverage, beginning with the July issue, the JOURNAL OF THE AERONAUTICAL SCIENCES will be known as:

JOURNAL OF THE AERO/SPACE SCIENCES

# The Laminar Free-Convective Heat Transfer From the Outer Surface of a Vertical Circular Cylinder†

KNOX MILLSAPS* AND KARL POHLHAUSEN**
*Air Research and Development Command, USAF*

SUMMARY

The boundary-layer problem that treats the laminar free-convective fluid motion produced by a heated vertical circular cylinder for which the thermal distribution on the outer surface varies linearly with the distance from the leading edge admits a similarity transformation that reduces the momentum and energy equations to two ordinary equations. The exact solutions to the ordinary differential system are obtained by numerical methods for parametric values of the Grashof and Prandtl Numbers. A comparison is given between the exact solutions and the approximations that are obtained by the Kármán momentum method using a parabolic assumption for the thermal profile.

## INTRODUCTION

IT IS WELL KNOWN that the analytical problem associated with the laminar free-convective heat transfer from the surfaces of a vertical flat plate can be satisfactorily treated by boundary-layer theory. In the particular cases where the surfaces are held at constant temperature, or where certain variations in the surface temperatures are specified, it has been shown[1] that a similarity transformation reduces the customary partial differential equations of boundary-layer theory to a system of two ordinary differential equations. One of these ordinary equations, which essentially describes the dynamical behavior of the fluid, is nonlinear; the other, which describes the thermal distribution, is linear, although it must be realized that the equations are closely coupled. The subsequent solutions to the equations are obtained by numerical methods since analytical solutions are unknown.

For the closely allied problem of the laminar free-convective heat transfer from the surfaces of a vertical circular cylinder which are held at a constant temperature, a similarity solution, if extant, has not been obtained; however, the problem has recently been attacked in very interesting ways with a direct treatment of the partial differential equations by expansion in power series and with the Kármán momentum method.[2] Consequently, it may be interesting to note that the case where the surface temperature varies linearly with the height of the cylinder, which is also of practical importance, admits a similarity transformation.

Received June 24, 1957.

† A preliminary report was presented at the Ninth International Congress of Applied Mechanics, Brussels, Belgium, September 5–13, 1956.

* Chief Scientist, Holloman Air Development Center.

** Senior Applied Mathematician, Wright Air Development Center.

The authors would like to express their gratitude to Frank Numan, who programed and obtained the numerical values for the exact solutions on the Bendix Digital Differential Analyzer of the Wright Air Development Center, and to Miss Martha Tongue, who performed desk calculations and graphical plottings.

## (1) MATHEMATICAL FORMULATION OF THE PROBLEM

In cylindrical coordinates $\bar{r}$, $\bar{z}$ the partial differential equations of laminar boundary-layer theory are

$$[\partial(\bar{r}\bar{u}_r)/\partial\bar{r}] + [\partial(\bar{r}\bar{u}_z)/\partial\bar{z}] = 0 \tag{1.1}$$

$$\bar{u}_z(\partial\bar{u}_z/\partial\bar{z}) + \bar{u}_r(\partial\bar{u}_z/\partial\bar{r}) = \nu[(\partial^2\bar{u}_z/\partial\bar{r}^2) + (1/\bar{r})(\partial\bar{u}_z/\partial\bar{r})] + g\beta(\bar{T} - \bar{T}_0) \tag{1.2}$$

$$\bar{u}_z(\partial\bar{T}/\partial\bar{z}) + \bar{u}_r(\partial\bar{T}/\partial\bar{r}) = \alpha[(\partial^2\bar{T}/\partial\bar{r}^2) + (1/\bar{r})(\partial\bar{T}/\partial\bar{r})] \tag{1.3}$$

where

$\bar{u}_z$ = vertical component of the local fluid velocity
$\bar{u}_r$ = radial component of the local fluid velocity
$\nu$ = kinematic viscosity of the fluid
$g$ = acceleration of gravity
$\beta$ = coefficient of cubic thermal expansion
$\bar{T}$ = local temperature of the fluid
$\bar{T}_0$ = ambient temperature
$\alpha$ = thermal diffusivity

Naturally, the term $g\beta(\bar{T} - \bar{T}_0)$ in the momentum equation represents the buoyancy effect. An idea of the physical geometry may be acquired by noting the schematic diagram in Fig. 1.

Denoting the fixed radius of the cylinder by $a$, it is convenient to introduce the following dimensionless variables and parameters:

$$r = \bar{r}/a, \quad z = \bar{z}/a, \quad u_r = a\bar{u}_r/\nu, \quad u_z = a\bar{u}_z/\nu, \quad \vartheta = g\beta a^3(\bar{T} - \bar{T}_0)/\nu^2$$

and $\sigma = \nu/\alpha$, where $\vartheta$ represents the Grashof temperature and $\sigma$ represents the Prandtl Number. Multiplying Eqs. (1.1), (1.2), and (1.3) by $a/\nu$, $a^3/\nu^2$, and $g\beta a^5/\nu^3$, respectively, in dimensionless terms the fundamental equations become

$$[\partial(ru_r)/\partial r] + [\partial(ru_z)/\partial z] = 0 \tag{1.4}$$

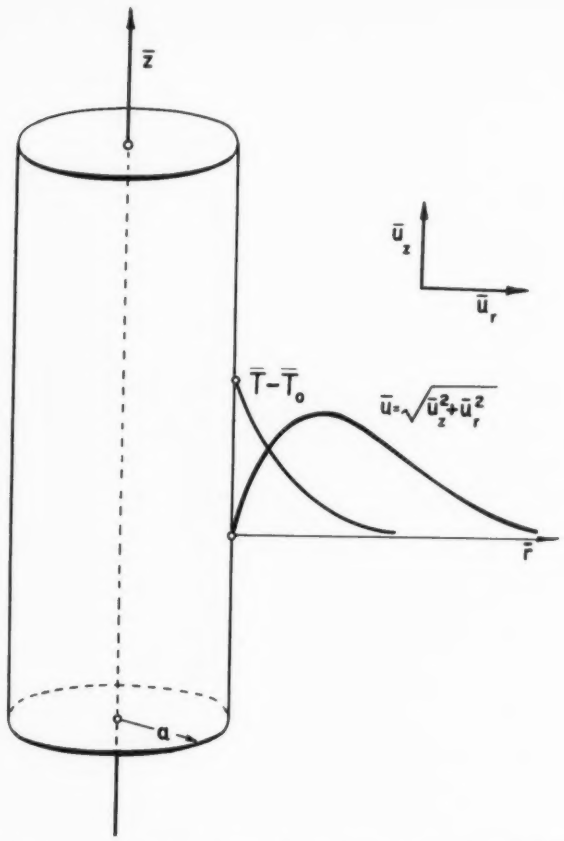


FIG. 1. Schematic diagram of the heated vertical cylinder showing the coordinate system and notations.

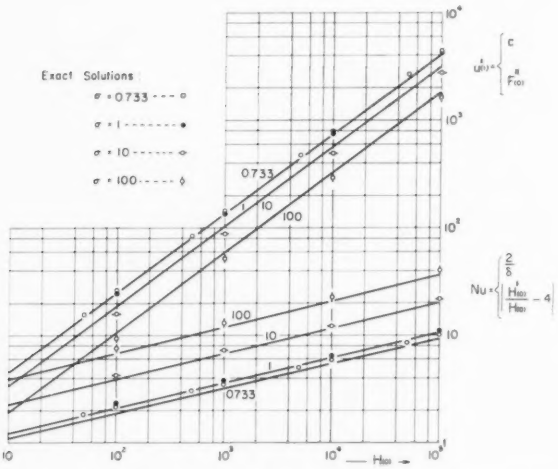


FIG. 2. Nusselt Number and the initial slope of the dynamic profiles for parametric values of the Prandtl Number. (The full lines represent the parabolic approximations; the points represent the values of the exact solutions.)

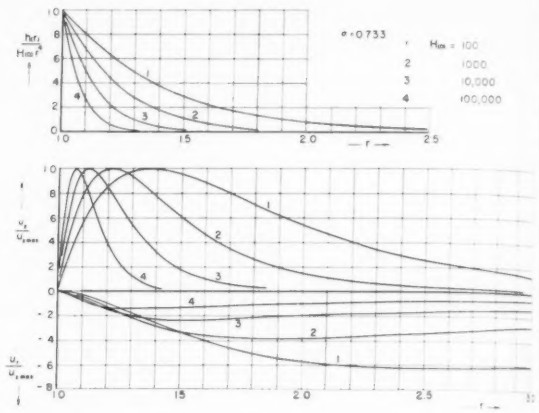


FIG. 3(a). Exact solutions for the dynamic and thermal profiles for parametric values of the modified Grashof Number and for Prandtl Number 0.733.

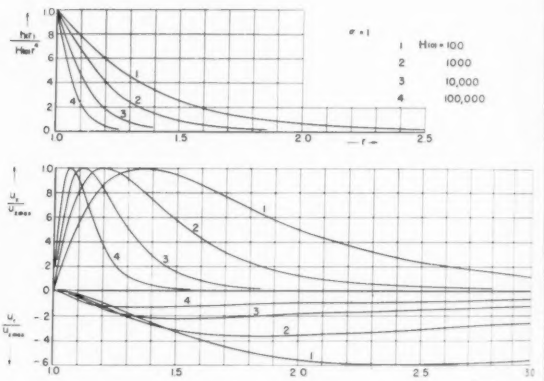


FIG. 3(b). Exact solutions for the dynamic and thermal profiles for parametric values of the modified Grashof Number and for Prandtl Number 1.000.

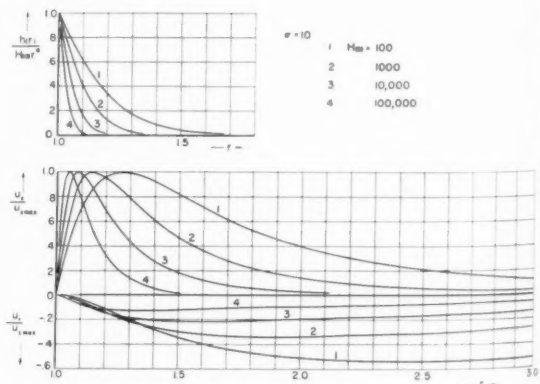


FIG. 3(c). Exact solutions for the dynamic and thermal profiles for parametric values of the modified Grashof Number and for Prandtl Number 10.00.

$$u_z(\partial u_z/\partial z) + u_r(\partial u_z/\partial r) = (\partial^2 u_z/\partial r^2) + (1/r)(\partial u_z/\partial r) + \vartheta \quad (1.5)$$

$$u_z(\partial \vartheta/\partial z) + u_r(\partial \vartheta/\partial r) = (1/\sigma)[(\partial^2 \vartheta/\partial r^2) + (1/r)(\partial \vartheta/\partial r)] \quad (1.6)$$

At this point in the analysis it is customary to introduce a stream function $\psi$, such that

$$\partial\psi/\partial r = ru_z \quad \text{and} \quad \partial\psi/\partial z = -ru_r \quad (1.7)$$

If one now takes

$$\psi = zf(r) \quad \text{and} \quad \vartheta = zh(r)\, r^4 \quad (1.8)$$

a series of algebraic manipulations shows that the continuity equation is satisfied identically and that the remaining two equations are reduced to the following ordinary equations:[3]

$$r^2f''' + r^2ff'' - r^2f'' - r^2(f')^2 - rff' + rf' + h = 0 \quad (1.9)$$

$$r^2h'' + (\sigma f - 7)rh' + (16 - 4\sigma f - \sigma rf')h = 0 \quad (1.10)$$

where primes denote differentiation with respect to $r$. Eqs. (1.9) and (1.10) are ordinary Eulerian differential equations which can be reduced further by the transformation $r = \exp t$ to the following forms:

$$F''' + (F - 4)F'' + (4 - 2F - F')F' + H = 0 \quad (1.11)$$

$$H'' + (\sigma F - 8)H' + (16 - 4\sigma F - \sigma F')H = 0 \quad (1.12)$$

where primes now denote differentiation with respect to $t$ and where $H(t) = h(r)$ and $F(t) = f(r)$. The physical boundary conditions when transformed to the dimensionless variables are

$$F(0) = 0, \quad F'(0) = 0, \quad H(0) = \text{const.} \quad (1.13)$$

at the surface of the cylinder and

$$F'(\infty) = 0, \quad H(\infty) = 0 \quad (1.14)$$

at an infinite distance from the cylinder. The boundary condition $H(0) = \text{const.}$ requires that the thermal distribution on the surface of the cylinder must vary linearly with the height of the cylinder.

## (2) Numerical Solutions of the Equations

It does not appear possible to obtain analytical solutions for the differential system (1.11) and (1.12); consequently, it appears desirable to resort to numerical procedures. The difficulty in obtaining numerical solutions lies in two facts: the nonlinearity of the first differential equation and the two point boundary conditions. These facts mean that one has to integrate the differential system as an initial value problem with the three known initial conditions and determine the two additional initial values $F''(0)$ and $H'(0)$, such that $F'(\infty) = 0$ and $H(\infty) = 0$.

As a convenience in obtaining approximate values $F''(0)$ and $H'(0)$, the Kármán momentum method is applied to Eqs. (1.5) and (1.6). If one denotes $r - 1$ by $y$, which represents a dimensionless distance from the cylinder wall, and $\bar{\delta}$ $a$ by $\delta$, which represents the dimensionless thickness of the boundary layer, one finds by integration that

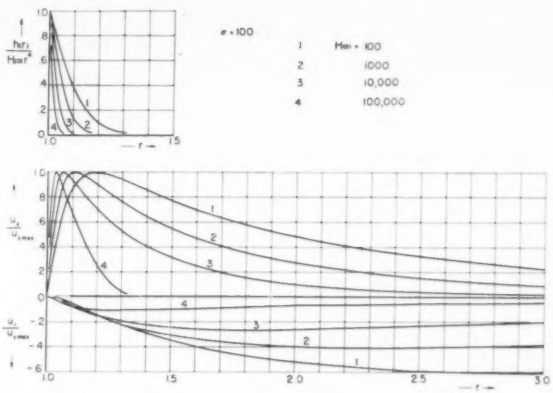


FIG. 3(d). Exact solutions for the dynamic and thermal profiles for parametric values of the modified Grashof Number and for Prandtl Number 100.0.

$$(d/dz)\int_0^\delta u_z^2(1 + y)dy = \int_0^\delta \vartheta(1 + y)dy - (\partial u_z/\partial y)_{y=0} \quad (2.1)$$

$$(d/dz)\int_0^\delta u_z\vartheta(1 + y)dy = -(1/\sigma)(\partial\vartheta/\partial y)_{y=0} \quad (2.2)$$

At a similar point in any analogous treatment it is customary to assume dynamic and thermal profiles and to use Eqs. (2.1) and (2.2) in order to get integral corrections to the constants in the assumed profiles. One of the simpler assumptions is to approximate the dynamic profile with a particular cubic and to take a parabola with the same thickness as the thermal profile—i.e.,

$$u_z = cz(y/\delta)[1 - (y/\delta)]^2 \quad (2.3)$$

$$\vartheta = \vartheta_0 z[1 - (y/\delta)]^2 \quad (2.4)$$

These assumptions are very rough approximations since they fail to satisfy the differential system when it is evaluated at the surface of the cylinder. The assumptions could be improved by taking higher-order terms; however, since a first-order result is sufficient for later improvement on large scale computers, the work that is necessary to obtain higher order approximations does not appear to be worth while.

Introducing the assumptions (2.3) and (2.4) into Eqs. (2.1) and (2.2) and proceeding in a precisely analogous way to the treatment of the vertical plate,[4] one finally sees that

$$c^2\delta^2(8 + 3\delta) = 35\vartheta_0\delta^2(4 + \delta) - 420c \quad (2.5)$$

$$c = 210/\sigma\delta^2(7 + 2\delta) \quad (2.6)$$

$$1260(8 + 3\delta) = \sigma^2\vartheta_0\delta^4(4 + \delta)(7 + 2\delta)^2 - 2520\sigma(7 + 2\delta) \quad (2.7)$$

TABLE 1
Comparison of the Exact Solutions With Parabolic Approximations

| | | Exact Solutions | | | | Parabolic Approximations | | |
|---|---|---|---|---|---|---|---|---|
| | | | (1) | (2) | (3) | (4) | (5) | (6) |
| $\sigma$ | $H(0)$ | $H'(0)$ | $\left\|\frac{H'(0)}{H(0)} - 4\right\|$ | $F''(0)$ | $max\ (u_z)$ for $z = 1$ | $2/\delta$ | $c$ | $max\ (u_z)$ for $z = 1$ |
| 0.733 | 50 | 107.4 | 1.852 | 15.60 | 2.61 | 1.58 | 15.0 | 2.80 |
| | 100 | 187.3 | 2.127 | 25.99 | 3.71 | 1.85 | 24.9 | 3.98 |
| | 500 | 511.2 | 2.978 | 85.36 | 8.39 | 2.68 | 81.1 | 8.96 |
| | 1,000 | 539.1 | 3.461 | 142.7 | 12.0 | 3.15 | 135 | 12.7 |
| | 5,000 | −4,802 | 4.960 | 472.2 | 26.8 | 4.60 | 444 | 28.6 |
| | 10,000 | −18,184 | 5.818 | 791.5 | 38.2 | 5.43 | 743 | 40.5 |
| | 50,000 | −223,970 | 8.479 | 2630 | 86.2 | 8.01 | 2456 | 90.8 |
| | 100,000 | −600,040 | 10.00 | 4415.4 | 122 | 9.49 | 4122 | 129 |
| 1 | 100 | 168.4 | 2.316 | 24.70 | 3.40 | 2.05 | 25.2 | 3.64 |
| | 1,000 | 206.2 | 3.794 | 135.72 | 11.0 | 3.49 | 137 | 11.6 |
| | 10,000 | −24,070 | 6.407 | 753.01 | 34.8 | 6.04 | 754 | 37.0 |
| | 100,000 | −704,700 | 11.05 | 4202.1 | 111 | 10.56 | 4185 | 117 |
| 10 | 100 | −22.54 | 4.225 | 15.74 | 1.54 | 3.84 | 18.5 | 1.43 |
| | 1,000 | −3,164 | 7.164 | 87.06 | 5.00 | 6.66 | 102 | 4.53 |
| | 10,000 | −83,830 | 12.38 | 485.0 | 15.8 | 11.63 | 563 | 14.3 |
| | 100,000 | −1,765,000 | 21.65 | 2711.5 | 50.0 | 20.5 | 3151 | 45.5 |
| 100 | 100 | −346.6 | 7.466 | 9.259 | 0.590 | 6.74 | 10.6 | 0.465 |
| | 1,000 | −8,912 | 12.91 | 51.26 | 1.89 | 11.8 | 58.5 | 1.47 |
| | 10,000 | −185,900 | 22.59 | 288.0 | 6.05 | 20.8 | 327 | 4.67 |
| | 100,000 | −3,556,000 | 39.56 | 1600 | 18.4 | 36.8 | 1837 | 14.8 |

After $\delta$ is determined for corresponding values of $\sigma$ and $\vartheta_0$, which is usually done by an inverse process, a bit of reflection shows that

$$F''(0) = c \tag{2.8}$$

and, from Eq. (1.8) since $\vartheta_0 = H(0)$, that

$$H'(0) = (4 - 2/\delta)H(0) \tag{2.9}$$

For sufficiently small values of $\delta$ Eq. (2.7) can be solved to give

$$\delta = (90/7)^{1/4}\vartheta_0^{1/4}\sigma^{-1/2}(4 + 7\sigma)^{1/4} \tag{2.10}$$

The values of $F''(0)$ and $H'(0)$ that are given by Eqs. (2.8) and (2.9) are used as first approximations whose accuracies are improved by a systematic trial-and-error scheme on a large scale digital computer. Table 1 is a comparison of the approximate and exact values; one should compare Column $n$ with Column $n + 3$.

Fig. 2 represents a survey of the initial values as a function of $H(0)$. Figs. 3(a), 3(b), 3(c), and 3(d) are graphs of the exact solutions for the dynamic and thermal profiles for parametric values of the Prandtl and Grashof Numbers.

In engineering applications an important quantity is the Nusselt Number $N_u$ which is defined as the product of the coefficient of heat transfer and the radius of the cylinder divided by the thermal conductivity of the fluid. For the parabolic assumptions one has

$$N_u = 2/\delta \tag{2.11}$$

and for the exact solution one has

$$N_u = \left|\frac{H'(0)}{H(0)} - 4\right| \tag{2.12}$$

Once again, a comparison between the approximate and exact values of the Nusselt Number occurs in Fig. 2.

## REFERENCES


[1] Schmidt, E., and Beckman, W., Forsch. Ing-Wes., Vol. 1, p. 391, 1930. See also Finston, M., *Free Convection Past a Vertical Plate*, J. Appl. Math. Phys. (ZAMP), Vol. 7, p. 527, 1956.

[2] Sparrow, E. M., and Gregg, J. L., *The Laminar-Free-Convection Heat Transfer From the Outer Surface of a Vertical Circular Cylinder*, Trans. Am. Soc. Mech. Engrs., Vol. 78, p. 1823, November, 1956. See also LeFevre, E. J., and Ede, A. J., Paper No. I-167, Ninth International Congress of Applied Mechanics, Brussels, Belgium, 1956.

[3] Millsaps, Knox, and Pohlhausen, Karl, *The Laminar Free-Convective Heat Transfer from the Surfaces of a Vertical Circular Cylinder*, Journal of the Aeronautical Sciences, Readers' Forum, Vol. 23, No. 4, p. 381, April, 1956.

[4] Goldstein, S. (Ed.), *Modern Developments in Fluid Dynamics*, Vol. II, p. 641; Clarendon Press, Oxford, England, 1938.



## 1958 HEAT TRANSFER AND FLUID MECHANICS INSTITUTE

*University of California at Berkeley, June 19–21, 1958*

The 1958 Institute is devoted to fundamental contributions in thermo and fluid dynamics. Emphasis is given to topics covering more than one specific field of engineering science; particular attention is devoted to those problems in fluid mechanics which require consideration of thermal phenomena (aerothermodynamics), chemical reactions (aerothermochemistry), and electromagnetic fields (magnetohydrodynamics).

*General Chairman:* A. K. OPPENHEIM, Aeronautical Sciences, University of California, Berkeley, Calif.

# A Pilot Analog for Airplane Pitch Control†

N. D. DIAMANTIDES*
*Goodyear Aircraft Corporation*

SUMMARY

A simplified pilot analog has been developed that accurately matches the motions of a jet interceptor pilot as he controls a pitching airplane. The analog was constructed by use of electronic computer components, and its design was clarified by postulating mathematical representations of the human dynamics involved.

The analog was tested in a control loop that included simulated pitch disturbances, the main characteristics of an F-89B jet interceptor, and a movable cockpit mock-up equipped with a simplified control column and display. The test loop permitted operation of the analog in parallel with human pilots so the control motions of both, when presented with identical stimuli, could be recorded for comparison. Control could be switched, without the pilot's knowledge, to analog or pilot. The analog performed so accurately that experienced jet pilots often did not immediately detect its substitution for themselves in the control loop.

The analog required simple adjustments for each test subject, but it was proved to be representative of an "average" pilot's dynamics within the scope of the simple control task. Moreover, the adjustments permitted measurement of human characteristics, thus making the analog a more versatile tool for human dynamics research. Its success encourages the development of more complex pilot simulators that would provide accurate data on little-known characteristics of the human as a controller and that also could be used to predict human performance in specific machine systems before costly experimental models are built.

## (1) INTRODUCTION

THE LACK of an accurate method of predicting the performance of the human controller often complicates the development of complex, high-speed modern machines. The need for a reliable indicator of the performance of the pilot of a high-speed airplane, while the machine still is in the early stages of design, increases proportionately with the increasing difficulty of the pilot's role and with the rising costs involved in constructing experimental models.

An accurate analog of an "average" pilot's dynamics could be put to many uses:

(1) In pilot performance analysis—to test the applicability of certain linear and nonlinear analytical techniques to the pilot-airplane system.

(2) In machine design—to close the loop of the pilot-airplane system while the airplane still is on the drawing board and, thus, permit incorporation of changes and improvements prior to construction.

(3) In instrument design—to investigate the pilot's use of control information and permit proper design of input instruments (gyro-horizon, control-stick mechanism, radar display) and output devices (control-surface linkages, airframe dynamics).

(4) In investigating effects of abnormal aerodynamic and control-stick-feel parameters on pilot performance—to establish levels of such parameters conducive to effective pilot control without overtaxing pilot physical capabilities.

(5) In assessing pilot adaptation effects—to determine variations in the day-to-day performance of individuals and among pilots.

A number of pilot simulators have been built and tried,[1] but the novelty of the art and the limited knowledge on which they arbitrarily were based hindered the reliable representation of physiological functions. Pilot simulators, however, when used in combination with accepted statistical methods, probably constitute the only effective method of evaluating the mathematical formulas postulated to represent human dynamics.

In contrast to the electronic analog, the describing function and other mathematical approximations of pilot physiological characteristics may seem attractive as a short method of defining pilot dynamics, but they are merely approximations of the analog, which, itself, is an approximate device. The tendency to translate human control characteristics into transfer functions—or, where nonlinearities are involved, into describing functions—is fully justified, however, because these postulations can be used to formulate a shorthand overall pilot equation, and the pilot equation can be used, though in a limited manner, to represent the electronic simulator.

A pilot equation that can be considered representative of the simplified electronic pilot analog for airplane pitch control, developed by Goodyear Aircraft Corporation for the U.S. Navy, is formulated here to aid in describing the design of the electronic model. This pilot analog was designed for the simple longitudinal control of a jet interceptor subjected to forced random disturbances. Thus, a single independent variable was involved, and the task required only continuous compensatory control. Considerable refinement of the analog would be required to encompass more complex tasks. The analog's accuracy, however, in matching pilot hand motions encourages the development of more complex pilot analogs to simulate the many variables involved in actual flight.

Received May 31, 1957. Revised and received December 23, 1957.

† The airplane mock-up and the original version of the pilot analog were designed by R. J. Mead, the project engineer. The project was contractually supported by the U.S. Navy, Bureau of Aeronautics, under Contract NOa(s)-54-244-c, with Goodyear Aircraft Corporation. The advanced version of the simulator is the result of a joint effort of the author and Mr. Mead. Dr. A. J. Cacioppo was the adviser on the psychological approach to the problem, and E. W. McGraw and M. Mazoh were in charge of the structural design of the mock-up.

* Senior Development Engineer, Avionics and Electronics Division.

## (2) Pilot Analog Development

### *Synthetic Approach*

The chief purpose of developing a pilot analog is to specify what the pilot is dynamically. By use of the available control-engineering data, this problem can be approached synthetically or analytically.

The synthetic approach requires scrutiny of pilot performance data, as recorded by an oscillograph, on the basis of servo experience. It must be remembered that this approach requires a good knowledge of pilot control behavior and is effective only when the experimenter understands the underlying physiological factors as well as the mechanisms used to represent them.

Taking into account what is known or suspected about the physiological make-up of the human controller, the researcher constructs an analog computer circuit or other hypothetical model of the human control system. The model of the pilot then is tested in the applicable aircraft control situation. The differences between human and analog performance outputs for identical inputs permit an accurate evaluation of the analog and yield data that will prove useful in refining the analog to the extent that, ultimately, the pilot will not detect its substitution for himself in the control loop.

The synthetic approach requires no a priori assumptions regarding the linearity of human dynamics; instead, it encourages the tendency to compare the human control system with familiar discontinuous servomechanisms. For studies of this type, it is expedient to view the pilot as a human servo, or as a nonlinear and rather complex control mechanism. Because of the considerable evidence that the human operator is nonlinear and because the analytic approach primarily requires linear approximations, the synthetic approach was employed in the development of the pilot analog for airplane pitch control.

### *Human Control Characteristics*

A disturbance to the airplane pitch attitude was the stimulus presented to both the real and simulated operators. Perception of this stimulus was the pilot's first task and the first to be considered in designing the pilot simulator.

The human operator normally does not react to stimuli unless their magnitude is above a certain threshold level, set up by the physiological limitations of the perceptual organs or by his mental attitude toward the situation; the latter is influenced by such factors as training and biological make-up. Thus, the operator does not sense or does not value small disturbances enough to attempt a response.

Once the pitch deviation exceeds the threshold level, the perceived information is transmitted to the brain, which decides what kind of corrective maneuver should be applied to the controls to offset the disturbance. The brain sends the appropriate command to the motor elements of the body (muscles and supporting skeletal parts). The signal flow from sensors through the central nervous system to the motor inputs require a measurable time, the average length of which is found to be approximately constant in all normal persons. This is called the reaction time.

Following perception of the stimulus, the human controller apparently performs two essentially linear operations: (1) a mental computation of the stimulus, or the weighing and summing of position, rate, and acceleration to achieve a basis for the decision to act, and (2) an involuntary placing of definite physical limitations on corrective hand motions, which is caused by the neuromuscular, or motor, feedback loop.

Although seldom, if ever, observed without a reaction time delay, mental computation does not require any conscious calculation by the pilot. The weighing, summing, and decision functions are similar to those used by the rope walker in balancing.

The type of data used in mental computation can be identified with the stimulus receptors involved. The movement of the airplane with respect to the horizon is transmitted by the eyes as a signal proportional to the amplitude of the airplane displacement. Rate-of-motion information is sensed by the ear canals (viscous flow of the endolymph fluid) and the eyes (through peripheral vision,[2] a result of the successive stimulation of the rods of the macula). Finally, linear and angular acceleration stimulates the vestibular organs of the inner ear and the proprioceptors of body muscles, tendons, and joints. It is also conceivable that pressure-nerve nets transmit impact sensations.

In addition to the components of the original pitch error signal and its time derivatives—as modified by mental computation, reaction time, and threshold level—the pilot's estimation of the magnitude of the total error signal appears to be an important factor in his functioning as a controller. In tests of the pilot analog, it was observed that the human pilot initiates reflexive control motions concurrently with, or even slightly before, zero crossings instead of after one reaction-time interval. The resulting hand motions appear on oscillographic recordings as a series of unevenly spaced square waves of alternate polarity superimposed on the prime control signal and initiated when the pitch error signal crosses zero.

To achieve zero error in the steady state, the pilot must center the control stick the instant before the airplane attitude reaches the level condition. Without prediction, a human controller, functioning similarly to a discontinuous servo, could not accomplish such centering action in the presence of a finite threshold level and reaction time. This discontinuous control-signal component and the part of the pilot analog that embodies it are called the "bias."

### *Selection of Error Input*

Significant in the design of the pilot analog for airplane pitch control was the selection of an error input that would represent the airplane's motion parameters

adequately for pilot perception. To simplify the simulation of the airplane dynamics, the pitch attitude, $\theta_{wp}$, was selected as the variable to supply the pilot with cues for control.

A pilot associates a certain control-stick force per $g$ with the operating characteristics of his airplane, which include speed ($V$), altitude, weight, and center of gravity. Therefore, the flight-path attitude, $\gamma$, can be used as the primary input variable because the control-stick load-factor increment is $V\dot{\gamma}/g$.

Control-stick force, as incorporated in the airplane mock-up used in these studies, was not affected by the flight-path attitude. A mechanism capable of conveying a true control-stick-feel effect was not employed because this would have required simulation of the aerodynamic forces normally acting on control surfaces, and it was desired to keep the simulation as simple as possible.

### *Mathematical Representation of Human Functions*

A block diagram of the pilot analog for airplane pitch control is shown in Fig. 1. The order of the various operations—mental computation, bias, threshold level, and reaction time—is consistent with the order of the underlying physiological mechanisms. Although the placement of the characteristics may be questioned, the circuit based on the design served to trick pilots in pilot-pilot analog substitution tests.

The pitch-error signal, $\theta_{wp}$, and its two time derivatives, rate and acceleration, are shown in the mental computation section of Fig. 1. The output of the computation block is

$$x_1(s) = G_s(s)\theta_{wp}(s) = (k_3s^2 + k_2s + k_1)\theta_{wp}(s) \quad (1)$$

where $s$ is the Laplace operator representing derivatives in the time domain and $G_s$ is the describing function for mental computation.

The signal from the mental-computation elements results in a threshold output, $x_2$. The describing function,[3] $G_t(x_1)$, relating $x_2$ to $x_1$, is a function of the amplitude of $x_1$. This relationship can be stated as

$$x_2/x_1 = G_t(x_1) \quad (2)$$

The describing function for the threshold element (see Fig. 2) has no component sensitive to frequency variations. Its form for pure sinusoidal inputs, disregarding all input harmonics that reappear in the output,[3] is

$$G_t(x_1) = 1 - (2/\pi)\sin^{-1}(a_t/x_1) + (2a_t/\pi x_1)\sqrt{x_1^2 - a_t^2} \quad (3)$$

where $a_t$ is the threshold level and $\pi/4$ rad. per sec. is the angular slope of the threshold characteristic curve.

The reaction-time element will have the known transfer function

$$x_3(s)/x_2(s) = C_r(s) = e^{-\tau s} \quad (4)$$

where $\tau$ is the time delay.

Because "bias" is instantaneous (reflexive) and conveys, primarily, error-direction information, it is approximated by a step function of alternate polarity, depending on the sign of the error signal. Fig. 3 is a diagram for derivation of the describing function for bias. The describing function for sinusoidal inputs[3] is

$$x_4/x_1 = k_bG_b(x_1) = \lim_{a\to 0}[(4k_b/\pi x_1) \times \sqrt{1 - (a^2/x_1^2)}] = 4k_b/\pi x_1 \quad (5)$$

The system kinesthesis, or neuromuscular loop, unlike the mental computation, threshold, reaction time, and bias characteristics, requires the participation of the pilot's biomotor system. The elasticity, damping, and inertia common to motor systems with an output load (hand and arm) with appropriate active elements (muscles) are characteristic of this system. A second-order transfer function, therefore, was used to approximate the forward part of the neuromuscular loop:

$$x_5'/x_3 = k/(ms^2 + ns + 1) \quad (6)$$

where $x_5'$ is the neuromuscular output.

Eq. (6) does not allow for neural feedback. Normally, a physiological loop is closed around the motor system. Open-loop operation indicates a pathological phenomenon called ataxia,[4] a condition in which the effector elements, though normal, are not monitored by the central nervous system. Continuous monitoring of the effectors is centered on the pick-off action of proprioceptors, which are rudimentary end-organ receptors of stimuli caused by the contraction of muscle fibers. Proprioceptors are distributed throughout the muscles and joints to permit internal feedback of data such as control-stick-feel pressure.

The neuromuscular feedback system involves a measurable amount of neural-transmission lag (see Fig. 4). The transfer function for kinesthesis, then, is

$$\frac{x_5}{x_3} = G_m(s) = k_m\left(\frac{ls + 1}{Ms^3 + Ns^2 + Ls + 1}\right) \quad (7)$$

The proprioceptors sense differences in pressure or force, so the error signal, $x_5$, as well as its associated signals, $x_4$ and $x_6$ (see Fig. 1), should have the dimensions of force or pressure. The element representing control-stick-deflection sensitivity, $k_0$, then should provide the error signal with the ratio of control-stick displacement to control-stick force so that the pilot's motor characteristics can be accurately simulated.

Frequency components that are not linearly related to the stimulus pattern have been observed in the human response by Tustin[5] and others. Generally, such "noise" has been attributed to nonlinear operations, such as the threshold element. The Navy jet pilots who participated in this project, however, exhibited steady hand oscillations, or information feedback,[4] in varying amounts. The oscillation, superimposed on the basic discontinuous servo type signal representing pilot hand motion, was nearly sinusoidal with a frequency near 1.4 cps. As long as the pitch disturbance was anticipated by the pilot, it persisted,

even during intervals of no disturbance. The oscillation stopped only after the disturbing signal was turned off.

Because the steady hand oscillations were unmistakably observed in the performance of jet pilots, the methods of piloting high-speed airplanes were examined to determine the cause. Piloting requires a knowledge of the airplane's performance especially at high speeds; thus, the pilot must familiarize himself with the performance characteristics of his airplane with respect to the air mass and other environmental conditions during high-speed operation. In continuously attempting to acquire this knowledge, the pilot imparts a succession of short, fast impulses to the control stick. Although these oscillations do not deflect the airplane from its course, they provide the pilot with a kinesthetic sense of the status of his control over the airplane.

The pilot of a high-speed airplane is particularly concerned with changes in the g force, which occur when the control stick is deflected or the throttle setting changed. Apparently, the oscillatory hand motion observed in the performance of the jet-interceptor pilots who participated in pilot analog tests was an informative feedback process used to inform the pilot of the number of gs he could safely withstand at any moment, and, therefore, of how much control-stick deflection he could afford without danger. The participating pilots, attributed the oscillatory motion to a desire for continuous awareness of their control of the aircraft so they would be prepared for the next required corrective maneuver. A constant amplitude oscillation of frequency $f_0 = 1.4$ cps was added to the kinesthesis output in the pilot analog design to represent informative feedback; this oscillation only approximates the phenomenon, but it was necessary to duplicate the appearance of the pilot's hand motion even though the effect of informative feedback on the pitch error signal is relatively small. Too little is known about the oscillatory motion for a cross modulation with the pitch-error signal.

Informative feedback, as it is incorporated in the analog, may be represented by the following:

$$x_6(s) = D[(\omega_0 + c)/(s^2 + \omega_0{}^2)] \tag{8}$$

where $\omega_0 = 2\pi f_0 \cong 8.8$ rad. per sec.
$c$ = function of phase angle

Based on the equations formulated for the mental and physiological functions involved, an equation can be derived to represent the overall input-output relations of the pilot analog. To the extent that the analog's performance duplicates that of the pilot in a given situation (sinusoidal input disturbance), this equation can be considered the pilot equation for that situation. The equation is derived herein to provide an analytical description of the analog. Its use for closed-loop analysis of the pilot-aircraft system is limited because of the restrictions on the describing function method.

For the pilot analog shown in Fig. 1, the describing function is

$$\delta_{ef}(s) = k_0G_s(s)\ [G_tG_r(s)G_m(s) + k_bG_b]\theta_{wp}(s) + D[(\omega_0 + c)/(s^2 + \omega_0{}^2)] \tag{9}$$

where $\delta_{ef}$ is the control-stick force and where the expressions for the functions $G$ are given by Eqs. (1) through (8). The eight parameters—$k_0$, $k_1$, $k_2$, $k_3$, $\tau$, $a_t$, $k_b$, and $D$—represent the variable quantities in the pilot dynamic system and have different values for different individuals.

### *Design of Pilot Analog Circuit*

In contrast to the analytical expression for the pilot analog, the simulation circuit is much more general in that it is valid for any input signal, $\theta_{wp}$. The circuit diagram for the pilot analog is shown in Fig. 5.

The first pilot operation is mental computation of a linear corrective signal. The threshold characteristic is represented by placing a conventional dead-zone circuit ahead of an absolute-value circuit, which flips a high-gain, prebiased amplifier to a state of polarity opposite to its normal state. This amplifier and the one immediately following it activate the electronic switch, S, when the error signal, $\theta_{wp}$, exceeds the preset (threshold) level. The switch consists of four diodes in a series-parallel connection. As long as points A and B are under negative and positive voltages, respectively, the diodes are cut off; when the polarities of these points are reversed, the diodes conduct, and the output of the mental computation circuit is fed to the reaction-time circuit.

The reaction-time circuit provides the values of $G_r$ as stated in Eq. (4). This function[6] can be approximated by

$$e^{-\tau s} \cong \prod_{n=1}^{r} [(1 + 2\zeta_n\tau_n s + \tau_n{}^2s^2) \div (1 + 2\zeta_n\tau_n s + \tau_n{}^2s^2)] = \exp\left[-\sum_{n=1}^{r} 4\zeta_n\tau_n\right] \tag{10}$$

where $r$ is an integer, and its value, when applied to the simulation, must be finite and small to avoid complexity. The approximate simulation of $G_r$ is accomplished by use of three amplifiers as shown in the circuit diagram (see Fig. 5). Fig. 6 shows the performance of the reaction-time circuit for $\tau = 0.20$ sec.

Certain factors limited this simulation of a pure reaction time. The most obvious of these is the response of the circuit to a step input. The instant a vertical wave is applied to the circuit, a high-frequency transient oscillation is initiated; it dies out, however, before the time-delay interval has elapsed. The error is of little consequence because of its short duration, its rarity (airplane attitude disturbances seldom occur as sudden steps), and because the low-pass characteristic of the airplane system filters out the greater part of the oscillation.

A second error is significant because, by coincidence, it is of the same order of magnitude as the neuromuscular lag. This error appears as a time lag causing a change in the slope of the wave form that passes through

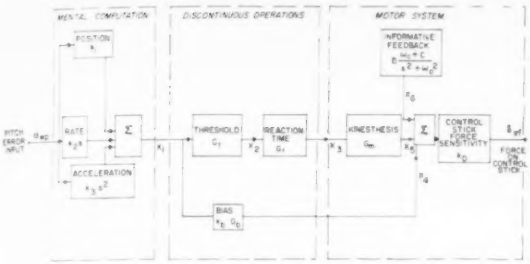


FIG. 1. Block diagram of pilot analog system.

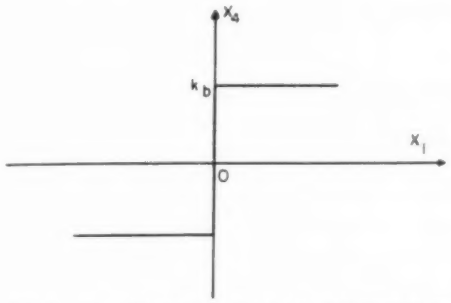


FIG. 3. Describing function for bias characteristic.

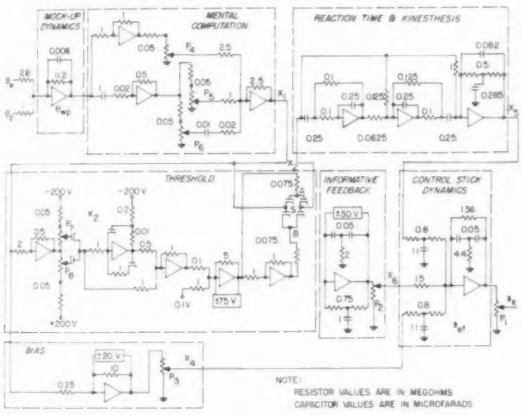


FIG. 5. Circuit diagram of pilot analog.

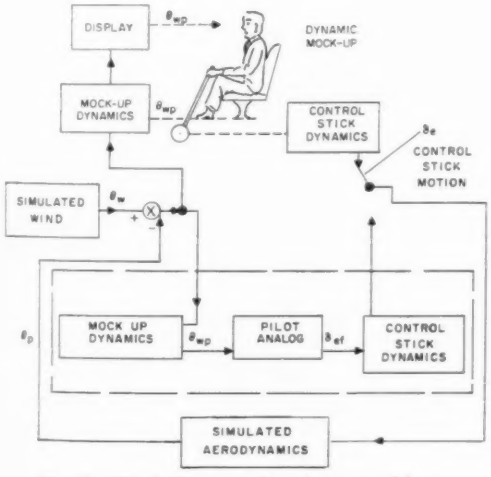


FIG. 7. Block diagram of analog control loop.

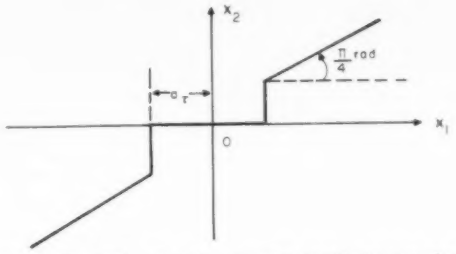


FIG. 2. Describing function for threshold characteristic.

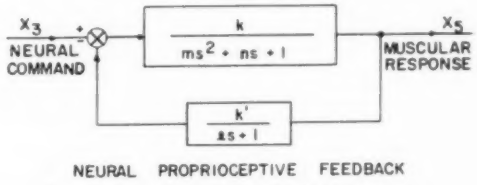


FIG. 4. Neuromuscular closed-loop system.

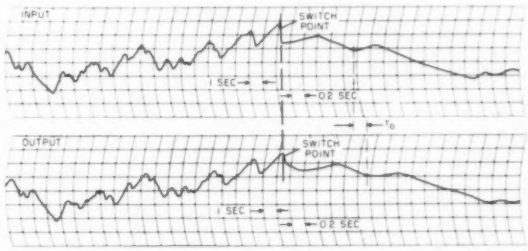


FIG. 6. Recorded response of reaction-time circuit.

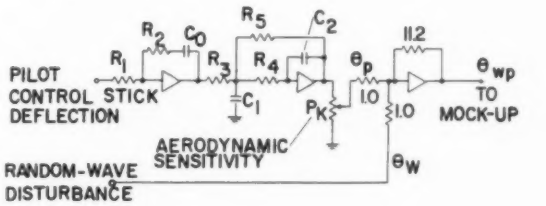


NOTE:
THE FOLLOWING VALUES CORRESPOND TO F-89 B JET INTERCEPTOR COEFFICIENTS, RESISTOR VALUES IN MEGOHMS, CAPACITOR VALUES IN MICROFARADS:

$R_1 = 0.41$
$R_2 = 0.73$
$R_3 = 0.40$
$R_4 = 1.15$
$R_5 = 1.0$

$C_0 = C_1 = 1.0$
$C_2 = 0.05$
$P_K$ = ONE-THIRD OF MAXIMUM POTENTIOMETER SETTING

FIG. 8. Circuit diagram of pitch-error-signal generator.

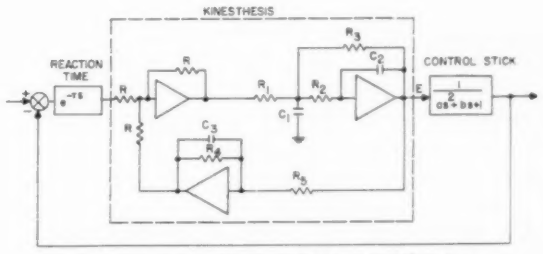


FIG. 9. Circuit diagram of kinesthesis system.

the reaction-time circuit. The feedback impedance of the last amplifier in the reaction-time circuit, which otherwise would have provided a pure resistance, was trimmed to permit the use of this error for the simulation of neuromuscular lag.

Both errors are caused by the limited number of stages used in the reaction-time simulation. This part of the analog circuit is being improved through incorporation of a device for simulating pure time delays based on an entirely different concept.

Bias was represented by a high-gain operational amplifier with an adjustable, limited output. Informative feedback was provided by a one-amplifier oscillator of the parallel-T, phase-shift type with output amplitude fixed by a diode-limiter circuit.

## (3) Analog Control Loop Development

### *General*

The most illuminating test of the pilot analog circuit is its operation in parallel with human pilots in a simulated flight situation. The system arranged for this test included a simulated airplane and a simulated environment in addition to the pilot and his analog. The environment simulation was restricted to a wind disturbance that affected only the longitudinal attitude of the airplane. The simulated pitch disturbance was summed with the output of the airplane simulator to provide inputs, $\theta_{wp}$, to a dynamic cockpit mock-up. The pilot in the mock-up received realistic data on the disturbance through a display and through angular movement of the mock-up seat. He controlled the mock-up by means of a control column on his platform. The pilot's corrective motions provided inputs to the airplane simulator, and thus, completed the pilot-airplane loop. The analog, wired into the computer also containing the aerodynamics simulation, was activated by the same input signals, $\theta_{wp}$, provided to the human pilot. A single-pole, double-throw switch allowed instant switching of mock-up control from the pilot to the analog, and vice versa. Fig. 7 shows the test control loop.

### *Airplane Simulator*

The basic aerodynamic conditions presented were a pitch rate proportional to the elevator deflection and the damping characteristics of the F-89B jet interceptor. The simulation was simplified by omitting the long-period phugoid oscillation of the jet fighter because only relatively short-term transients characterized the simple task. It was assumed that the airplane maintained a 5,000-ft. altitude and a constant forward velocity of 560 ft. per sec. The airplane simulator was based on the following transfer function:[7]

$$\frac{\theta_p}{\delta_e} = \frac{1.97(0.73s + 1)}{s[(0.24)^2s^2 + 0.24s + 1]} \tag{11}$$

where $\theta_p$ is the pitch angle caused by the elevator deflection, $\delta_e$.

Fig. 8 shows the circuit used to generate pitch-offset signals continuously on a one-to-one time scale. The circuit is based on the transfer function

$$\frac{\theta_p}{\delta_e} = \frac{-(R_5/C_6R_1R_3)\ (R_2C_6s + 1)}{s\{R_4R_5C_1C_2s^2 + [R_4 + R_5 + (R_4R_5/R_3)]\ C_2s + 1\}} \tag{12}$$

As in the simulation of the pilot, resistor and capacitor values were selected to obtain the numerical translation for the physical system.

The cockpit mock-up is a hydraulically driven platform on which are mounted a bucket-type seat, a control column, and a cathode-ray tube. The platform has one degree of freedom, with a maximum angular deflection of 12°. The bucket seat can be oriented to face the mock-up axis, for roll motion, or perpendicular to the axis, for pitch motion. Angular motions of the mock-up seat are generated by an electronic analog computer as functions of pitch or roll angles. The cathode-ray tube provides a visual display of an artificial horizon. The prime mover is a 1,000-psi, 5-hp. hydraulic pump (Vickers T3-FAI-262), and the servo-control valve is a high-quality aviation type (Moog V-4). A conventional d. c. servoamplifier, incorporating a 400-cps oscillation to avoid valve friction, energizes the control valve.

The frequency response of the dynamic mock-up loop with a 200-lb. weight in the seat, is essentially flat to 1.5 cps and is decreased by 3 db. at 2.3 cps for the peak-to-peak input of a 5° pitch angle. The overall multiloop system—amplifier, valve actuator, and platform—has a transfer function comprising two second-degree and two first-degree polynomials in the Laplacian variable $s$. These are contributed, respectively, by the platform structure, the hydraulic actuator, the control valve, and the amplifier-input filter. The amplifier-input filter is by far the most significant as far as the response is concerned because of its low cut-off point, which provides a safety measure against the possibility of high mock-up accelerations.

The effective transfer function for the mock-up is

$$\theta_{wp}/\theta_p = k/(0.0675s + 1) \tag{13}$$

where the filter time constant, $\tau_f$, is 0.0675. The transfer function is incorporated in the simulation (see Fig. 5) by means of a condenser in the feedback branch of the first amplifier.

An elaborate instrument simulation, which is characteristic of most operational flight trainers, was unnecessary for this application because the only type of performance investigated was the continuous control of a single variable. The only visual instrument used, therefore, was a 5-in. cathode-ray tube masked to the size and shape of a typical gyro-horizon indicator. The scope trace, at the horizontal position during level flight, was deflected vertically to indicate pitch errors.

The control stick used in the mock-up was a 30-in. length of hollow tubing fitted with a jet-interceptor

handgrip. Only one degree of freedom was studied during a given run, but the control stick could be placed in either of two positions, corresponding to the respective seat orientations.

Control linkages and constant loads were physically simulated in the mock-up by standard airplane cables, which were attached to the control stick and loaded by adjustable inertial, spring, and viscous drag forces. A modified viscous damper of the type used in some aircraft was employed. The control-column structure did not include a control-stick-feel effect adequate for simulation of the aerodynamic forces reflected from the control surfaces during maneuvering. Consequently, the control column dynamics can be expressed by the transfer function

$$G(s) = 1/(as^2 + bs + 1) \tag{14}$$

Experiments with the control column yielded the following values for coefficients $a$ and $b$ under a standard control column adjustment of 0.8$g$ per inch:

$$a = 0.015 \text{ sec.}^2 \quad \text{and} \quad b = 0.44 \text{ sec.} \tag{15}$$

Incorporation of the factors represented by Eqs. (14) and (15) complete the simulation.

The control column dynamics simulation must follow the commands of the pilot analog in the same manner the actual control stick responds to the commands of the human pilot for accurate comparisons of the responses of the pilot and his analog. The control-stick dynamics are shown in Fig. 5 as the last circuit of the simulation.

The entire simulation apparatus, with the exception of the computer and the recorder, was placed in an air-conditioned lightproof room for isolation from extraneous disturbances and space reference cues. A dim illumination of the oscilloscope screen and of the room reduced eye fatigue.

### *Wind Simulator*

The independent input variable, $\theta_w$, used to disturb the system and produce simulated wind gusts, was obtained by application of principles similar to those employed to simulate noise.[8] A random wave generator, with a sample of radioactive material at its heart, emitted particles at a rate defined by a Poisson distribution.[9] A self-quenching counter tube (Geiger-Muller) and associated circuits, energized by the particles, produced pulses when the particle-energy exceeded a preset level. After amplification, the pulses triggered a bistable multivibrator, which generated square waves of constant amplitude. The square waves, amplified again in the computer and clipped symmetrically to assure a zero mean value, provided randomly timed zero crossings.

Because the zero crossings follow a Poisson distribution, the associated power spectrum is easily determined and can be altered, by filtering, to make the wind disturbance more realistic. Mock-up tests with subjects experienced in both jet and conventional airplane piloting provided parameter values for the filter, which included only one time lag.

## (4) Pilot Analog Tests

### *Analog Settings*

The analog parameters seem so numerous that their isolation and setting, at first glance, appear to be prohibitive tasks. However, certain simple measurements, taken under controlled conditions, provide parameter values for at least three analog components: threshold level, reaction time, and neuromuscular lag.

Measurements were made with a test subject in the dynamic mock-up. The mock-up was designed so that the distance between the subject's eyes and the face of the cathode-ray-tube horizon display was 36 in. The scope deflection gain was adjusted so that the horizon deflection, with respect to the eye, was one-third that of mock-up tilt. Thus, when the mock-up was tilted 6 deg., the horizon deflection, as shown on the scope, was 1.25 in. The display adjustment was established on the basis of the subjective judgment of several experienced pilots.

Measurements for the threshold level were determined by subjecting the mock-up to randomly spaced step inputs of small amplitude. The points at which the pilots made corrective responses were established, and an average of these points was taken. The average was used as a starting point from which the threshold level required for each subject could be set.

The reaction-time parameters also were investigated by observing pilot response to unpredictable step input disturbances of amplitudes well above the threshold level. These trials revealed a marked variance in reaction times, even for the same person. Reaction-time values were found to follow a skewed distribution,[10] with the longer tail of the curve extending toward the longer time values. The most probable value emerging from such distributions and that generally accepted is $\tau = 0.25$ sec. However, the task involved in this study required a complex of stimuli, presented simultaneously, all of which incurred the same response. As a general rule,[2] the more intense the stimulus, the shorter the reaction time. Because the stimuli complex presented to incur pilot pitch-control motions was equivalent to an intense single stimulus, the reaction time of efficient jet pilots can be figured as low as $\tau = 0.20$ sec.

The experiments in kinesthesis (or neuromuscular lag) were not rigorous enough to satisfy the meticulous analyst but are adequate for the objectives of the study. A step input was presented to the pilot by the visual display only. The platform remained horizontal and stationary. A direct feedback loop was established between the control column output and the display. The step amplitude was held well above the threshold level so that the threshold effect could be neglected, and it was assumed that the mental-computation transfer function can be represented by a pure gain. To permit this approximation, the rate and

acceleration associated with the input were held so high, by means of the step signal, that they always were above the upper limits of pilot perception. Consequently, the pilot analog control loop comprised only the reaction time, exp $(-\tau s)$; the control column dynamics, $G(s)$; and the kinesthesis, $G_m(s)$; of which the first two components were known.

After several oscillographic recordings were made, an average response curve was established. A supplementary simulation of the loop (see Fig. 9) was set up, and the parameters of the kinesthesis block were determined by a trial-and-error procedure in combination with curve-fitting techniques. The following values of the constants given in Eq. (7) were obtained: $l = 0.05$, $M = 0.00022$, $N = 0.00672$, and $L = 0.0983$.

### *Analog Performance*

The primary purpose of the experimental and theoretical work that led to the development of the pilot analog for airplane pitch control was to evaluate jet pilots' control abilities as affected by the dynamic characteristics of the airplane and the control column. Four jet interceptor pilots recently active in fleet duty served as test subjects. The study provided an excellent opportunity to attempt the simulation of the human link in a closed loop system in which all other factors already were represented in a dynamic mock-up or electronically. The pursuit of these tasks revealed answers to several questions regarding a man-machine (pilot-aircraft) system for a continuous rate control function.

The pilots performed routine ten-minute flights. Pitch error signals were fed to the pilot analog and to the dynamic mock-up servo and display (see Fig. 1). The observer could record (1) the pitch error, (2) the pilot's hand motions, and (3) the simultaneously generated outputs of the pilot analog.

Analog parameters (mental computation, bias, and informative feedback) could be adjusted until differences between the two outputs were negligible without interfering with the pilot's control of the loop. Control of the mock-up could be switched to the analog without the pilot's knowledge (see Fig. 7). When the pilot did not detect the substitution of the analog for himself in the control loop, the analog was considered representative of his dynamics.

One might suspect that the human pilot's output wave forms would be too inconsistent to permit precise judgment on the nature of the required analog adjustments. Such inconsistency, however, was seldom observed in the experienced subjects who participated in these tests. Although data on their average accuracy, as indicated by the root mean square pitch error, showed variance, the modes of operation among pilots were similar and were consistent in individuals. Only inexperienced subjects exhibited occasional control-stick reversals that the analog, having no comparable component for unreliability, could not simulate.

The five oscillographic recordings, each of which encompasses approximately 40 sec. of "flight" time, are shown in Figs. 10 through 12 as typical of similar recordings obtained in more than 80 hours of "flight." The recordings illustrate the correspondence of outputs of three pilots and their analog circuits for standard aerodynamic settings [see Eq. (12)].

The response of the light-airplane pilot (Fig. 10) was typical of that recorded for pilots without previous experience in jet airplane control. Compared to Jet Pilot No. 1 (Fig. 11), he showed little or no informative feedback. It is uncertain, however, whether he originally exhibited the characteristic and gradually abandoned it or whether it was lacking completely, for the light airplane pilot participated in mock-up tests before the pilot analog was completed. The informative-feedback habit is superfluous in mock-up "flight" and eventually is abandoned, even by jet pilots.

The light-airplane pilot also frequently exceeded the mock-up pitch range typical of the jet pilots. Evidence of his poorer performance was confirmed by his efficiency recording (root mean square pitch error), which showed 25 per cent less smoothing of the random disturbance than that achieved by the jet pilots. Pilot efficiency was checked by use of the modified analog circuit shown in Fig. 13.

Jet Pilot No. 1 (see Fig. 11) exhibited more informative feedback than the other subjects. He was more active, also, in other respects, and was the only subject who fatigued control-column linkage supports and overstressed the mechanism. Despite his high rates of control-stick motion, the effects of informative feedback are scarcely perceptible in this pilot's mock-up pitch record. Pilot No. 1 showed excellent control of the mock-up during the run shown in Fig. 11.

Jet Pilot No. 2 (see Fig. 12) was the least consistent of the four Navy pilots. His informative feedback level was less pronounced, and his control efficiency was higher than that of the light airplane pilot. The recording (Fig. 12) was made with standard aerodynamic parameters, so estimates of the effects of system parameter variations could be based on a comparison of Figs. 12 and 14. In Fig. 14 aerodynamic damping was reduced from the normal value of critical damping (0.5) to 0.2. The other parameters remained constant. The pilot-airplane oscillation, a notably slower oscillation than that of informative feedback, is evident. The same pilot's hand motion for a flight situation in which aircraft sensitivity was reduced 50 per cent is shown in Fig. 15. The average amplitude of the pilot's control-stick motion increased to compensate for the decreased system gain. Instability was noted but not as continuously as in the recording shown in Fig. 14.

The remarkable similarity of actual and simulated pilot hand motions, as recorded by the oscillograph, proves that the pilot analog system is representative of an "average" pilot's dynamics for the simple control task involved.

The effects of human adaptation, on learning, on early performance can be observed in tests similar to those used to check the pilot analog design. Learning effects normally are transient as they occur during that

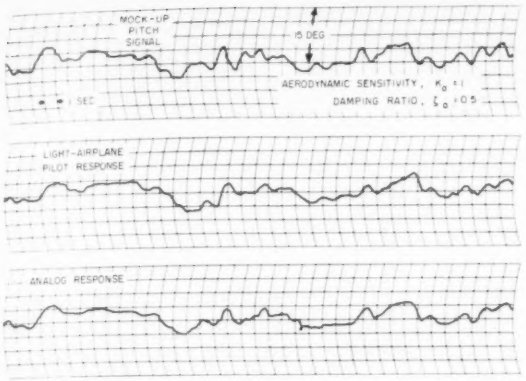


FIG. 10. Oscillograph recording—responses of light-airplane pilot and analog to mock-up pitch.

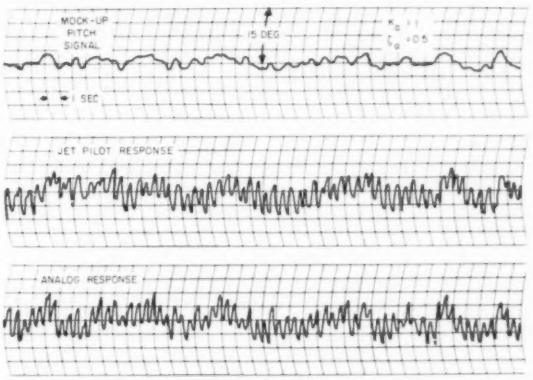


FIG. 11. Oscillograph recording—responses of Jet Pilot No. 1 and analog to mock-up pitch.

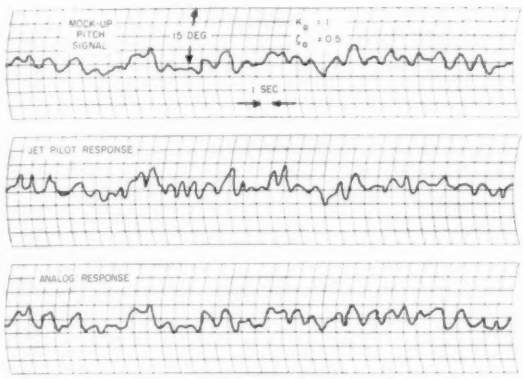


FIG. 12. Oscillograph recording—responses of Jet Pilot No. 2 and analog to mock-up pitch.

$$E = \frac{1}{T}\int_0^T (\theta_w^2 - \theta_{wp}^2)\,dt \quad \text{WHERE } T \geq 10 \text{ MIN}$$

EFFICIENCY CRITERION EQUATION

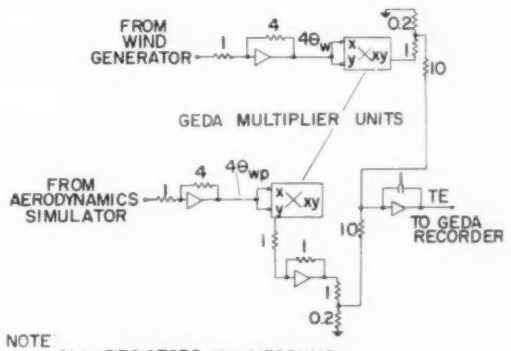


NOTE
ALL RESISTORS IN MEGOHMS
ALL CAPACITORS IN MICROFARADS

FIG. 13. Pilot efficiency test circuit.

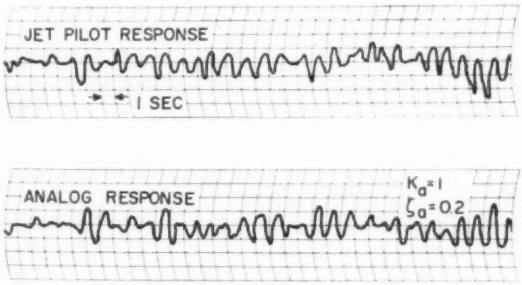


FIG. 14. Oscillograph recording—responses of Jet Pilot No. 2 and analog to signal with reduced aerodynamic damping.

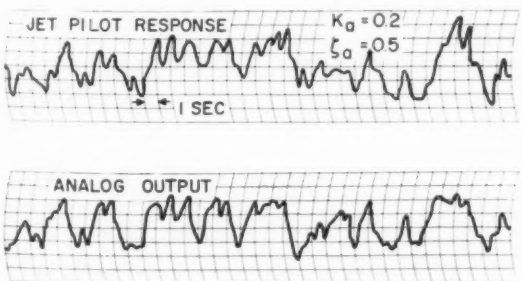


FIG. 15. Oscillograph recording—responses of Jet Pilot No. 2 and analog to signal with reduced aircraft sensitivity.

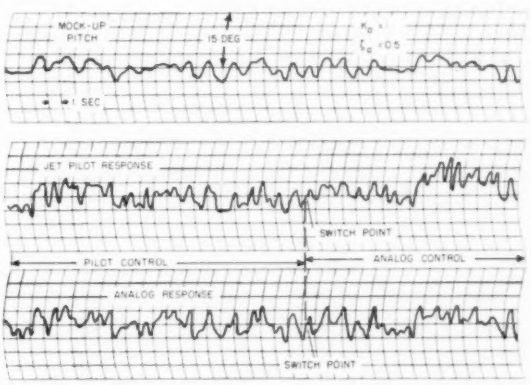


FIG. 16. Oscillograph recording—pilot-pilot analog substitution test.

TABLE 1

Typical Pilot Analog Parameter Settings

| Analog Parameter | Potentiometer | Adjustments Required for Test Subjects —(Fraction of Full-Scale Setting)— Light-airplane pilot | Jet pilot 2 | Jet pilot 3 | Jet pilot 4 |
|---|---|---|---|---|---|
| Position gain, $k_1$ | $P_4$ | 0.530 | 0.150 | 0.600 | 0.600 |
| Rate gain, $k_2$ | $P_5$ | 0.300 | 0.600 | 0.600 | 0.600 |
| Acceleration gain $k_3$ | $P_6$ | 0.300 | 0.400 | 0.600 | 0.600 |
| Threshold level, $a_t$ | $P_7$, $P_8$ | 0.750 | 0.040 | 0.075 | 0.075 |
| Bias, $k_b$ | $P_3$ | 0.200 | 0.300 | 0.500 | 0.400 |
| Informative feedback, $D$ | $P_2$ | 0.025 | ... | 0.100 | ... |
| Deflection sensitivity, $k_0$ | $P_1$ | 0.100 | 0.080 | 0.075 | 0.080 |

initial period of somewhat unpredictable exploration when the pilot is familiarizing himself with the machine. This type of study was possible because analog parameter settings could be adjusted to suit the individual and could be changed to account for day-to-day differences in individuals. (See Figs. 10, 11, 12, 14 and 15.)

The naturalness of the control effected by the analog, when successfully adjusted, is indicated in Fig. 16. After Jet Pilot No. 3 had been "flying" the mock-up for several minutes, control was switched to the analog without his knowledge. The pilot, completely unaware of the trick, continued to move the control stick in response to the pitch stimuli.

Table 1 shows parameter settings with the corresponding analog circuit elements (see Fig. 5). Informative feedback data are incomplete because the jet pilots, although they carried this habit of their normal flight experience to mock-up "flight," gradually abandoned it as they grew more accustomed to test conditions. The gradual reduction of the informative feedback oscillation was observed in the responses of three jet pilots. The fourth pilot showed no tendency toward abandoning it even after eighty ten-minute trials. The trait may have disappeared, however, if the tests had been continued.

An interesting feature regarding the experimental extinction of informative feedback was noted in tests of the third jet-pilot test subject. Particular care was taken to measure the amount of informative feedback present in his control-stick oscillations when the characteristic had been observed consistently in earlier trials. The data obtained by measuring adjustments in the proper potentiometer of the analog for his day-to-day performance were analyzed, and his gradual abandonment of the informative feedback habit proved to be an exponential function of time.[1]

## (5) Conclusions

Although tests of the pilot analog for airplane pitch control were limited by the simplicity of simulated conditions and by the relatively small sample of test subjects, the analog adequately fulfilled the objectives for which it was designed. Its accuracy in matching pilot hand motions was proved when active Navy jet pilots failed to detect immediately its substitution for themselves in an applicable control loop.

The analog was designed to account for pilot adaptation to new situations as well as for individual differences. Its usefulness as an aid in human dynamics research, as a result of its versatility in these respects, was demonstrated, at least for the one task involved. Evidence of the human pilot's rapid adaptation characteristics was exhibited when jet-pilot test subjects quickly accustomed themselves to the dynamics of the system.

Thus, it can be concluded that the human operator, while performing a continuous rate-control task (such as the control of a pitching airplane), is capable of rapid self-adaptation to compensate for a new system dynamics—at least in instances where no other tasks are involved or where system dynamics do not change rapidly.

By simple adjustment of pilot analog potentiometers, researchers could determine differences in individuals as well as among pilots. Psychologists measured differences in experience and training by measuring the adjustments required. It was discovered, for instance, that a pilot's use of information conveyed by the time derivatives of an error increases with experience and training.[11]

Analog tests also revealed that the control motions of jet pilots for the informative feedback process are remarkably consistent in individuals and even from pilot to pilot. Thus, the premise that a pilot simulator equivalent to any given pilot can be developed, even though nonlinearities are involved, is justified. Moreover, such evidence of pilot consistency indicates that an analog computer circuit can be evolved to simulate the control motions of an "average" pilot at a given level of training.

It was found that pilot-induced informative feedback is a significant part of the output energy of some jet interceptor pilots. Previously attributed to noise originating from nonlinear operations, oscillations were repeatedly detected in jet-pilot hand motions as a signal superimposed on the basic signal of pilot control and, after considerable investigation, were proved to be a pilot's means of keeping himself informed of the status of his control over the airplane.

The control efficiency of the human operator also can be determined, to some extent, by using a modified analog circuit. When the airplane system parameters do not vary by more than two from a given set of standard parameters, the pilot analog circuit can be employed to obtain a first approximation to the root mean square control efficiency of the test subject. Higher order approximations of pilot control efficiency would be of doubtful value unless supported by intensive study of the self-adaptation and informative-feedback phenomena. Thus, the development of airplanes with low-pass aerodynamic response involves considerable risk unless the source and full effects of these characteristics are first determined.

(*Continued on page 394*)

# Theoretical Considerations of Flutter at High Mach Numbers

HOMER G. MORGAN,* HARRY L. RUNYAN,** AND VERA HUCKEL***

*Langley Aeronautical Laboratory, NACA*

SUMMARY

Some of the theories for two-dimensional oscillatory air forces which may be applied in flutter calculations at high Mach Numbers are discussed. These include linear theory, Van Dyke's second-order theory, piston theory, Landahl's method, tangent-wedge and tangent-cone approximations, Newtonian theory, and a new nonlinear-pressure method. A comparison of the theories is made by showing the results of flutter calculations for Mach Numbers up to 10, and the possibility of flutter at these higher Mach Numbers is pointed out.

Results of flutter calculations are shown to illustrate the various effects arising from a nonlinear thickness theory. The possibility of large flutter speed thickness effects which depend on frequency ratio is shown. The influence of airfoil shape is discussed and flutter speed trends with center of gravity and elastic axis locations are presented. Some possible refinements of piston theory are discussed for use at very high Mach Numbers. These include the use of local flow conditions and the use of Newtonian theory over the leading edge of a blunt-nosed airfoil.

## SYMBOLS

| | |
|---|---|
| $a$ | = speed of sound, ft./sec. |
| $b$ | = semichord, ft. |
| $c$ | = chord, ft. |
| $C_L$ | = lift coefficient |
| $C_p$ | = pressure coefficients, $(p - p_0)/(\rho V^2/2)$ |
| $f$ | = instantaneous airfoil-surface location, ft. |
| $h$ | = wing vertical displacement at elastic axis, ft. |
| $I_\alpha$ | = mass moment of inertia of wing section per unit width, lb.-sec.$^2$ |
| $k$ | = reduced frequency, $b\omega/V$ |
| $\bar{L}_i, \bar{M}_i$ | = $(i = 1, 2, 3, 4)$ oscillatory total lift and moment derivatives defined as in reference 2 |
| $m$ | = mass of wing section per unit width, lb.-sec$^2$/ft.$^2$ |
| $M$ | = Mach Number |
| $p$ | = pressure, lb./sq. ft. |
| $p_0$ | = free-stream pressure, lb./sq. ft. |
| $r_\alpha^2$ | = $I_\alpha/mb^2$ |
| $t$ | = time, sec. |
| $V$ | = velocity, ft./sec. |
| $w$ | = downwash velocity, ft./sec. |
| $x, y; \xi, \eta$ | = Cartesian coordinates, ft. |
| $x_g$ | = distance from elastic axis to center of gravity, positive aft, fraction chord |
| $x_0$ | = elastic axis location, fraction chord |
| $Y$ | = airfoil surface, measured from airfoil mean line, ft. |
| $\alpha$ | = angle of attack, rad. |
| $\beta$ | = $\sqrt{M^2 - 1}$ |
| $\gamma$ | = ratio of specific heats |
| $\mu$ | = mass ratio for a wing section, $m/4b^2\rho$ |
| $\bar{\mu}$ | = mass ratio for a cone, (total mass/$8b^3\rho$) |
| $\rho$ | = air density, slugs/ft.$^3$ |
| $\tau$ | = airfoil thickness, fraction chord |
| $\phi$ | = velocity potential |
| $\theta$ | = cone semiapex angle, rad. |
| $\omega_h$ | = circular bending frequency, rad./sec. |
| $\omega_\alpha$ | = circular torsion frequency, rad./sec. |
| $\bar{\omega}$ | = $2kM^2/\beta^2$ |

Presented at the Aeroelasticity—II Session, Twenty-Sixth Annual Meeting, IAS, New York, January 27–30, 1958.

* Aeronautical Research Engineer.

** Head, Dynamic Loads Analysis Section.

*** Mathematician.

## INTRODUCTION

THE STRUCTURES of high-speed aircraft and missiles are, of necessity, designed for maximum load-carrying efficiency. This implies minimum weight to sustain a given load and often results in a structure which is relatively flexible, thus inviting such aeroelastic problems as flutter and divergence. Also, certain nonlinear effects in the aerodynamics, of comparatively small importance at subsonic speeds, can have destabilizing influences on these aeroelastic problems at high speeds.

Unsteady aerodynamic theory and the oscillatory aerodynamic forces needed for flutter calculations have received much attention in the supersonic speed regime. Correspondingly, little effort has gone toward extending this work into the high supersonic and hypersonic speed regions, and few applications to flutter have been made. However, there are several methods available or adaptable for calculating unsteady aerodynamic forces in this speed range.

It is the purpose of this paper to discuss and to attempt to bring into perspective some of the aerodynamic theories that are available at high supersonic speeds and to show their application to flutter calculations. The theories to be discussed are the Van Dyke second-order theory, piston theory, linear theory, the Landahl extension of piston theory, Newtonian theory, tangent-wedge approximation for hypersonic flow, and a new theory based on the use of the nonlinear-pressure expression.

These various theories will be compared and discussed with reference to their adequacy for prediction of aeroelastic effects. In addition, some flutter trends at high Mach Number will be discussed.

## HIGH MACH NUMBER AERODYNAMIC THEORIES

Before discussing some of the high Mach Number aerodynamic theories which are available for aeroelastic calculations, some general comments will be made.

The basis for many supersonic flutter calculations has been the work of Garrick and Rubinow.[1] This method has proved to be very useful in the low supersonic speed region and is based on linearized two-

dimensional aerodynamic theory. Linearized theory has also been used to study three-dimensional aspect ratio and plan-form effects in the supersonic region. For example, references 2 and 3 treat special plan forms while reference 4 presents a method for handling an arbitrary plan form.

Several attempts have been made for an improved supersonic aerodynamic theory which will account for all or part of the nonlinearities not treated by linear theory. These nonlinearities appear in the aerodynamic forces as the result of airfoil shape, thickness, boundary layer, Reynolds Number, finite shock waves, etc. Although the general problem is largely untouched, some of these effects have been studied. For example, Carrier's work in reference 5 examines the effects of the bow shock wave on an oscillating wedge. Several methods are available which include an effect of airfoil shape and thickness. For example, Jones and Skan[6] used a numerical integration technique to predict forces and moments on a biconvex airfoil. Van Dyke[7] found a second-order solution for unsteady flow by a method of successive approximations. His solution is related to linear theory for the oscillating case as Busemann's solution is related to that of Ackeret for the steady case.

To reconcile certain discrepancies which existed between the results of Van Dyke and some previous writers, Lighthill,[9] reasoning from a suggestion by Hayes,[8] presented a check at high Mach Number which verified the solution of Van Dyke. This proposal by Lighthill, since called piston theory, has proved to be a very valuable flutter tool in itself and has been discussed in this light by Ashley and Zartarian in reference 10. Piston theory is especially attractive for flutter calculations because of its simplicity in comparison with other supersonic theories. Piston theory not only agrees with linear theory at high Mach Numbers but it is a bona fide high supersonic theory which agrees with the more exact second-order solution of Van Dyke when thickness terms are included.

By assuming large Mach Numbers, Landahl[11] has developed another nonlinear method by use of an iteration technique similar to that of Van Dyke. Second-order piston theory is a special case of this work.

Still another technique available for accounting for a portion of the nonlinearities of the supersonic flow problem involves using the linear velocity potential but retaining the pressure coefficient in its general second-order form. This technique will be referred to as the nonlinear-pressure method and will be discussed later.

The methods just discussed are to be applied in the supersonic and high supersonic speed regions. For purposes of this discussion, $M \simeq 4$ can be defined as being hypersonic. Piston theory, as originally suggested by Hayes in reference 8, is a hypersonic theory for slender profiles. The tangent-wedge approximation, discussed in reference 12, is also a hypersonic theory, similar to piston theory, and can be adapted for unsteady flow. Each element on the surface is assumed to be subjected to the pressure which would act on a semi-infinite wedge whose half-angle is the local slope. The pressure relation is derived by considering the oblique shock relations for large Mach Numbers and small angles.

Another procedure which involves the Newtonian approximation may also be used at hypersonic speeds. The flow region is assumed to be an infinitely thin layer lying between the shock wave and the airfoil. Local pressures are determined by the change in fluid momentum as it follows the airfoil contour.

The previously mentioned methods are for two-dimensional flow. A second-order three-dimensional theory is given by Leslie in reference 13, based on an iteration method similar to Van Dyke's. It is applied to a rectangular wing with a specialized thickness distribution, and static lifts and moments are calculated. The possibility is presented that this technique could be extended to the quasi-steady case for oscillatory derivatives.

In order to understand the relation between the various aerodynamic theories, some of those found useful for flutter calculations will now be discussed in more detail. Linear theory will not be reviewed since a large amount of literature is available.

### *Van Dyke's Method*

Van Dyke in reference 7 has presented a solution for the oscillating two-dimensional airfoil which is correct to second order. This solution contains the effects of airfoil shape and thickness on the forces and moments acting on the airfoil. By obtaining a solution correct only to second order, Van Dyke is able to work with the velocity potential equation. (Shock-wave effects enter as third-order terms so that to third order and higher a potential will not exist.) The second-order nonlinear perturbation equations which result are, for the velocity potential,

$$\phi_{yy} - \beta^2\phi_{xx} - 2(M^2/V)\phi_{xt} - (M^2/V^2)\phi_{tt} = M^2\{(\gamma - 1)\,[\phi_x + (1/V)\phi_t]\,(\phi_{xx} + \phi_{yy}) + 2\phi_x\phi_{xx} + 2\phi_y\phi_{xy} + (2/V)\,(\phi_x\phi_{xt} + \phi_y\phi_{yt})\} \quad (1)$$

and for the pressure coefficient,

$$C_p = -2\phi_x - (2/V)\phi_t + \beta^2\phi_x^2 - \phi_y^2 + 2(M^2/V)\phi_x\phi_t + (M^2/V^2)\phi_t^2 \quad (2)$$

The boundary conditions require that the flow be tangential to the airfoil surface.

The more familiar linear theory presented by Garrick and Rubinow, reference 1, results when the right side of Eq. (1) is set equal to zero and the product terms in the pressure coefficient, Eq. (2), are dropped. In the linearized theory, the tangency condition is satisfied at the mean line of the airfoil.

Van Dyke solves Eq. (1) by an iteration technique using the solution to the linearized equation as the first step. The linear solution is substituted in the right side of Eq. (1), giving a linear, nonhomogeneous differential equation which can be solved with the correct boundary conditions. Pressures are then found at the

airfoil surface from Eq. (2). Lift and moment coefficients are presented in reference 7 expanded in powers of a frequency parameter, up to and including the cube of frequency. In principle, the solution can be found for arbitrary frequencies, and reference 7 gives the result for a wedge oscillating about its vertex. However, the labor involved in finding the lift and moment on a general airfoil at arbitrary frequencies makes such a procedure extremely difficult. Nevertheless, the coefficients as presented to the cube of frequency should cover most flutter cases of practical interest.

Inasmuch as this method is based on the general potential flow equations, it is expedient to use this second-order solution as the standard of comparison for other theories at supersonic speeds.

### *Nonlinear-Pressure Method*

In Van Dyke's second-order solution, nonlinearities in the aerodynamic forces arise from two sources—the solution of the nonlinear velocity potential equation and from the nonlinear pressure coefficient. If it is assumed that contributions to the thickness terms by the nonlinear part of the velocity potential are small, a thickness effect can be found by using the linear velocity potential with the nonlinear pressure coefficient.

The linear velocity potential—i.e., the solution to Eq. (1) with the right side of the equation set equal to zero—is

$$\phi(x, t) = -(1/\beta) \times \int_0^x w(\xi, t)\, e^{(-i\bar{\omega}/c)(x-\xi)} J_0[(\bar{\omega}/cM)(x - \xi)]\, d\xi \quad (3)$$

where $w(\xi, t)$ is the downwash at the mean line of the airfoil and the boundary conditions are satisfied as $y$ approaches zero. However, downwash $w(\xi, t)$ can be interpreted as the downwash at the surface of the airfoil without too much error, provided the thickness remains small, and will be, for a pitching and translating airfoil,

$$w(\xi, t) = \mp[\dot{h} + V\alpha + (\xi - 2bx_0)\dot{\alpha}] + VY'(\xi) \begin{cases} \text{upper surface} \\ \text{lower surface} \end{cases} \quad (4)$$

where $Y(\xi)$ is the equation which describes the airfoil contour as illustrated in Fig. 1. Using Eq. (4) for the downwash, the velocity potential, Eq. (3), can be expanded in powers of a frequency parameter. This expression is used to get the pressure coefficients, using nonlinear Eq. (2) and retaining only terms which are linear in displacement. The pressure on the lower surface can then be subtracted from the pressure on the upper surface and thickness terms retained.

Such a procedure obviously will not yield the complete nonlinear solution. However, as will be shown subsequently, this method does give the major portion of the thickness effects. The primary advantage of this technique is that frequency effects are readily obtained. While Van Dyke's method is currently available only to cube of frequency, the nonlinear pressure approach can be used to obtain an arbitrary number of frequency terms without prohibitive labor; while cubic frequency terms will prove adequate for a large number of flutter problems, other cases, especially in the lower supersonic region, will occur where more frequency terms are needed.

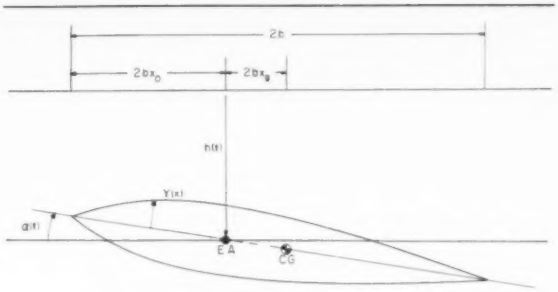


FIG. 1. A two-dimensional wing section.

### *Piston Theory*

Piston theory as an aerodynamic tool has been discussed in reference 10 by Ashley and Zartarian. The basic assumption of piston theory is that the local pressure on an airfoil is related to the local fluid velocity normal to the free stream in the same manner that the pressure on a piston in a one-dimensional channel is related to the velocity of the piston. For this assumption to be valid, Mach Number must be much greater than 1.0. Pressures are time dependent only through the boundary conditions—that is, through the normal fluid velocities at the airfoil surface. Pressures at a point are assumed independent of the conditions at any other point. In the actual case when $M^2 \gg 1.0$, since the component of fluid velocity along the $x$ axis changes very little and is much greater than the speed of sound, disturbances cause practically no change in the $x$ component of velocity from one point to another.

The piston theory third-order expansion for the pressure at a point, as given in references 9 and 10, is

$$p - p_0 = \rho a^2 \left\{ (w/a) + [(\gamma + 1)/4](w/a)^2 + [(\gamma + 1)/12](w/a)^3 \right\} \quad (5)$$

where $w$ is the local downwash, given by Eq. (4) for a pitching and translating airfoil. Lighthill, in reference 9, points out that Eq. (5) can be used with good accuracy provided $M^2 \gg 1$ and $w/a < 1$. Since the downwash $w$ must be less than the sound speed, $a$, a limitation is placed on amplitude of oscillation and airfoil thickness. Since in flutter small perturbations are considered, this is primarily a limit on the airfoil thickness. This also implies that piston theory will not be applicable near the leading edge of blunt-nosed airfoils where the surface slopes are large, or for large angles of attack.

For use in flutter work, the third term in the pressure expansion has usually been found to be negligible and is dropped. Also, only terms which are linear in the dis-

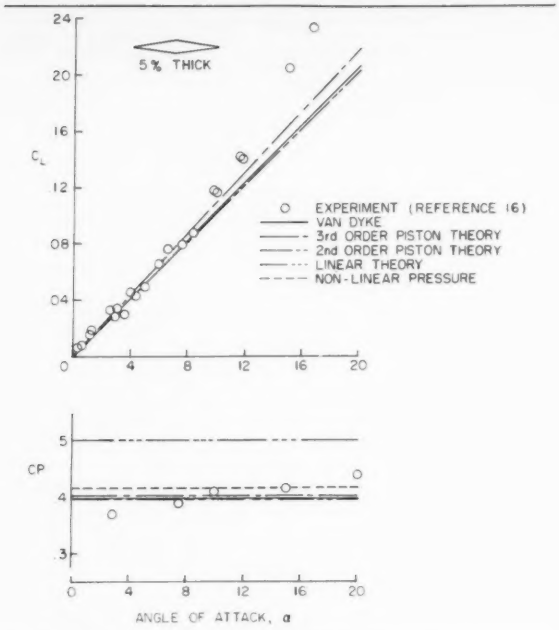


FIG. 2. Experimental and theoretical lift and center of pressure in steady flow at $M = 6.86$.

placements are retained in computing the oscillatory forces so that, as used, piston theory is nonlinear in thickness but linear in displacement. Initial angle of attack effects can be studied provided the third term in the pressure expansion is retained, subject to the limitation that $w/a < 1.0$.

It must be emphasized that piston theory is more than an approximation of linear theory. This method is a legitimate high supersonic theory which agrees with the second-order theory of Van Dyke and is even more valuable due to its simplicity.

Landahl has presented a high Mach Number theory[11] which may be described as an inverse Rayleigh-Janzen method—that is, as an expansion in inverse powers of $M$. An iteration procedure is used, similar to Van Dyke's, and the solution is obtained as an expansion in powers of $1/M$ and thickness. An interesting result obtained by Landahl is that second-order piston theory, which had been based on one-dimensional ideas, can be obtained from the more general potential flow equation to second order and for large $M$.

*Tangent-Wedge Approximation*—The tangent-wedge approximation, discussed by Lees in reference 12, has been used with success to predict pressures for steady hypersonic flow. A basic assumption is that the shock wave is very close to the surface but not coincident with it. The pressure at any point on the surface is taken as being the same as the pressure on a semi-infinite wedge at the same flight Mach Number whose half angle is the local inclination of the surface. The derivation, as carried out by Lees, uses the oblique shock relations with assumptions of large Mach Number and small wedge angles.

It would be of interest to examine some applications of this method to unsteady flow. The local surface inclination becomes time dependent, making the pressures a function of time. The resulting expression for the local pressure can be expanded as a power series in the downwash velocity and, to third order, is

$$p - p_0 = \rho a^2 \left\{ (w/a) + [(\gamma + 1)/4] (w/a)^2 + [(\gamma + 1)^2/32] (w/a)^3 \right\} \quad (6)$$

where $w/a < 1.0$.

Eq. (6) is identical with the piston theory relation for the pressure at a point, Eq. (5), up to and including terms of order $(w/a)^2$. The deviation between the expressions is only 10 per cent in the coefficient of the $(w/a)^3$ term. As previously mentioned, in flutter calculations only terms to order $(w/a)^2$ would seem to be ordinarily required and the tangent-wedge approach would be identical with piston theory.

It is of interest that a similar approximation for three-dimensional slender bodies is possible, referred to as the tangent-cone approximation by Lees in reference 12. An application to a cone-shaped body will be given subsequently.

***Newtonian Approximation***

The Newtonian approximation may be used to predict pressures on an airfoil or body of revolution. In this representation for hypersonic flow, the fluid particles ahead of the body are undisturbed. Upon striking the surface, these particles lose their momentum normal to the surface, then flow tangentially with no further change in velocity. This concept implies that the shock wave coincides with the body surface while the flow is compressed into an infinitesimal layer, sometimes called the hypersonic boundary layer, between the surface and the shock. This does not account for the change in the effective shape of the body which can be caused by thick boundary layers and viscous effects. The pressure relation is derived in reference 14 for a two-dimensional profile and is given by

$$C_p = 2[f'^2 + ff''] \quad (7)$$

This pressure is determined by the local change in fluid momentum, given by the first term in Eq. (7), with a correction added to account for the centrifugal force required to make the fluid follow the surface contour, the second term of Eq. (7).

The function $f$ which appears in Eq. (7) describes the surface of the airfoil and varies with time as well as position. For a pitching and translating airfoil, this function is

$$f = \mp [h(t) + (x - cx_0)\,\alpha(t)] + Y(x) \begin{cases} \text{upper surface} \\ \text{lower surface} \end{cases} \quad (8)$$

The instantaneous slope of this surface, $f'$, multiplied by free-stream velocity, corresponds to the downwash velocity $w$ appearing in Eqs. (5) and (6).

Any point of the surface in shadow, hidden from the free stream by a portion of the airfoil, is assumed to

be in a region of near zero pressure. As reference 12 points out, viscous effects would probably increase the pressure due to boundary-layer breakaway.

Forces and moments determined from Eq. (7) will be independent of Mach Number. Reference 12 points out that this is characteristic of the Newtonian approximation and is true in fact for slender bodies at $M > 10$ and at lower Mach Numbers for blunt bodies. The tangent-wedge and piston theory methods also become essentially independent of $M$ for $M \gg 1$, as can be seen by rewriting Eq. (6) as

$$C_p = 2[1 - 1/M)(w/V) + [(\gamma + 1)/4](w/V)^2 + M[(\gamma + 1)^2/32](w/V)^3] \quad (9)$$

and noting that the first term vanishes as $M$ becomes large.

An expression similar to Eq. (7) can be determined for bodies of revolution (reference 14) which allows the Newtonian approximation to be applied to three-dimensional bodies.

## Application of High Mach Number Theories

### *Comparison With Experiment at Zero Frequency*

With several methods such as those just discussed available for use in flutter calculations, the question of which is best naturally arises. Some steady-state measurements of lift and moment have been reported and can serve as a limited basis for comparison.

In reference 15, McLellan, Bertram, and Moore have reported the lift and center of pressure as measured on some 5 per cent thick airfoil sections at $M = 6.86$. Their results for a double-wedge airfoil are shown in Fig. 2 as a function of angle of attack and compared with predicted lift and center of pressure by the various methods.

The predicted lift coefficients are in good agreement with experiment by all methods up to angles of attack of about 10°. The predicted lift is identical by the linear, Van Dyke, and nonlinear-pressure methods, while Landahl's technique is identical with second-order piston theory. The best agreement with experiment actually results when third-order piston theory is used.

The results of using a nonlinear thickness theory become more apparent when the center of pressure or the moment is examined. As Fig. 2 shows, linear two-dimensional theory predicts that the center of pressure will be at the 50 per cent chord. All the thickness theories show that the center of pressure will be shifted forward about 10 per cent of the chord from the linear theory prediction. The experiment shows much better agreement with the nonlinear theories, even to large angles of attack. This would indicate that these nonlinear methods should give more accurate moments, even at angle of attack, and accurate moment prediction is well known to be of vital importance in aeroelastic calculations such as flutter.

Van Dyke[7] presents a limited amount of experimental data at $M = 1.42$ and 1.61 on an oscillating biconvex airfoil which was obtained at the National Physical Laboratory, Teddington, England. These data show a marked improvement, even at such low Mach Numbers, of the Van Dyke nonlinear theory over the linear theory.

### *Comparison of Theories Through Flutter Calculations*

The various aerodynamic theories may be compared by their prediction of flutter. For this purpose, a simple two degree of freedom system similar to Fig. 1 was used with a 6 per cent biconvex airfoil. Flutter calculations were made over the Mach Number range 1.3 to 10 for the elastic axis at 40 per cent chord, the center of gravity at 50 per cent chord, and a bending-to-torsion frequency ratio 0.5. The results are presented in Fig. 3 by use of a parameter found convenient in comparing flutter results, $(b\omega_\alpha/a)\sqrt{\mu}$, which is called the stiffness-altitude parameter.

The stiffness-altitude parameter depends only upon the physical properties of the wing—in particular, the torsional stiffness—and upon the atmosphere in which it operates. Its value increases as either altitude or stiffness increase. When plotted as the ordinate against Mach Number, as in Fig. 3, constant dynamic pressure curves will appear as radial lines through the origin. The stable region, when this parameter is the ordinate, will be above the flutter boundary.

The most prominent feature of Fig. 3 is the divergence between the flutter boundaries as predicted by the linear and the nonlinear theories at the higher Mach Numbers. For example, at Mach Number 6, the non-

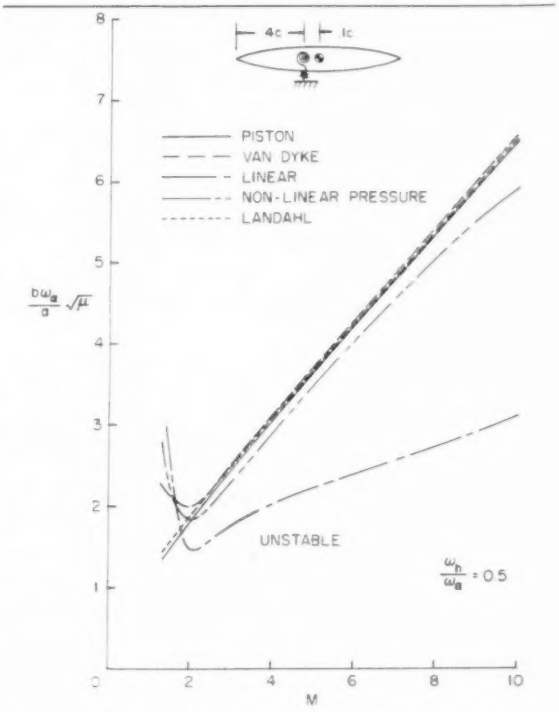


FIG. 3. Flutter boundaries for a 6 per cent biconvex airfoil, $\mu = 250$, $r_\alpha^2 = 0.25$.

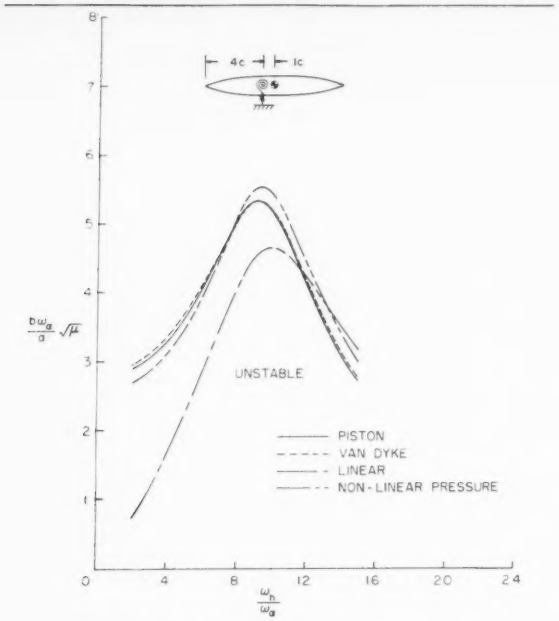


FIG. 4. Flutter boundary variation with frequency ratio for a biconvex airfoil, $M = 5$, $\tau = 0.06$, $\mu = 250$, $r_\alpha^2 = 0.25$.

linear theories require about 80 per cent more stiffness than linear theory in order to avoid flutter at a given altitude.

For Mach Numbers greater than 2 or 3, flutter calculations by Van Dyke's method (including terms to the cube of frequency), Landahl's method (using three terms), and piston theory give essentially the same result. The flutter boundary by the Landahl method falls between the other two. In the lower supersonic Mach Number range, the results of both piston theory and Landahl's method deviate considerably from the Van Dyke boundary. However, the Landahl method has been shown to give better agreement with Van Dyke down to $M \simeq 1.5$ if more terms are used in the expansion.[11] The nonlinear-pressure results, using terms through the seventh power of frequency, fall very close to the Van Dyke result to $M \simeq 8$, indicating that most of the nonlinearity due to thickness is contained in the method.

An interesting point is the crossover of the flutter boundaries near $M = 1.5$ as predicted by linear theory and the nonlinear theories. Below this Mach Number, the effect of thickness is stabilizing. At higher Mach Numbers, thickness is increasingly destabilizing.

In reference 16, for example, it is pointed out that the thickness effect varied drastically with frequency ratio when piston theory was used for the flutter calculation. The other nonlinear aerodynamic theories predict this same variation as shown in Fig. 4 where stiffness-altitude parameter is plotted against frequency ratio at $M = 5$ for the same parameters used in Fig. 3. At this Mach Number, Van Dyke and piston theory give almost identical curves. The nonlinear pressure method agrees essentially with them also. The thickness effect is destabilizing at frequency ratios less than about 1.0 and stabilizing for higher frequency ratios.

Flutter as calculated by the Van Dyke, Landahl, and piston-theory methods shows agreement for $M \geqq 2.0$ to 3.0. At lower supersonic Mach Numbers, the latter two methods are not expected to give reliable answers. In this range, $1.0 < M \leqq 2.0$ to 3.0, Van Dyke's nonlinear thickness theory is probably the appropriate procedure to use, provided cubic frequency terms are sufficient. The nonlinear-pressure method contains most of the nonlinearity but still does not give quite as good agreement with the more exact Van Dyke method for $M \geqq 2.0$ to 3.0 as the much simpler theories. In the lower Mach Number region, it shows better agreement with Van Dyke.

In the high Mach Number range, $M \geqq 2.0$ to 3.0, piston theory flutter calculations show very good agreement with calculations made with the more exact theory. They show better agreement than calculations made by the nonlinear-pressure method. In view of its simplicity and in conjunction with its agreement with more exact methods, piston theory will now be used to show calculated flutter trends at high Mach Numbers.

### *Flutter Trends at High Mach Number*

The nonlinear thickness theories just discussed have been shown to predict changes in flutter boundaries at high Mach Numbers when compared to linear theory. The parameters used in Figs. 3 and 4 were deliberately chosen to emphasize the large variations which are possible. With a change of parameters, the thickness effects may be much less or the trends may be altered. With the aid of piston theory, these changes due to thickness may be examined. At the high Mach Numbers being considered, first-order or zero-thickness piston theory will predict the same flutter speed as linear theory and will be used for comparison.

*Frequency Ratio*—Examples of the magnitude of the thickness effects for various parameters, as well as the change in trends with frequency ratio which may be expected, are shown in Fig. 5. A stiffness parameter is given at $\mu = 150$ for a zero thickness plate and for 3 and 6 per cent biconvex airfoils. Fig. 5(a) is for the same set of parameters used in Figs. 3 and 4, elastic axis at 40 per cent chord and center of gravity at 50 per cent chord. At very low frequency ratios, zero thickness theory shows no flutter while airfoils with thickness have a finite flutter speed. However, above frequency ratios of about 1.2, thickness becomes stabilizing.

Fig. 5(b) is for a 50 per cent elastic axis with a 60 per cent center of gravity. In this case, the zero thickness wing has a finite flutter speed at low frequency ratios. The effect of thickness is large, changing from destabilizing at low frequency ratios to stabilizing for $\omega_h/\omega_\alpha \gtrsim 1.1$. Fig. 5(c) shows a case where thickness is destabilizing for all frequency ratios. The parameters here place the elastic axis at 40 per cent and center of

gravity at 60 per cent chord. Finally, Fig. 5(d) gives an instance with very little thickness effect at low frequency ratios. This is an aft elastic axis configuration, at 60 per cent chord, with the center of gravity at 80 per cent chord. The crossover with frequency ratio is again apparent with a large stabilizing effect at ratios greater than 1.0.

*Center of Gravity and Elastic Axis*—Fig. 5 has shown that thickness effects on flutter speed may have large variations which depend on the elastic axis and center of gravity locations of the system. Examples of the variation with these parameters are shown in Figs. 6 and 7 at $M = 5$ for a bending-to-torsion frequency ratio of 0.5. In both Figures, the stiffness-altitude parameter for a 3 per cent thick biconvex airfoil is compared with that of a zero thickness flat plate. In Fig. 6, which is plotted against axis position, a thickness of only 3 per cent is seen to require that the elastic axis be placed about 5 per cent farther forward to avoid flutter with a fixed amount of static unbalance. Fig. 7 gives the flutter boundary variation with center of gravity position for various elastic axis locations. For

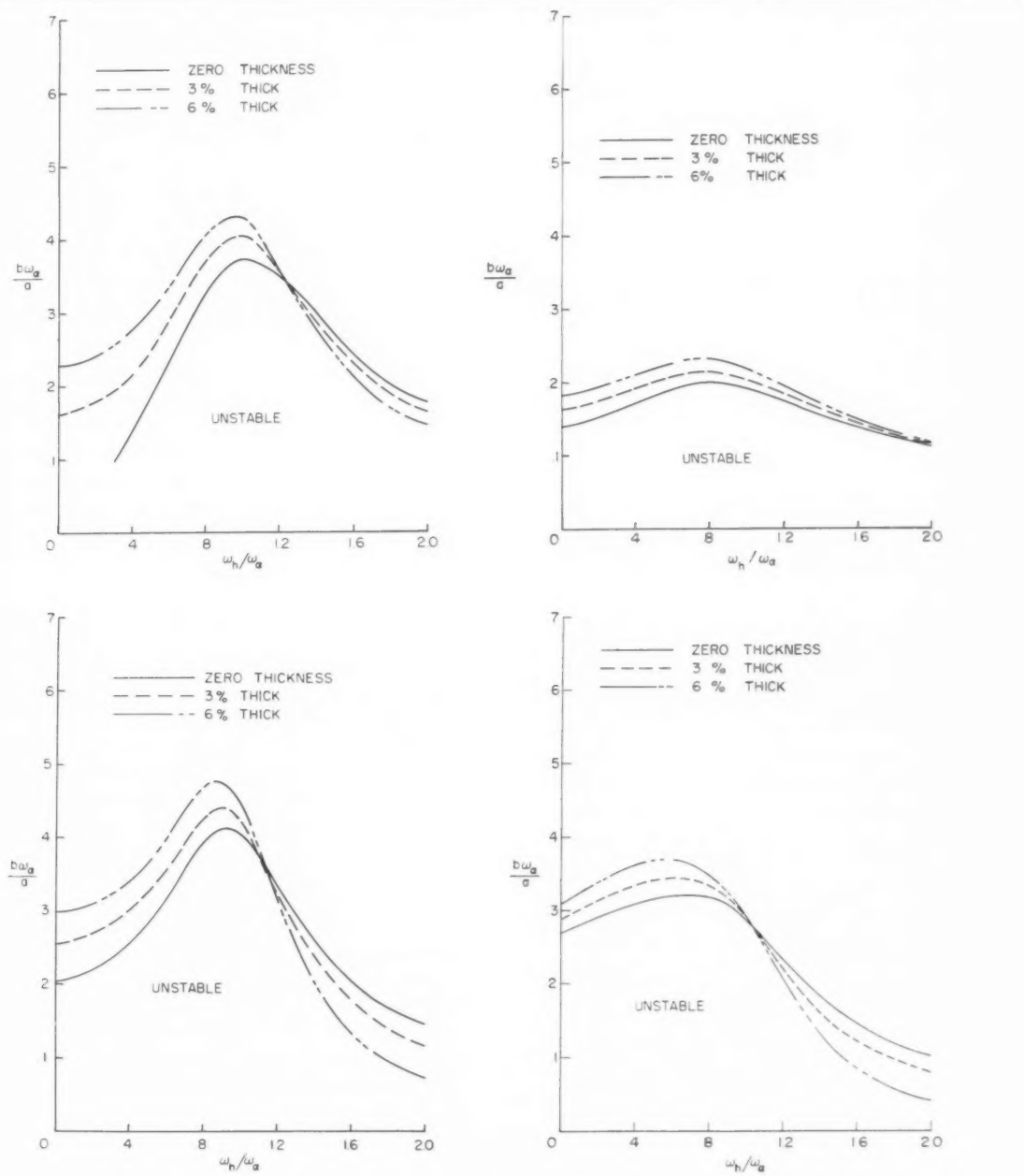


FIG. 5. Flutter boundaries showing thickness effect on biconvex airfoils, $\mu = 150$, $r_\alpha^2 = 0.25$. (a) *Top left.* $M = 5$, $x_g = 0.1$, $x_0 = 0.4$. (b) *Bottom left.* $M = 5$, $x_g = 0.1$, $x_0 = 0.5$. (c) *Top right.* $M = 3$, $x_g = 0.2$, $x_0 = 0.4$. (d) *Bottom right.* $M = 4$, $x_g = 0.2$, $x_0 = 0.6$.

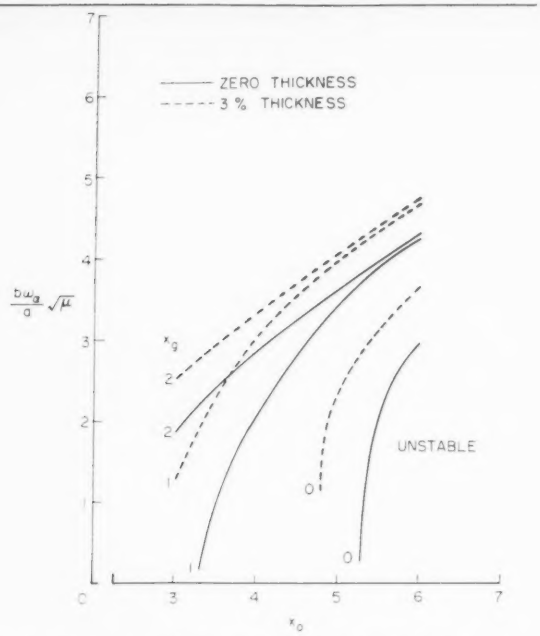


FIG. 6. Flutter boundary variation with elastic axis location for a biconvex airfoil, $M = 5$, $\mu = 250$, $r_\alpha^2 = 0.25$, $\omega_h/\omega_\alpha = 0.5$.

a given axis location, thickness requires the center of gravity be farther forward to avoid flutter. That is, more mass balance will be required by thickness. This Figure also shows that, for a fixed elastic axis, there is a center of gravity location which gives a minimum flutter speed. The two Figures show that, generally, the effect of thickness is to increase the region of instability.

*Airfoil Shape*—The previous examples illustrating effects which may result from thickness were for a biconvex airfoil. The airfoil shape itself may influence the flutter boundaries, as shown in Fig. 8. Here a stiffness parameter is given for three 4 per cent thick airfoil sections and a zero thickness plate. The 65A and double-wedge airfoils, when compared to the zero thickness plate, present curves similar to the biconvex airfoils. A large reduction in flutter speed is apparent at low frequency ratios with a crossover near $\omega_h/\omega_\alpha = 1.2$. The shape effect is stabilizing at higher frequency ratios. The wedge presents a different picture—the result of its shape is destabilizing at all frequency ratios. However, the magnitude of this flutter speed reduction is small over the entire range. Generally, a blunt trailing edge has been found to decrease the size of the thickness effect on an airfoil.

### *Possible Refinements*

At extremely high Mach Numbers, aerodynamic forces are altered by effects such as strong shock waves, viscosity, dissociation, ionization, etc. The previously discussed methods do not account for such features in the flow. However, piston theory presents some interesting possibilities for use at these Mach Numbers, several of which will now be discussed.

*Local Flow*—In the original work of Hayes, in which he reasoned from the assumptions of slender bodies and large Mach Numbers, piston theory was based on free-stream conditions. In the physical picture as used by Lighthill, each point on the airfoil is regarded as a small piston moving in a one-dimensional channel. The pressure on this piston is determined by its own motion and by the speed of sound and density at its face which are free stream in the usual applications. This pressure is independent of the pressure at any other point. Thus, each tiny "piston" on an airfoil surface will feel only the local conditions and will not be influenced by free stream. Since Mach Number, density, and velocity all vary locally, the pressure distribution could be altered and change the total force and moment.

Forces and moments as determined using the local flow conditions with piston theory have been used in a flutter calculation for a 4 per cent thick double-wedge airfoil. Local Mach Number, density, and velocity were calculated by the standard shock-wave relations. The results are plotted in Fig. 9 as the stiffness-altitude parameter versus flight Mach Number and compared with standard piston theory calculations. The local flow effect is stabilizing and is generally small.

The local flow conditions used with piston theory also present possibilities for studying angle of attack effects.

*Blunt-Nosed Airfoils*—Lighthill has pointed out that for the piston theory expansion in powers of $w/a$ to give the pressure at a point, $w/a$ must be less than 1.0, where $w$ is the downwash velocity at the surface of the airfoil, given by Eq. (4), and $a$ is the free-stream sound speed. If the theory is limited to small displacements, the downwash from Eq. (4) will be approximately

$$w \simeq VY'(x) \tag{10}$$

Therefore, $$w/a = MY'(x) < 1.0 \tag{11}$$

is the requirement for piston theory validity. This shows that pressures will be inaccurate in regions where the airfoil slope is large.

Airfoils with blunt leading edges are of great practical significance due to heating requirements. Over these leading edges, the slope of the contour is very large and the piston theory requirement of Eq. (11) is not met. The Newtonian approximation, however, can be used to obtain pressures in this region of the airfoil, while piston theory can be used over the remainder of the surface. The effect of the detached shock wave should also be included for a more complete picture but has not been attempted in this discussion.

This technique has been applied to a blunt-nosed airfoil whose surface is parabolic over the leading 20 per cent and biconvex over the remainder of the chord. The airfoil contour is described by the equation

$$\left.\begin{aligned} Y(x) &= 0.84\,\tau c\sqrt{x/c}, && 0 \leqq x \leqq 0.2c \\ &= \tau c\,[0.117 + 1.64\,(x/c) - 1.76\,(x/c)^2], && 0.2c \leqq x \leqq c \end{aligned}\right\} \tag{12}$$

Over the leading edge, the slope of this contour will be

$$Y'(x) = 0.42\ \tau\sqrt{c/x}$$

The piston theory requirement of Eq. (11) will be satisfied if

$$M\,Y'(x) = (0.42/\sqrt{x})\ (M\tau)\ \sqrt{c} < 1.0$$

or

$$\sqrt{x} > 0.42\ (M\tau)\ \sqrt{c} \qquad (13)$$

The airfoil selected for the calculation was 3 per cent thick. Over the forward 5 per cent of the airfoil, Newtonian theory, as given by Eq. (7) without the centrifugal force correction, was applied. Piston theory was used on the remainder of the surface. The maximum slope occurring with the piston theory will be at $x = 0.05c$, so that the piston theory aerodynamics should be valid for $M \leqq 17.7$.

The results of this calculation are shown in Fig. 10 and compared with a conventional piston theory calculation. For the frequency ratios below 1.0, revising the leading-edge pressures according to Newtonian theory is seen to have a minor stabilizing influence over a wide Mach Number range. When the frequency ratio is greater than 1.0, very little effect is seen at the lower Mach Numbers, but for $M \gtrsim 15$, a destabilizing influence is seen at $\omega_h/\omega_\alpha = 1.2$, while a highly stabilizing effect appears at a frequency ratio of 1.5.

An interesting secondary result appears in Fig. 10. For the higher frequency ratios, $\omega_h/\omega_\alpha = 1.2$ and 1.5, the curves have a maximum at $M \simeq 10$–$15$. These maximums would be design points similar to the transonic maximums determining the stiffness required to avoid flutter at a given altitude for this configuration.

### *Flutter of a Cone*

There are certain instances when a cone may be installed on aircraft—for instance, as an angle of attack indicator. The question arises as to the flutter possibilities of this configuration at high speeds.

In deriving the air forces for such a study, a steady-state theory due to von Kármán[12] was used in a manner similar to the tangent-wedge or tangent-cone approximation. A philosophy similar to that of piston theory was followed in the use of the instantaneous downwash. The pressure coefficient as given by von Kármán is

$$C_p = (2/M^2)K_c^2 \log (2/K_c) \qquad (14)$$

where $K_c = w/a$ and $K_c$ is required to be less than 1.0. Performing a Taylor expansion about $K_c = 1$, insertion of the appropriate boundary conditions for a rotating and plunging cone, linearization with regard to the displacements, and integration over the cone result in the following expressions for the oscillating lift and moment on the cone:

$$\bar{L}_1 = 0, \quad \bar{L}_2 = \pi\Delta/8Mk,$$

$$\bar{L}_3 = \pi\Delta/8Mk^2, \quad \bar{L}_4 = (\pi\Delta/6Mk) - 2x_0\,\bar{L}_2,$$

$$\bar{M}_1 = 0, \quad \bar{M}_2 = (\pi\Delta/6Mk) - 2x_0\,\bar{L}_2,$$

$$\bar{M}_3 = (\pi\Delta/6Mk^2) - 2x_0\,\bar{L}_3,$$

$$\bar{M}_4 = (\pi\Delta/4Mk) - 2x_0\,[\bar{M}_2 + \bar{L}_4 + 2x_0\,\bar{L}_2]$$

where

$$\Delta = (1/3) + M\theta \log 2 - (M\theta)^2 + (1/6)\ (M\theta)^3$$

This aerodynamic input has been used in a sample flutter calculation for a 15° conical shell. The requirement for $K_c < 1$ limits the usefulness of these calculations to $M\theta \lesssim 1$ or $M \lesssim 7.65$. The results are shown on Fig. 11, where a stiffness-altitude parameter has been plotted against Mach Number. The flutter region is below the curve. Results are presented for three axes of rotation, $x_0 = 1/3$, $1/2$, and $2/3$, where the critical Mach Number varies from 5 at $x_0 = 1/2$ to 3 at $x_0 = 1/3$. Note that the axis placed at midchord represents the lowest flutter speed. Axis locations ahead of or behind the midchord require less stiffness to avoid flutter or, conversely, could be flown at a lower altitude without flutter.

## Concluding Remarks

Some of the theories for two-dimensional oscillatory air forces for use in flutter calculations at high Mach Numbers have been discussed. These include linear theory, Van Dyke's second-order theory, piston theory, Landahl's method, tangent-wedge and tangent-cone approximations, Newtonian theory, and a method utilizing the nonlinear-pressure coefficient. The methods which include nonlinear thickness terms give much better agreement with experiment at $M = 6.86$ for static lift and center of pressure. The methods including nonlinear thickness terms have also been shown to predict flutter speeds which may be very different from the prediction of linear theory.

The second-order solution of Van Dyke is based on the general potential flow equations. This method

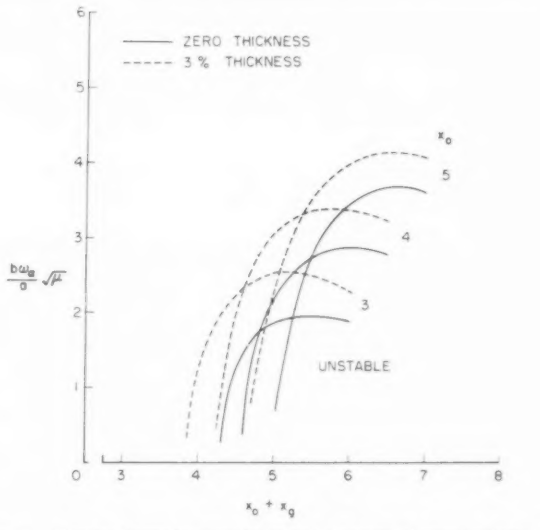


FIG. 7. Flutter boundary variation with center of gravity location for a biconvex airfoil, $M = 5$, $\mu = 250$, $r_\alpha^2 = 0.25$, $\omega_h/\omega_\alpha = 0.5$

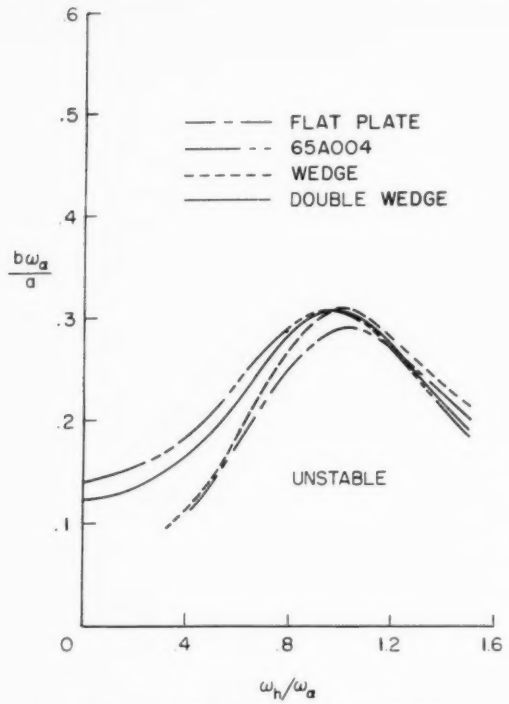


FIG. 8. Effect of airfoil shape on flutter speed of 4 per cent thick airfoils, $M = 5$, $\mu = 250$, $r_\alpha^2 = 0.25$, $x_g = 0.1$, $x_0 = 0.4$.

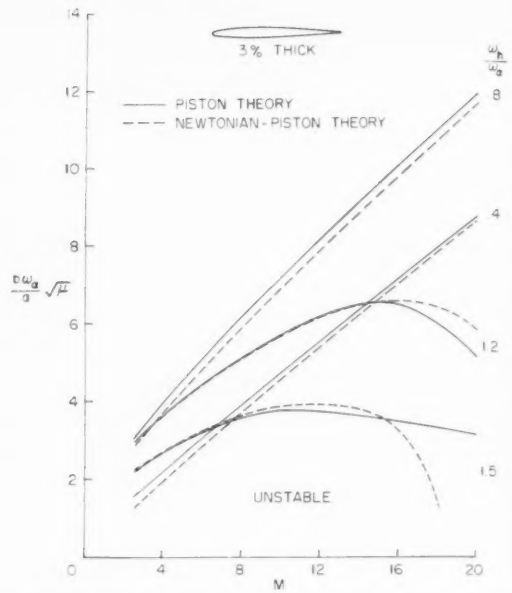


FIG. 10. Flutter boundaries using Newtonian piston theory, $\mu = 250$, $r_\alpha^2 = 0.25$, $x_g = 0.1$, $x_0 = 0.4$.

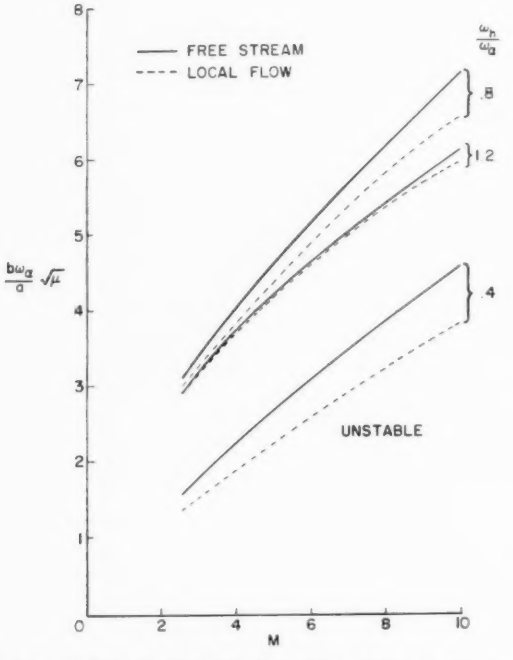


FIG. 9. Effect of using local flow conditions on flutter speed of a 4 per cent double wedge, $\mu = 250$, $r_\alpha^2 = 0.25$, $x_g = 0.1$, $x_0 = 0.4$.

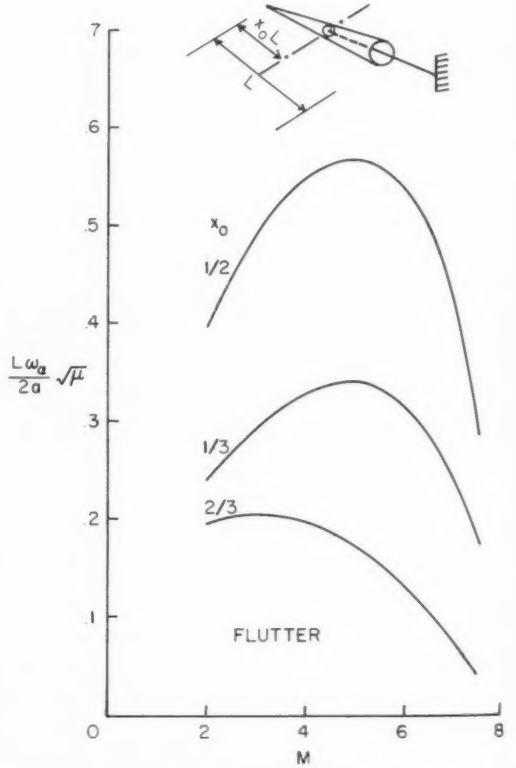


FIG. 11. Effect of axis location on the flutter of a cone, $\tilde{\mu} = 3.0$, $\omega_h/\omega_\alpha = 0.5$, $r_\alpha^2 = (1 - 2x_0)^2 + [(7/5) - 2x_0]$, $x_g = (3/4) - x_0$.

corresponds to linear theory as Busemann's second-order solution corresponds to Ackeret's linearized solution for the steady case. As currently available, the method is limited in the lower supersonic region ($M \lesssim 2.0$) by having only terms to cube of frequency.

For Mach Number greater than 2.0 or 2.5, piston theory may be used in flutter calculations. It has been shown to agree with calculations by the more exact method of Van Dyke at these higher Mach Numbers. Landahl's method gives slightly better agreement than piston theory with Van Dyke when used in flutter calculations. Agreement of piston theory with the tangent-wedge approximation shows that this simple method should also be valuable in the hypersonic region. Newtonian theory has possible applications at hypersonic speeds and around blunt airfoils.

The nonlinear pressure method has been presented as an easy way to obtain an effect of thickness with a large number of frequency terms. A second possible use for this method is in conjunction with linear three-dimensional theory to obtain an effect of thickness together with aspect ratio.

The simplified flutter calculations presented have shown that thickness effects on flutter speed may or may not be important. Depending on the parameters of the system, such as frequency ratio, elastic axis location, center of gravity, etc., the thickness effect may be stabilizing, negligible, or destabilizing; the shape of the airfoil has been shown to influence these results.

Some possible refinements on piston theory for use at extremely high speeds were discussed. In general, the effect on calculated flutter speeds was small. In the absence of available experimental data, their value cannot be assessed.

The possibility of flutter of a cone at hypersonic speeds was shown by using the tangent-cone approximation for aerodynamic forces. The critical location for the elastic axis was discussed together with the existence of a critical Mach Number for flutter.

The thickness effects discussed here have been shown to be capable of producing sizable changes in flutter speed. Studies of aspect ratio when combined with thickness are now needed. Information is also needed on such nonlinear effects as boundary layer, viscosity, shock waves, etc., since intelligent design for flutter demands an accurate knowledge of the aerodynamics involved.

## References


[1] Garrick, I. E., and Rubinow, S. I., *Flutter and Oscillating Air-Force Calculations for an Airfoil in a Two-Dimensional Supersonic Flow*, NACA Report 846, 1946.

[2] Watkins, C. E., *Effect of Aspect Ratio on the Air Forces and Moments of Harmonically Oscillating Thin Rectangular Wings in Supersonic Potential Flow*, NACA Report 1028, 1951.

[3] Nelson, H. C., *Lift and Moment on Oscillating Triangular and Related Wings With Supersonic Edges*, NACA TN 2494, 1951.

[4] Pines, S., and Dugundji, J., *Aerodynamic Flutter Derivatives of a Flexible Wing With Supersonic Edges*, AIA Report ARTC-7 February, 1954.

[5] Carrier, G. F., *The Oscillating Wedge in a Supersonic Stream*, Journal of the Aeronautical Sciences, Vol. 16, No. 3, pp. 150–152, March, 1949.

[6] Jones, W. P., and Skan, Sylvia W., *Aerodynamic Forces on Biconvex Aerofoils Oscillating in a Supersonic Airstream*, R&M No. 2749, British ARC, 1951.

[7] Van Dyke, Milton D., *Supersonic Flow Past Oscillating Airfoils Including Nonlinear Thickness Effects*, NACA Report 1183, 1954.

[8] Hayes, W., *On Hypersonic Similitude*, Quarterly of Applied Mathematics, Vol. V, No. 1, pp. 105–106, April, 1947.

[9] Lighthill, M. J., *Oscillating Airfoils at High Mach Number*, Journal of the Aeronautical Sciences, Vol. 20, No. 6, pp. 402–406, June, 1953.

[10] Ashley, H., and Zartarian, G., *Piston Theory—A New Aerodynamic Tool for the Aeroelastician*, Journal of the Aeronautical Sciences, Vol. 23, No. 12, pp. 1109–1118, December, 1956.

[11] Landahl, Marten T., *Unsteady Flow Around Thin Wings at High Mach Numbers*, Journal of the Aeronautical Sciences, Vol. 24, No. 1, pp. 33–38, January, 1957.

[12] Lees, Lester, *Hypersonic Flow*, Presented at the Fifth International Aeronautical Conference, June, 1955.

[13] Leslie, D. C. M., *An Introduction to Second-Order Wing Theory*, Journal of the Aeronautical Sciences, Vol. 24, No. 2, pp. 99–106, February, 1957.

[14] Ivey, H. R., Klunker, E. B., and Bowen, E. N., *A Method for Determining the Aerodynamic Characteristics of Two- and Three-Dimensional Shapes at Hypersonic Speeds*, NACA TN 1613, 1948.

[15] McLellan, Charles H., Bertram, Mitchel H., and Moore, John A., *An Investigation of Four Wings of Square Plan Form at a Mach Number of 6.9 in the Langley 11-Inch Hypersonic Tunnel*, NACA Report 1310, 1957 (supersedes NACA RM L51D17).

[16] Garrick, I. E., *Aerodynamic Theory and Its Application to Flutter*, AGARD Report 34, April, 1956.



## IAS Twenty-Seventh Annual Meeting

*Hotel Sheraton-Astor, New York City, January 26–29, 1959*

The scope of the meeting will be broad to cover the many fields of interest to IAS members. The meetings committee plans to schedule papers on aerodynamics, hypersonics, aeroelasticity, missiles and rockets, missile propulsion, space propulsion, satellites and spacecraft, space medicine, VTOL/STOL aircraft, rotary wing aircraft, meteorology, etc.

Members or organizations wishing to have papers considered for presentation at this meeting should submit outlines or short abstracts to the Meetings Committee, 2 East 64th St., New York 21, N.Y., no later than August 1, 1958.

# Compressive Buckling of a Long Simply Supported Plate on an Elastic Foundation

PAUL SEIDE*

*The Ramo-Wooldridge Corporation*

SUMMARY

A solution is obtained for the problem of the compressive buckling of infinitely long, flat, simply supported plates resting on an elastic foundation. The effect of nonattachment of the plate and foundation is found to reduce drastically the buckling load of the plate as compared to a plate with attached foundation.

SYMBOLS

$A, B$ = constants appearing in deflection functions
$b$ = width of plate
$c$ = fraction of half-buckle wavelength representing length of region of plate in which the foundation is compressed
$D$ = flexural stiffness of plate $[D = Et^3/12(1 - \nu^2)]$
$E$ = Young's modulus of plate material
$F(x)$ = function representing variation in $x$-direction of the plate deflection
$k$ = buckling load coefficient $(k = b^2N/\pi^2D)$
$\bar{k}$ = foundation modulus
$N$ = critical compressive load per inch of plate width
$t$ = plate thickness
$w$ = plate deflection
$x$ = distance along plate longitudinal axis [see Fig. 1(b)]
$y$ = distance along width of plate
$\gamma$ = foundation modulus parameter $(\gamma = b^4\bar{k}/\pi^4D)$
$\nabla^4$ = $(\partial^4/\partial x^4) + 2(\partial^4/\partial x^2\partial y^2) + (\partial^4/\partial y^4)$
$\lambda$ = half-wavelength of buckle
$\nu$ = Poisson's ratio

*Subscripts*

1 refers to portion of plate which compresses foundation
2 refers to portion of plate which pulls away from foundation

## INTRODUCTION

A CONSIDERABLE LITERATURE exists concerning the behavior of plates on elastic foundations. In most or all of these investigations, however, the plate is assumed to be attached in some way to the foundation and is found to be considerably strengthened thereby.

The problem investigated in the present paper is that of the effect of nonattachment of the foundation on the compressive buckling load of a long plate, simply supported along its longitudinal edges. The analysis presented here indicates, as might be expected, that the unattached foundation raises the plate buckling load only a relatively small amount as compared to that of the plate with attached foundation, for which the buckling load is limited only by the inelastic properties of the material.

Received January 17, 1958.

* Member of the Technical Staff, Engineering Mechanics Department, Space Technology Laboratories.

The author wishes to express his appreciation to Dr. Eugene Levin and Dr. Kenneth Hoffman of the Computer Systems Division for their help in making the stability criteria amenable to computation and for supervising the performance of the complex calculations involved in the solution of the problem.

## ANALYSIS

We consider an infinitely long flat plate, simply supported at its long edges, and compressed in the longitudinal direction. The plate rests on, but is not attached to, a foundation of the Winkler type—that is, the deflection at any point is proportional only to the load applied at that point [see Fig. 1(a)]. Since the plate is infinitely long, it can be expected to buckle in some repetitive pattern so that one part of the pattern compresses the foundation while the remaining portion separates from the foundation [Fig. 1(b)]. The deflections of the former are governed by the differential equation

$$D\nabla_1{}^4w_1 + N(\partial^2w_1/\partial x_1{}^2) + kw_1 = 0, \qquad -c\lambda \le x_1 \le c\lambda \quad (1)$$

and of the latter by

$$D\nabla_2{}^4w_2 + N(\partial^2w_2/\partial x_2{}^2) = 0, \qquad -(1 - c)\lambda \le x_2 \le (1 - c)\lambda \quad (2)$$

The deflections of the two regions are connected by the boundary conditions

$$\left.\begin{aligned} w_1\big|_{x_1 = c\lambda} &= w_2\big|_{x_2 = -(1-c)\lambda} = 0 \\ \left.\frac{\partial w_1}{\partial x_1}\right|_{x_1 = c\lambda} &= \left.\frac{\partial w_2}{\partial x_2}\right|_{x_2 = -(1-c)\lambda} \\ \left.\frac{\partial^2 w_1}{\partial x_1{}^2}\right|_{x_1 = c\lambda} &= \left.\frac{\partial^2 w_2}{\partial x_2{}^2}\right|_{x_2 = -(1-c)\lambda} \\ \left.\frac{\partial^3 w_1}{\partial x_1{}^3}\right|_{x_1 = c\lambda} &= \left.\frac{\partial^3 w_2}{\partial x_2{}^3}\right|_{x_2 = -(1-c)\lambda} \end{aligned}\right\} \quad (3)$$

implying zero deflection at the boundaries of the two regions (by definition of the extent of the two regions) and continuity of slope, moment, and shear. In addition, the deflections of each region are symmetrical about $x_1 = 0$ and $x_2 = 0$, respectively.

We assume deflection functions of the form

$$\left.\begin{aligned} w_1 &= F_1(x_1)\cos(\pi y/b) \\ w_2 &= F_2(x_2)\cos(\pi y/b) \end{aligned}\right\} \quad (4)$$

Substitution of these functions into Eqs. (1) and (2) and use of the assumed symmetry conditions yields

$$F_1(x_1) = A_1 \cosh \alpha_1(x_1/b) \cos \alpha_2(x_1/b) + B_1 \sinh \alpha_1(x_1/b) \sin (\alpha_2 x_2/b)$$
$$F_2(x_2) = A_2 \cos \beta_1(x_2/b) + B_2 \cos \beta_2(x_2/b) \quad (5a)$$

$$\text{where } \alpha_{1,2} = (\pi/2)\sqrt{2(\sqrt{1+\gamma}) \mp (k-2)}$$
$$\beta_{1,2} = (\pi/2)(\sqrt{k} \mp \sqrt{k-4}) \quad (5b)$$
$$\gamma = b^4 k/\pi^4 D, \quad k = b^2 N/\pi^2 D$$

Substitution of Eqs. (5a) into the boundary conditions (3) yields

$$A_1 \cosh \alpha_1 c(\lambda/b) \cos \alpha_2 c(\lambda/b) + B_1 \sinh \alpha_1 c(\lambda/b) \sin \alpha_2 c(\lambda/b) = 0 \quad (6a)$$

$$A_2 \cos \beta_1(1-c)(\lambda/b) + B_2 \cos \beta_2(1-c)(\lambda/b) = 0 \quad (6b)$$

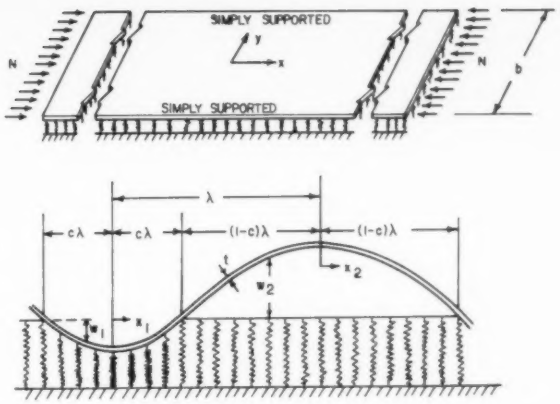


FIG. 1. Notation for problem discussed. (a) *Top.* Compressed plate resting on elastic foundation. (b) *Bottom.* Assumed repeating buckling pattern.

$$A_1[\alpha_1 \sinh \alpha_1 c(\lambda/b) \cos \alpha_2 c(\lambda/b) - \alpha_2 \cosh \alpha_1 c(\lambda/b) \sin \alpha_2 c(\lambda/b)] + B_1[\alpha_1 \cosh \alpha_1 c(\lambda b) \sin \alpha_2 c(\lambda/b) + \alpha_2 \sinh \alpha_1 c(\lambda/b) \cos \alpha_2 c(\lambda/b)] = A_2\beta_1 \sin \beta_1(1-c)(\lambda/b) + B_2\beta_2 \sin \beta_2(1-c)(\lambda/b) \quad (6c)$$

$$A_1[(\alpha_1^2 - \alpha_2^2) \cosh \alpha_1 c(\lambda/b) \cos \alpha_2 c(\lambda/b) - 2\alpha_1\alpha_2 \sinh \alpha_1 c(\lambda/b) \sin \alpha_2 c(\lambda/b)] + B_1[(\alpha_1^2 - \alpha_2^2) \sinh \alpha_1 c(\lambda/b) \sin \alpha_2 c(\lambda/b) + 2\alpha_1\alpha_2 \cosh \alpha_1 c(\lambda/b) \cos \alpha_2 c(\lambda/b)] = -A_2\beta_1^2 \cos \beta_1(1-c)(\lambda/b) - B_2\beta_2^2 \cos \beta_2(1-c)(\lambda/b) \quad (6d)$$

$$A_1[\alpha_1(\alpha_1^2 - 3\alpha_2^2) \sinh \alpha_1 c(\lambda/b) \cos \alpha_2 c(\lambda/b) + \alpha_2(\alpha_2^2 - 3\alpha_1^2) \cosh \alpha_1 c(\lambda/b) \sin \alpha_2 c(\lambda/b)] + B_1[\alpha_1(\alpha_1^2 - 3\alpha_2^2) \cosh \alpha_1 c(\lambda/b) \sin \alpha_2 c(\lambda/b) - \alpha_2(\alpha_2^2 - 3\alpha_1^2) \sinh \alpha_1 c(\lambda/b) \cos \alpha_2 c(\lambda/b)] = -A_2\beta_1^3 \sin \beta_1(1-c)(\lambda/b) - B_2\beta_2^3 \sin \beta_2(1-c)(\lambda/b) \quad (6e)$$

Eqs. (6a) and (6b) yield relationships between $A_1$ and $B_1$, and $A_2$ and $B_2$, respectively The remaining three equations yield three relationships between $B_1$ and $B_2$ which must be identical. These, then, are the stability criteria

$$\frac{[\sinh 2\alpha_1 c(\lambda/b)/2\alpha_1] + [\sin 2\alpha_2 c(\lambda/b)/2\alpha_2]}{\beta_1 \tan \beta_1(1-c)(\lambda/b) - \beta_2 \tan \beta_2(1-c)(\lambda/b)} = \frac{\cosh 2\alpha_1 c(\lambda/b) + \cos 2\alpha_2 c(\lambda/b)}{\beta_2^2 - \beta_1^2} = \frac{(\alpha_2^2 - 3\alpha_1^2)[\sinh 2\alpha_1 c(\lambda/b)/2\alpha_1] - (\alpha_1^2 - 3\alpha_2^2)[\sin 2\alpha_2 c(\lambda/b)/2\alpha_2]}{\beta_1^3 \tan \beta_1(1-c)(\lambda/b) - \beta_2^3 \tan \beta_2 \tan \beta_2(1-c)(\lambda/b)} \quad (7)$$

which are two simultaneous equations for $k$ and $c$ as a function of $\gamma$ and $\lambda/b$.

Eqs. (7) can be arranged in a form that is better for computation by expressing them first as follows:

$$\beta_1 \tan \beta_1(1-c)\frac{\lambda}{b} - \beta_2 \tan \beta_2(1-c)\frac{\lambda}{b} = (\beta_2^2 - \beta_1^2)\frac{[\sinh 2\alpha_1 c(\lambda/b)/2\alpha_1] + [\sin 2\alpha_2 c(\lambda/b)/2\alpha_2]}{\cosh 2\alpha_1 c(\lambda/b) + \cos 2\alpha_2 c(\lambda/b)} \quad (8a)$$

$$\beta_1^3 \tan \beta_1(1-c)\frac{\lambda}{b} - \beta_2^3 \tan \beta_2(1-c)\frac{\lambda}{b} = (\beta_2^2 - \beta_1^2)\frac{(\alpha_2^2 - 3\alpha_1^2)[\sinh 2\alpha_1 c(\lambda/b)/2\alpha_1] - (\alpha_1^2 - 3\alpha_2^2)[\sin 2\alpha_2 c(\lambda/b)/2\alpha_2]}{\cosh 2\alpha_1 c(\lambda/b) + \cos 2\alpha_2 c(\lambda/b)} \quad (8b)$$

We next solve Eqs. (8) for $\tan \beta_1(1-c)(\lambda/b)$ and $\tan \beta_2(1-c)(\lambda/b)$ to obtain

$$\tan \beta_1(1-c)\frac{\lambda}{b} = \frac{(\beta_2^2 - \alpha_2^2 + 3\alpha_1^2)[\sinh 2\alpha_1 c(\lambda/b)/2\alpha_1] + (\beta_2^2 + \alpha_1^2 - 3\alpha_2^2)[\sin 2\alpha_2 c(\lambda/b)/2\alpha_2]}{\beta_1[\cosh 2\alpha_1 c(\lambda/b) + \cos 2\alpha_2 c(\lambda/b)]} \quad (9a)$$

$$\tan \beta_2(1-c)\frac{\lambda}{b} = \frac{(\beta_1^2 - \alpha_2^2 + 3\alpha_1^2)[\sinh 2\alpha_1 c(\lambda/b)/2\alpha_1] + (\beta_1^2 + \alpha_1^2 - 3\alpha_2^2)[\sin 2\alpha_2 c(\lambda/b)/2\alpha_2]}{\beta_2[\cosh 2\alpha_1 c(\lambda/b) + \cos 2\alpha_2 c(\lambda/b)]} \quad (9b)$$

Then
$$\tan \beta_2(1-c)(\lambda/b) = \tan\{(\beta_2/\beta_1)\tan^{-1}[\tan \beta_1(1-c)(\lambda/b)]\} \quad (10a)$$

or
$$\tan\left\{\frac{\beta_2}{\beta_1}\tan^{-1}\frac{(\beta_2^2 - \alpha_2^2 + 3\alpha_1^2)[\sinh 2\alpha_1 c(\lambda/b)/2\alpha_1] + (\beta_2^2 + \alpha_1^2 - 3\alpha_2^2)[\sin 2\alpha_2 c(\lambda/b)/2\alpha_2]}{\beta_1[\cosh 2\alpha_1 c(\lambda/b) + \cos 2\alpha_2 c(\lambda/b)]}\right\} - = 0 \quad (10b)$$

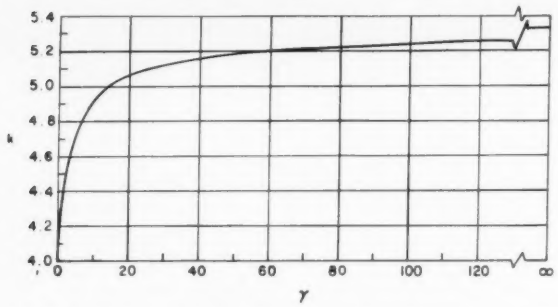


FIG. 2(a). Variation of buckling load coefficient with foundation modulus parameter.

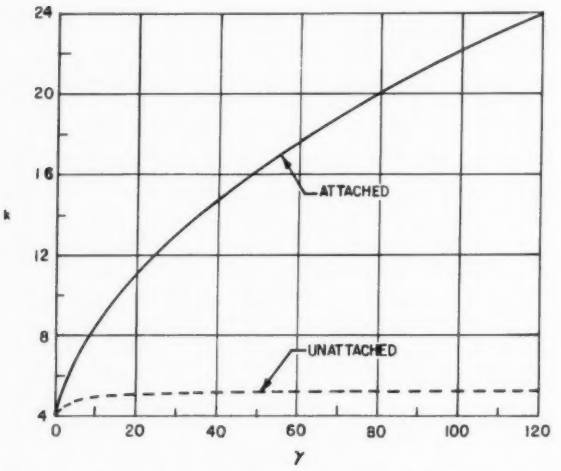


FIG. 2(b). Comparison of buckling loads of plates attached and not attached to the foundation.

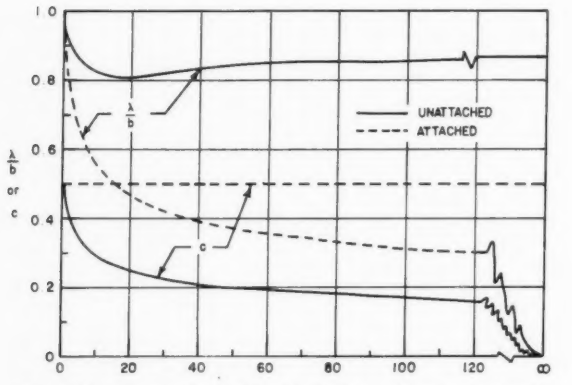


FIG. 2(c). Comparison of buckle half-wavelengths and region proportions for plates attached and not attached to the foundation.

FIG. 3. Limiting buckle configuration for plate resting on a rigid foundation.

TABLE 1

| $\gamma$ | $k$ | $\lambda/b$ | $c$ |
|---|---|---|---|
| 0 | 4.00 | 1.00 | 0.50 |
| 1 | 4.33 | 0.94 | 0.44 |
| 3 | 4.62 | 0.88 | 0.38 |
| 5 | 4.75 | 0.85 | 0.34 |
| 10 | 4.92 | 0.85 | 0.29 |
| 20 | 5.07 | 0.82 | 0.26 |
| 30 | 5.12 | 0.81 | 0.22 |
| 40 | 5.16 | 0.82 | 0.21 |
| 50 | 5.19 | 0.82(5) | 0.20 |
| 60 | 5.20 | 0.84 | 0.19 |
| 70 | 5.21 | 0.83(5) | 0.18(5) |
| 80 | 5.22 | 0.84 | 0.18 |
| 90 | 5.23 | 0.83(5) | 0.17(5) |
| 100 | 5.24 | 0.84 | 0.17 |
| 1,000 | 5.31 | 0.84 | 0.095 |

which is the desired stability criterion of one equation for $k$ as a function of $\gamma$ and $(\lambda/b)c$. In the solution of this equation for a given value of $\gamma$, a value of $c(\lambda/b)$ was chosen and $k$ was varied until Eq. (10b) was satisfied. This process was repeated for other values of $c(\lambda/b)$ until a minimum value of $k$ was obtained. This value of $k$ is then the buckling load and, if the corresponding values of $c(\lambda/b)$ and $(1 - c)(\lambda/b)$ [obtained from Eq. (9a)] are denoted by $x$ and $y$, respectively,

$$c = x/(x + y), \quad \lambda/b = x + y \tag{11}$$

In the performance of the calculations, there was some question as to where the quadrant in which the angle represented by the inverse tangent in Eq. (10b) lay. A criterion was introduced to aid in determining the quadrant—namely, that the deflection functions represented by Eqs. (5a) and (5b) must not change sign within the regions in which they are valid—a change of sign would mean that the region in which the plate was assumed to pull away from the foundation would contain a region in which the plate compressed the foundation, and, similarly, the region in which the plate was assumed to compress the foundation would contain a region in which the plate pulled away from the foundation. The numerical calculations indicate that, subject to this criterion, the angle represented by the inverse tangent lies in the first quadrant near the critical values of $(\lambda/b)c$ and $k$.

## NUMERICAL RESULTS AND DISCUSSION

The calculated results of the investigation are presented in Table 1.

The values of $\lambda/b$ and $c$ are, by the nature of the computation procedure, less accurate than the values of $k$. These results are shown graphically in Figs. 2(a), 2(b), and 2(c), where the results for a long plate attached to the foundation are also given. These are

$$\left.\begin{aligned} k &= 2[1 + \sqrt{1 + \gamma}] \\ \lambda/b &= 1/\sqrt[4]{1 + \gamma} \\ c &= 0.5 \end{aligned}\right\} \tag{12}$$

It will be noted from Table 1 that the values of $k$ seem to be approaching some asymptotic value. The limit of $k$ as $\gamma$ becomes infinite can readily be deter-

(Continued on page 394)

# A Simple Method of Matric Structural Analysis: Part III—Analysis of Flexible Frames and Stiffened Cylindrical Shells

BERTRAM KLEIN*

*Convair Astronautics, A Division of General Dynamics Corporation*

SUMMARY

The method presented in Part II (reference 2) is extended to cover the case of stiffened cylinders. Treatable loadings include those producing peak shear, such as in flexible frame problems, and those involving thermal stresses. Various structural irregularities may be accounted for, such as variable frame moment of inertia, tapered longerons, variable skin gage, cutouts, noncircular cylindrical shells, etc. A flexible frame problem is solved for illustration purposes.

SYMBOLS

$A$ = cross-sectional area
$A, B$ = parameters
$a$ = frame spacing
$E$ = Young's modulus
$F, \bar{s}, f$ = functions of $\varphi$ or factor
$G$ = shear modulus
$I$ = effective centroidal moment of inertia of frame cross-section
$\int$ = integral
$L$ = developed length of outer line of curved element
$M$ = frame bending moment
$P$ = axial force or applied load
$q$ = shear flow or shear flow coefficient
$R$ = frame radial force
$r$ = radius
$S$ = stiffness
$T$ = frame tangential force
$t$ = skin gage
$u, v$ = tangential and radial displacements
$V$ = frame shear
$w$ = axial displacement
$x$ = axial coordinate
$y$ = coordinate
$\alpha$ = thermal coefficient of expansion or function of $\varphi$
$\beta$ = angle subtended by curved element
$\gamma$ = parameter
$\Delta$ = determinant or difference
$\delta$ = parameter
$\epsilon$ = strain or error function
$\theta$ = angular rotation
$\varphi$ = angle
$\kappa, \lambda$ = parameters
$\mu$ = parameter
$\rho$ = parameter
$\sigma$ = axial stress
$\tau$ = temperature
$\psi$ = angular coordinate

***Superscripts and Subscripts***

$\bar{}, *$ = effective
$'$ = modified
$0, 1, 2, \ldots$ = numerical indices
$c$ = centroidal
$H$ = horizontal
$i, j, n$ = numerical indices
$M$ = relating to bending moment
$mm, rr$, etc. = denoting various stiffnesses
$o$ = outer
$R, r$ = radial
$T, t$ = tangential
$V$ = vertical
$\Delta\tau$ = due to temperature difference

Presented at the Missile Structures Session, Twenty-Sixth Annual Meeting, IAS, New York, January 27–30, 1958.

* Head, Structures Theory and Methods Group.

## INTRODUCTION

IN PARTS I AND II (see references 1 and 2), for the structures considered, it has been assumed that the shear flow is constant along each nontapered shear panel—i.e., this element takes shear only. This assumption is simple and convenient but not always realistic. In flexible frame problems, for example, it is known that the shear flow can vary radically circumferentially.[4] Therefore, in the present paper a method is developed in which the shear flow is allowed to vary along each curved element. The variation is assumed to be in the form of a power series in the angle subtended by the curved element. However, any other convenient series could be used, such as a Fourier series.

The structures considered here contain, in general, curved segmental elements (which may be of nonuniform cross section), curved panel elements, and longeron elements (which may be tapered). The curved panel elements are assumed to carry axial as well as shear load as a consequence of the variable shear flow assumption. The axial load carrying thickness is designated

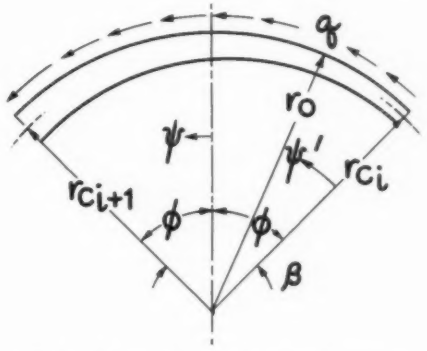


FIG. 1. Curved segmental element geometry.

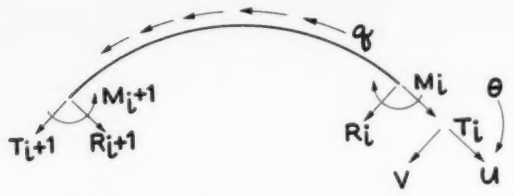


FIG. 2. Curved segmental element loading.

$l$; the shear carrying thickness is designated $t$. Both thicknesses may vary within the element. The radius of curvature, $r_o$, is assumed to be constant within each curved element but may vary from element to element. The dimension, $r_c$, however, may vary within each curved element.

Loadings which may be considered include concentrated loads either in the plane of the frames or in the axial direction, various distributed loadings in the axial direction, and thermal loadings of the frames and longerons. It is assumed, however, that there are no hoop stresses between frames and that the longerons cannot take bending or torsion.

## (1) Curved Segmental Element

### (a) *Shear Flow*

Refer to Fig. 1. Positive shear flow acting on the curved segmental element and the origin for the angular coordinate, $\psi$, are taken as shown. The shear flow is expressed as

$$q = q_0 + q_1(\psi/\varphi) + q_2(\psi/\varphi)^2 + q_3(\psi/\varphi)^3 \ldots \quad (1)$$

The actual shear flow acting at certain points defined by $\psi_1, \psi_2, \psi_3, \ldots, \psi_n$ may be expressed in terms of the coefficients, $q_0, q_1, q_2, q_3, \ldots$, as

$$\begin{bmatrix} q_{\psi_1} \\ q_{\psi_2} \\ q_{\psi_3} \\ \cdot \\ \cdot \\ \cdot \\ q_{\psi_n} \end{bmatrix} = \begin{bmatrix} 1 & (\psi_1/\varphi) & (\psi_1/\varphi)^2 & (\psi_1/\varphi)^3 \\ 1 & (\psi_2/\varphi) & (\psi_2/\varphi)^2 & (\psi_2/\varphi)^3 \\ 1 & (\psi_3/\varphi) & (\psi_3/\varphi)^2 & (\psi_3/\varphi)^3 \ldots \\ & & \ldots & \\ 1 & (\psi_n/\varphi) & (\psi_n/\varphi)^2 & (\psi_n/\varphi)^3 \end{bmatrix} \begin{bmatrix} q_0 \\ q_1 \\ q_2 \\ q_3 \\ \cdot \\ \cdot \\ \cdot \end{bmatrix} \quad (1a)$$

### (b) *Equilibrium Equations*

Refer to Fig. 2. The three equations of equilibrium of a curved segmental element are expressed in terms of the forces shown as

$$\left.\begin{aligned} \text{vertical:}\quad & (T_i + T_{i+1})f_1 + (R_i + R_{i+1}) + (F_{V1}q_1 + F_{V3}q_3 + \ldots)r_o = 0 \\ \text{horizontal:}\quad & (T_i - T_{i+1})f_1^{-1} + (-R_i + R_{i+1}) - (2q_0 + F_{H2}q_2 + F_{H4}q_4 + \ldots)r_o = 0 \\ \text{moment:}\quad & (r_{c_i}T_i - r_{c_{i+1}}T_{i+1}) + (M_i - M_{i+1}) - [\beta q_0 + (\beta/3)q_2 + (\beta/5)q_4 + \ldots]r_o^2 = 0 \end{aligned}\right\} \quad (2)$$

The quantities, $f$ and $F$ are certain functions of $\varphi$. These functions are defined in the Appendix and listed in Table 1.

### (c) *Force-Displacement Equations—Constant Section*

The three force-displacement equations for a curved segmental element with constant cross-sectional properties are

$$\left.\begin{aligned} & -(M_i + M_{i+1}) + (\theta_i - \theta_{i+1})S_{mm} + (v_i + v_{i+1})S_{mr} + (u_i - u_{i+1})S_{mt} - (F_{M1}q_1 + F_{M3}q_3 + \ldots)r_o^2 = 0 \\ & -(R_i - R_{i+1}) + (\theta_i + \theta_{i+1})S_{rm} + (v_i - v_{i+1})S_{rr} + (u_i + u_{i+1})S_{rt} - (F_{R0}q_0 + F_{R2}q_2 + F_{R4}q_4 + \ldots)r_o = 0 \\ & -(T_i + T_{i+1}) + (\theta_i - \theta_{i+1})S_{tm} + (v_i + v_{i+1})S_{tr} + (u_i - u_{i+1})S_{tt} - (F_{T1}q_1 + F_{T3}q_3 + \ldots)r_o = 0 \end{aligned}\right\} \quad (3)$$

The functions, $F_M$, $F_R$, and $F_T$ are defined in the Appendix. Certain numerical values are listed in Table 1. The positive sign convention for $u$, $v$, and $\theta$ is shown in Fig. 2. The stiffnesses, $S$, are the same as those defined by Eq. (9) of reference 2. The equations are repeated here in the Appendix, and numerical values of $S$ are listed in Table 2.

### (d) *Force-Displacement Equations—Variable Section*

When the cross-sectional properties of the curved segmental element vary, it is convenient to write the force-displacement equations in the following form (see the Appendix for the derivation):

$$\left.\begin{aligned} & -(\theta_i - \theta_{i+1}) + I_{M_1}M_i + I_{T_1}T_i + I_{R_1}R_i - [(I_{q_0})_1q_0 + (I_{q_1})_1q_1 + (I_{q_2})_1q_2 + \ldots] + (I_{\Delta T})_1 = 0 \\ & -(u_{i+1} - r_{c_{i+1}}\theta_{i+1})\sin\beta - (v_i - v_{i+1}\cos\beta) + I_{M_2}M_i + I_{T_2}T_i + I_{R_2}R_i - [(I_{q_0})_2q_0 + (I_{q_1})_2q_1 + (I_{q_2})_2q_2 + \ldots] + (I_{\Delta T})_2 = 0 \\ & v_{i+1}\sin\beta - (u_i - u_{i+1}\cos\beta) + (r_{c_i}\theta_i - r_{c_{i+1}}\theta_{i+1}\cos\beta) - I_{M_3}M_i - I_{T_3}T_i - I_{R_3}R_i + [(I_{q_0})_3q_0 + (I_{q_1})_3q_1 + (I_{q_2})_3q_2 + \ldots] + (I_{\Delta T})_3 = 0 \end{aligned}\right\} \quad (4)$$

The integrals appearing in Eq. (4) are

$$I_{M_1} = \int_0^\beta (r_c/\overline{EI})d\psi'; \quad I_{T_1} = r_{c_i}I_{M_1} - \int_0^\beta (r_c^2\cos\psi'/\overline{EI})d\psi'$$

$$I_{R_1} = \int_0^\beta (r_c^2\sin\psi'/\overline{EI})d\psi' = I_{M_2}; \quad I_{T_2} = r_{c_i}I_{M_2} - \int_0^\beta (\lambda r_c^3\sin 2\psi'/2\overline{EI})d\psi'$$

TABLE 1(a)
Functions of $\varphi$

| $\varphi$ degrees | $f_1$ | $f_2$ | $f_3$ | $F_{V1}$ | $F_{V3}$ | $F_{H2}$ | $F_{H4}$ |
|---|---|---|---|---|---|---|---|
| 5 | .0874886635 | .1744442770 | .0000886481854 | .00509247011 | .0030550387 | .6659892477 | .3994193832 |
| 10 | .1763269807 | .3483557383 | .0007010120982 | .02055836177 | .01232785029 | .6639510768 | .3976728021 |
| 15 | .2679491924 | .5211969245 | .002401851092 | .04698104669 | .01281517152 | .6605342759 | .3947439565 |
| 20 | .3639702342 | .6924210399 | .005710660893 | .0853958291 | .05111793289 | .6557085883 | .3906146509 |
| 22.5 | .4142135623 | .7772520933 | .0081460700 5 | .1095723503 | .0655489632 | .6527544039 | .3880869262 |
| 25 | .4663076581 | .8614671619 | .01119746404 | .1373968613 | .0821366104 | .6494306690 | .3852442349 |
| 30 | .5773502691 | 1.027755305 | .01944224539 | .2053155816 | .1225381096 | .6416430456 | .3785887852 |
| 35 | .7002075382 | 1.190681298 | .03104917776 | .2925106698 | .1742378815 | .6322727043 | .3705899918 |
| 40 | .8390996311 | 1.349611422 | .04665197939 | .4038433728 | .2400066603 | .6212292324 | .3611756957 |
| 45 | 1. | 1.503876787 | .0669195390 | .5464790894 | .3239260830 | .6084024258 | .3502580059 |
| 50 | 1.191753592 | 1.652767416 | .0925618358 | .7312980430 | .4321904666 | .5936592365 | .3377308976 |
| 55 | 1.428148006 | 1.795526008 | .1243361683 | .9755219384 | .5745996387 | .5768398938 | .3234671602 |
| 60 | 1.732050807 | 1.931341414 | .1630536876 | 1.307973372 | .7675479626 | .5577529705 | .3073145183 |
| 65 | 2.144506920 | 2.059341825 | .2095862023 | 1.780652174 | 1.040603246 | .5361690886 | .2890906825 |
| 67.5 | 2.414213562 | 2.120120659 | .2360738307 | 2.068496236 | 1.223611481 | .5243567877 | .2791553677 |
| 70 | 2.747477419 | 2.178587769 | .2648731833 | 2.497081726 | 1.452956894 | .5118128411 | .2685770007 |
| 75 | 3.732050807 | 2.288065035 | .3299288427 | 3.702155605 | 2.142777227 | .4843523475 | .2455102513 |
| 80 | 5.671281819 | 2.386677720 | .4058490830 | 6.123512817 | 3.524625863 | .4533856216 | .2195719348 |
| 85 | 11.43005230 | 2.473241717 | .4938180105 | 13.40926486 | 7.671376727 | .4184225881 | .1903741516 |

TABLE 1(b)
Functions of $\varphi$ for $\kappa = \lambda = (r_o/r_c) = 1$

| $\varphi$ degrees | $F_{R0}$ | $F_{R2}$ | $F_{R4}$ | $F_{T1}$ | $F_{T3}$ | $F_{M1}$ | $F_{M3}$ |
|---|---|---|---|---|---|---|---|
| 5 | .0060927398612 | .001160496297 | .0004835024389 | .0747883891 | .04153640232 | .00001266162877 | .0000041817306 86 |
| 10 | .02437643461 | .004642571485 | .001934292589 | .1405079254 | .0830798568 | .0001013661295 | .0000337d373017 |
| 15 | .05486659699 | .01044796431 | .004352751509 | .2240894812 | .1245611212 | .0003425248613 | .0001141298969 |
| 20 | .0975883281 | .01857951206 | .007739683721 | .2984630857 | .1659719425 | .0008132832611 | .0002709033577 |
| 22.5 | .1235474543 | .02351873614 | .00979664396 | .3355497442 | .1866434240 | .001159175998 | .0003860478763 |
| 25 | .1525777094 | .02904104729 | .01209613309 | .3725576426 | .2072832453 | .001591923096 | .0005300575310 |
| 30 | .2198755926 | .04183725953 | .01742337517 | .4463005095 | .2484356047 | .002758198129 | .0009179431588 |
| 35 | .2995308766 | .05697349779 | .02372286340 | .5196170852 | .2895390641 | .004393781659 | .001461455449 |
| 40 | .3915957389 | .0744555134 | .03099615862 | .5924305795 | .3304230143 | .006582653962 | .002188035311 |
| 45 | .4961232122 | .0942891433 | .03924483938 | .6646605615 | .3711110713 | .009411553776 | .003125987040 |
| 50 | .6131634706 | .1164798762 | .04847038927 | .7362244816 | .4115759475 | .01297235005 | .004304399243 |
| 55 | .7427591533 | .1410323366 | .05867405649 | .8070351640 | .4517893159 | .01735267844 | .005753571746 |
| 60 | .8849395143 | .1679497320 | .0698566802 | .8770012645 | .4917216656 | .02265628565 | .007504129330 |
| 65 | 1.039713136 | .1972328612 | .0820184771 | .9460264894 | .5313421477 | .02898364546 | .00958916306 |
| 67.5 | 1.121817268 | .2127609897 | .0834663995 | .9801546751 | .5510253918 | .032564683553 | .01076756986 |
| 70 | 1.207058899 | .2288793562 | .0951587788 | 1.014008969 | .5706184100 | .03644251355 | .01204238006 |
| 75 | 1.386914821 | .2628822318 | .1092757128 | 1.080840584 | .6095164209 | .04514653687 | .01489926240 |
| 80 | 1.579164323 | .2992288877 | .1243658122 | 1.146406233 | .6480002781 | .05521590457 | .01819703597 |
| 85 | 1.783619387 | .3378986217 | .1404235446 | 1.210583054 | .6860320048 | .0667780437 | .02197484977 |

$$I_{R_2} = \int_0^\beta (r_c^3/\overline{EI})\ [(1/2)(\kappa + \lambda)\sin^2\psi' + (1/2)(\kappa - \lambda)\cos^2\psi']d\psi';\quad I_{M_2} = \int_0^\beta (r_c^2\cos\psi'/\overline{EI})d\psi'$$

$$I_{T_2} = r_{c_f} I_{M_2} - \int_0^\beta (r_c^3/\overline{EI})\ [(1/2)(\kappa + \lambda)\cos^2\psi' + (1/2)(\kappa - \lambda)\sin^2\psi']d\psi';$$

$$I_{R_3} = \int_0^\beta (\lambda r_c^3 \sin 2\psi'/2\overline{EI})d\psi' \qquad (4a)$$

where $$\kappa = 1 + (\overline{EI}/r_c^2\overline{EA}) + (\overline{EI}/r_c^2\overline{EA}^*);\quad \lambda = 1 + (\overline{EI}/r_c^2\overline{EA}) - (\overline{EI}/r_c^2\overline{EA}^*) \qquad (4a')$$

(the coordinate $\psi'$ is measured from the end of the curved segmental element as shown in Fig. 1) and

$$(I_{q_n})_1 = r_o\int_0^\beta (r_c^2/\overline{EI})\left\{[{}^nC_0(\mathfrak{F}')_n/\varphi^n] - [{}^nC_1(\mathfrak{F}')_{n-1}/\varphi^{n-1}] + \ldots + (-1)^n(\mathfrak{F}')_0\right\}d\psi' =$$
$$r_o\int_0^\beta (r_c^2/\overline{EI})\sum_{i=0}^{n}[{}^nC_i(-1)^i(\mathfrak{F}')_{n-1}/\varphi^{n-i}]d\psi'$$

$$(I_{q_n})_2 = r_o\int_0^\beta (r_c^3/\overline{EI})\sum_{i=0}^{n}[(-1)^i\,{}^nC_i/\varphi^{n-i}]\left\{[(\mathfrak{F}')_{n-i} - f(\mathfrak{F})_{n-i}(\overline{EI}/r_c^2\overline{EA})]\sin\psi' + \right. \qquad (4b)$$
$$\left.(\mathfrak{F})_{n+1-i}(\overline{EI}/r_c^2\overline{EA}^*)\cos\psi'\right\}d\psi'$$

$$(I_{q_n})_3 = r_o\int_0^\beta (r_c^3/\overline{EI})\sum_{i=0}^{n}[(-1)^i\,{}^nC_i/\varphi^{n-i}]\left\{[(\mathfrak{F}')_{n-i} - f(\mathfrak{F})_{n-i}(\overline{EI}/r_c^2\overline{EA})]\cos\psi' - \right.$$
$$\left.(\mathfrak{F})_{n+1-i}(\overline{EI}/r_c^2\,\overline{EA}^*)\sin\psi'\right\}d\psi'$$

where

$$\begin{aligned}
&(\mathfrak{F})_0 = \sin\psi' && (\mathfrak{F}')_n = (r_o/r_c)\,[(\psi')^{n+1}/(n+1)] - n(\mathfrak{F})_n, \quad n \geqq 1\\
&(\mathfrak{F})_1 = 1 - \cos\psi' && (\mathfrak{F}')_0 = (r_o/r_c)\,(\psi') - (\mathfrak{F})_0\\
&(\mathfrak{F})_2 = (\psi') - (\mathfrak{F})_0\\
&(\mathfrak{F})_3 = (\psi')^2 - 2(\mathfrak{F})_1 && f = (n-i), \quad (n-i) \geqq 1\\
&(\mathfrak{F})_4 = (\psi')^3 - 6(\mathfrak{F})_2 && f = 1, \quad (n-i) = 0\\
&\quad\vdots
\end{aligned} \qquad (4b')$$

TABLE 2
Values of Stiffnesses for Various Values of $\varphi$; $\kappa = \lambda = 1$

| $\varphi$ degrees | $S_{mm}(r_o/EI)$ | $S_{mr}(r_o^2/EI)$ | $S_{mt}(r_c^2/EI)$ | $S_{rm}(r_c^2/EI)$ | $S_{rr}(r_o^3/EI)$ | $S_{tr}(r_o^3/EI)$ | $S_{tt}(r_o^3/EI)$ |
|---|---|---|---|---|---|---|---|
| 5 | 68.7300002 | -1967.826821 | 22492.36348 | -392.5372409 | 4486.721194 | -772837.848 | 8833577.02 |
| 10 | 34.32758669 | -490.5644322 | 2782.129145 | -97.0861092 | 550.602686 | -47724.07817 | 270656.6968 |
| 15 | 22.84346318 | -216.9980171 | 809.847623 | -42.37507983 | 158.1459509 | -9237.68338 | 34475.50372 |
| 20 | 17.08888514 | -121.2505965 | 333.1332760 | -23.22877101 | 63.82052384 | -28397.31112 | 7802.097109 |
| 22.5 | 15.16651023 | - 95.4143640 | 230.3506516 | -18.06346397 | 43.60905971 | -1741.577391 | 4204.539758 |
| 25 | 13.62609504 | - 76.9341306 | 164.9857755 | -14.36959537 | 30.81569671 | -1119.881922 | 2401.594533 |
| 30 | 11.30916661 | -52.86196551 | 91.5596100 | - 9.56024881 | 16.55883668 | - 514.933791 | 891.891490 |
| 35 | 9.64698256 | -38.34823928 | 54.76696149 | -6.663592153 | 9.51659585 | - 262.2006185 | 374.4612907 |
| 40 | 8.39397907 | -28.92934961 | 34.47665633 | -4.786944869 | 5.704858745 | - 143.2701465 | 170.7427119 |
| 45 | 7.413727282 | -22.47291014 | 22.47291014 | -3.505876787 | 3.503876787 | - 82.2461850 | 82.2461850 |
| 50 | 6.624365919 | -17.85581931 | 14.98281140 | -2.589822258 | 2.173118901 | - 48.83322057 | 40.97393737 |
| 55 | 5.973797999 | -14.44089867 | 10.11162611 | -1.917308298 | 1.342583744 | -29.60650726 | 20.73069956 |
| 60 | 5.427239177 | -11.84481898 | 6.838609428 | -1.410040323 | .8140871605 | -18.11171771 | 10.45680221 |
| 65 | 4.960799997 | -9.82575094 | 4.581822911 | -1.019432843 | .4753693419 | -11.03618606 | 5.146230102 |
| 67.5 | 4.751976335 | - 8.98075255 | 3.719949510 | -0.857573284 | .3552184850 | - 8.55922674 | 3.543347803 |
| 70 | 4.557120067 | -8.22502203 | 2.993663196 | -.7139413843 | .2598534129 | - 6.586125002 | 2.397153460 |
| 75 | 4.203678617 | -6.935025796 | 1.858234561 | -.4721448963 | .1265108436 | - 3.746481932 | 1.003866808 |
| 80 | 3.891013654 | -5.880702507 | 1.036926517 | -.2791423903 | .04922033488 | - 1.920695745 | .3386704816 |
| 85 | 3.611896183 | -5.008407277 | .438178859 | -.1243269561 | .01087719923 | - .747006988 | .0653546430 |

and, finally,

$$\left.\begin{aligned}(I_{\Delta\tau})_1 &= \int_0^\beta \left(r_c \int_A E\alpha\Delta\tau y dA/\overline{EI}\right) d\psi' \\ (I_{\Delta\tau})_2 &= \int_0^\beta r_c \left[\left(r_c \int_A E\alpha\Delta\tau y dA/\overline{EI}\right) - \left(\int_A E\alpha\Delta\tau dA/\overline{EA}\right)\right] \sin\psi' d\psi' \\ (I_{\Delta\tau})_3 &= \int_0^\beta r_c \left[-\left(r_c \int_A E\alpha\Delta\tau y dA/\overline{EI}\right) + \left(\int_A E\alpha\Delta\tau dA/\overline{EA}\right)\right] \cos\psi' d\psi'\end{aligned}\right\} \quad (4c)$$

The last three integrals represent the effects of "thermal loading" on the curved segmental element. The cross-sectional coordinate, $y$, is measured from the centroidal axis of the cross section positive when outward away from the center of curvature. The quantities, $\overline{EI}$, $\overline{EA}$, and $\overline{EA}^*$ signify that $E$ may vary with $y$ in the expressions

$$\overline{EI} = \int_A Ey^2 dA; \quad \overline{EA} = \int_A E dA; \quad \overline{EA}^* = \int_A E dA^* \quad (4d)$$

All the above integrals can be evaluated numerically on an automatic digital machine as a subproblem. The results can be stored in the machine in their proper matric location.

## (2) Curved Panel Element

Refer to Fig. 3 for the positive sign convention for the shear flow acting on and the geometry of a curved panel element. Notice that as a consequence of the assumption of no hoop stresses the shear flow is constant in the $x$ direction.

### *(a) Equilibrium Equation*

The equilibrium equation relating shear flow and axial stress acting on the curved edges of a curved panel is

$$-(l_i\sigma_i - l_j\sigma_j) + (a/r_o)(dq/d\psi) = 0 \quad (5)$$

or

$$-\sigma_i + (l_j/l_i)\sigma_j + (2a/l_iL) \times [q_1 + 2(\psi/\varphi)q_2 + 3(\psi/\varphi)^2 q_3 + \dots] = 0 \quad (5')$$

with the aid of Eq. (1).

### *(b) Interelement Continuity Equations*

Consider the juncture of two curved panel elements. At such a juncture, it is specified that the axial stress and its first derivative be continuous. Therefore, the following derivatives must be the same for each element at the juncture:

$$(1/lr_o)(dq/d\psi), \quad (1/lr_o^2)(d^2q/d\psi^2) \quad (6)$$

Evaluation of these derivatives using Eq. (1) yields, at the juncture,

$$\left.\begin{aligned}&(q_1 + 2q_2 + 3q_3 + \dots)_i - \\ &\qquad \rho_1(q_1 - 2q_2 + 3q_3 - \dots)_{i+1} = 0 \\ &(q_2 + 3q_3 + 6q_4 + \dots)_i - \\ &\qquad \rho_2(q_2 - 3q_3 + 6q_4 - \dots)_{i+1} = 0\end{aligned}\right\} \quad (6a)$$

where

$$\rho_1 = (L_i/L_{i+1})(l_i/l_{i+1}); \quad \rho_2 = (L_i/L_{i+1})^2 (l_i/l_{i+1}) \quad (6b)$$

The above conditions are valid whether there is a longeron at the juncture or not. However, when there is no longeron at the juncture, the additional requirement of shear flow equality must be specified—i.e.,

$$(q_1 + q_2 + q_3 + \dots)_i - (q_1 - q_2 + q_3 - \dots)_{i+1} = 0 \quad (7)$$

Notice that in the above equations the index $i$ increases in the same direction as the coordinate $\psi$.

### *(c) Boundary Condition Equations*

In addition to the above interelement equations, certain boundary condition equations must be satisfied as follows: (a) at an axis of symmetry,

$$q = 0 \quad \text{and} \quad d^2q/d\psi^2 = 0 \quad (8a)$$

and (b) at an axis of antisymmetry,

$$dq/d\psi = 0 \quad (8b)$$

These equations may be evaluated at given points by use of Eq. (1).

### *(d) Axial Stress-Displacement Equation—No Longeron*

This equation is (see Appendix)

$$-(w_i - w_j) + l_i\sigma_i \int_0^a \{[1 - (x/a)]/El\}\, dx + l_j\sigma_j \int_0^a (x/a)(1/El)\, dx + \int_0^a (\alpha\Delta\tau/E)\, dx = 0 \quad (9)$$

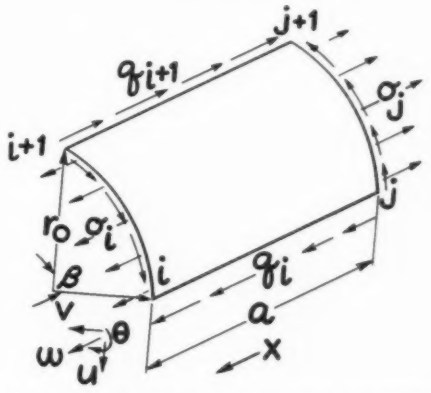


Fig. 3. Curved panel element geometry and loading.

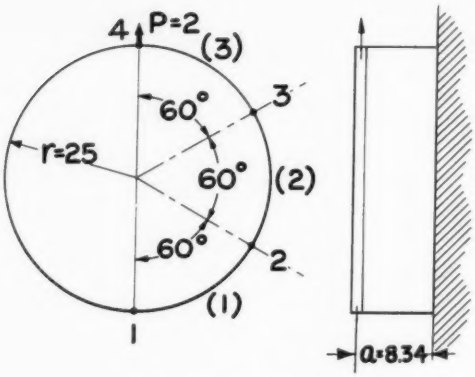


FIG. 5. Cantilever cylinder.

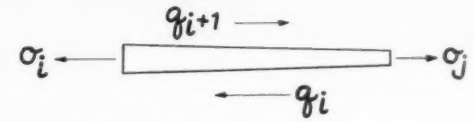


FIG. 4. Longeron element and loading.

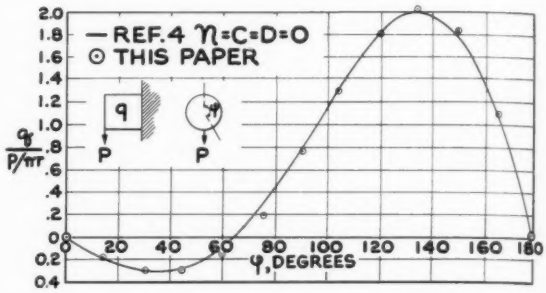


FIG. 7. Shear flow distribution in one field cantilever monocoque for $A = 10^4$, $B = 200$.

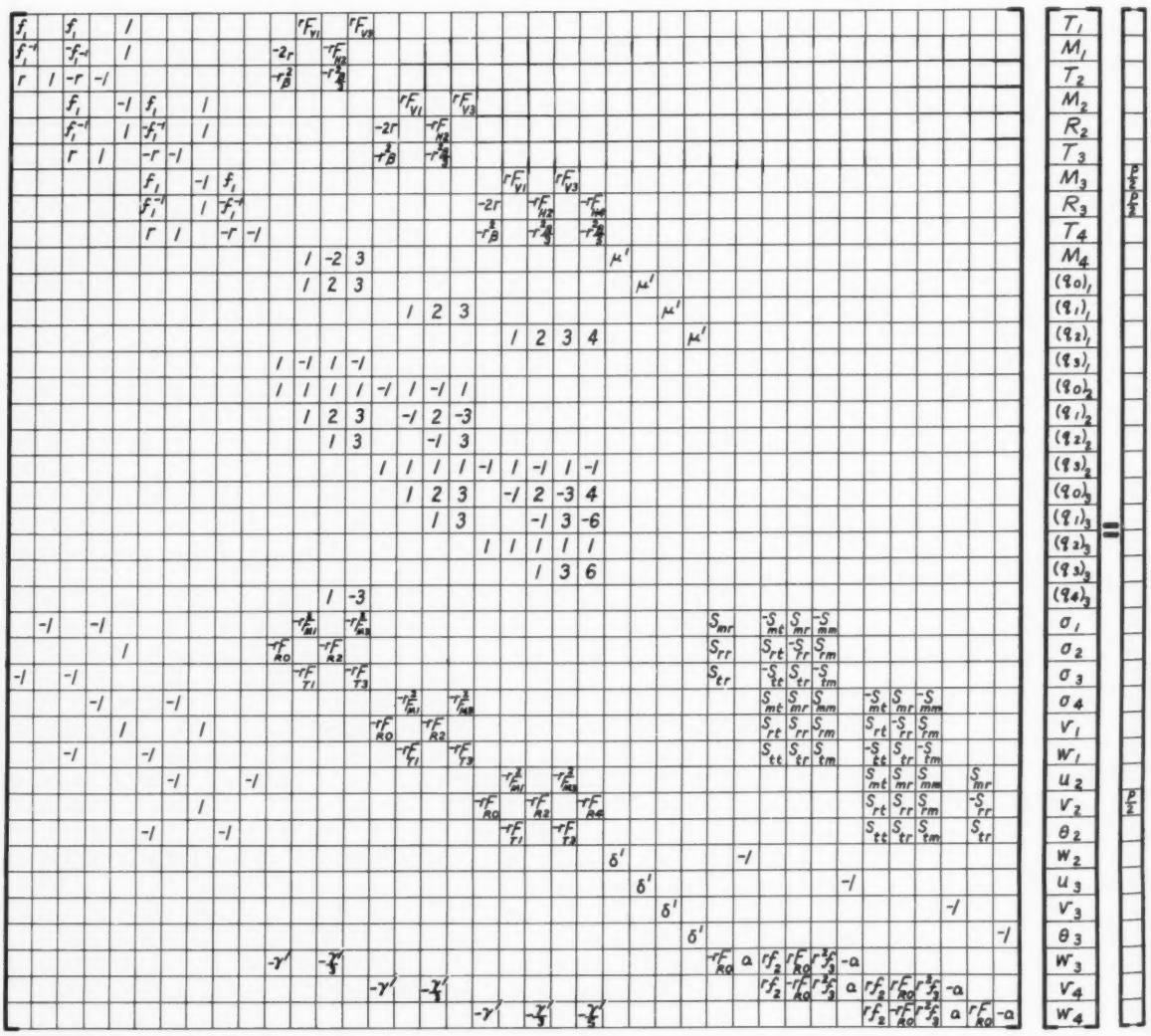

FIG. 6. Matric equation for cantilever cylinder under symmetric radial load.

If $l$ is constant and no temperature gradient is present, the equation is

$$-(w_i - w_j) + (a/2E)(\sigma_i + \sigma_j) = 0 \qquad (9a)$$

**(e) *Shear Force-Displacement Equation***

The average shear angle (times twice the panel area) of the curved panel is[3]

$$[w_i + w_j - (w_{i+1} + w_{j+1})]a + [v_{i+1} + v_j - (v_i + v_{j+1})]F_{R0}r_o + [u_i + u_{i+1} - (u_j + u_{j+1})]f_2r_o +$$
$$[\theta_i + \theta_{i+1} - (\theta_j + \theta_{j+1})]f_3r_o^2 = (2r_o/G)\int_0^a \left[q_0\int_{-\varphi}^{\varphi}(1/t)d\psi + q_1\int_{-\varphi}^{\varphi}(1/t)(\psi/\varphi)d\psi + \right.$$
$$\left. q_2\int_{-\varphi}^{\varphi}(1/t)(\psi/\varphi)^2 d\psi + q_3\int_{-\varphi}^{\varphi}(1/t)(\psi/\varphi)^3 d\psi + \ldots\right]dx \qquad (10)$$

If $t$ is constant, the right-hand side of Eq. (10) is

$$(2aL/tG)[q_0 + (1/3)q_2 + (1/5)q_4 + \ldots] \qquad (10a)$$

The functions $F_{R0}$, $f_2$, and $f_3$ are defined in the Appendix. Numerical values are tabulated in Table 1. These functions are proportional to the quantities $|\alpha|$ derived in reference 3—i.e.,

$$2L|\alpha_r| = F_{R0}r_o, \quad 2L|\alpha_t| = f_2r_o, \quad 2L^2|\alpha_n| = f_3r_o^2 \qquad (10b)$$

(3) Longeron Element

***(a) Equilibrium Equation***

Refer to Fig. 4. The equation is

$$-(A_i\sigma_i - A_j\sigma_j) + a[-(q_0 + q_1 + q_2 + \ldots)_i + (q_0 - q_1 + q_2 - q_3 + \ldots)_{i+1}] = 0 \qquad (11)$$

***(b) Force-Displacement Equation***

The equation is (see Appendix)

$$A_i\sigma_i\int_0^a [1 - (x/a)/EA]dx + A_j\sigma_j\int_0^a [(x/a)/EA]\,dx + \int_0^a (\alpha\Delta\tau/E)dx - (w_i - w_j) = 0 \qquad (12)$$

If $A$ is constant and no temperature gradient is present, the equation is the same as Eq. (9a) above.

A numerical example is given below to illustrate the workings of the method applied to a particular problem.

*Numerical Example*—Consider a uniform cantilever circular cylinder with a uniform edge ring loaded symmetrically as shown in Fig. 5. Because of symmetry, only one-half of the structure need be considered. The elements are taken as three curved segmental and three curved panel elements. Each element subtends an angle of 60°. 39 unknown quantities are found to exist as follows:

10 curved segmental element forces: $T_1$, $M_1$, $T_2$, $M_2$, $R_2$, $T_3$, $M_3$, $R_3$, $T_4$, $M_4$

13 shear flow coefficients: $(q_0)_1$, $(q_1)_1$, $(q_2)_1$, $(q_3)_1$; $(q_0)_2$, $(q_1)_2$, $(q_2)_2$, $(q_3)_2$; $(q_0)_3$, $(q_1)_3$, $(q_2)_3$, $(q_3)_3$, $(q_4)_3$

4 axial stresses (at the fixed end of the cylinder): $\sigma_1$, $\sigma_2$, $\sigma_3$, $\sigma_4$

12 displacements: $v_1$, $w_1$, $u_2$, $v_2$, $\theta_2$, $w_2$, $u_3$, $v_3$, $\theta_3$, $w_3$, $v_4$, $w_4$

The necessary 39 equations consist of

$3 \times 3 = 9$ curved segmental element equilibrium
4 axial equilibrium
6 interelement continuity
4 boundary conditions
$3 \times 3 = 9$ curved segmental element force-displacement
4 axial stress-displacement
3 curved panel shear-displacement

The matric equation defining the problem may be written as shown in Fig. 6. A particular structure is analyzed having the following values of elastic and geometric constants:

$$E = 10^7, \quad G = 4 \times 10^6, \quad \varphi_1 = \varphi_2 = \varphi_3 = 30°, \quad \gamma' = (2La/tG) \times 10^3 = 3.90$$

$$I = 10, \quad a = 8.34, \quad \mu' = (Lt/2a) \times 10^3 = 62.8$$

$$r_c = r_o = 25, \quad \kappa = \lambda = 1, \quad \delta' = (a/2E) \times 10^6 = 0.417$$

The multipliers of powers of ten for $\mu$, $\delta$, and $\gamma$ are used because the unit values of displacement and stress are taken as $10^{-3}$ and $10^3$, respectively. Also let $P = 2$.

According to reference 4, the two basic parameters defining the present type of problem of a concentrated loaded flexible frame are

$$A = 6r^6 l/Ia^3; \quad B = 6(G/E)(l/t)(r/a)^2 \qquad (13)$$

The values of the elastic and geometric constants listed above have been chosen so that the values of the two

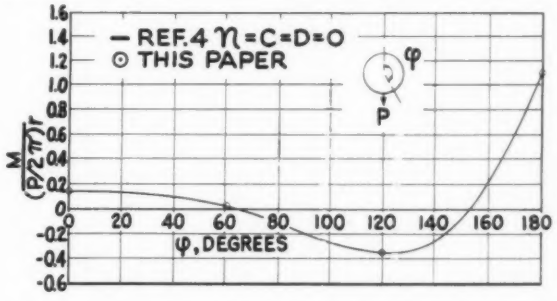


Fig. 8. Moment distribution in the loaded ring of a one field cantilever monocoque for $A = 10^4$, $B = 200$.

parameters $A$ and $B$ are nearly equal to $10^4$ and 200, respectively. Curves showing the shear flow and bending moment distributions are presented in reference 4 for the cantilever cylinder with such values of $A$ and $B$. These curves are repeated here as the solid curves in Figs. 7 and 8. The circled points represent the values calculated from the results obtained by solving the matric equation defined in Fig. 6. These results shown below have been calculated in less than half a minute on the IBM 704 electronic digital machine.

$$
\begin{array}{llllll}
T_1 = -0.027388981 & (q_0)_1 = 0.0070498589 & \sigma_1 = -0.15945223 \\
M_1 = 0.98982704 & (q_1)_1 = 0.0058217902 & \sigma_2 = 0.25492525 \\
T_2 = -0.14856292 & (q_2)_1 = -0.0061917007 & \sigma_3 = 0.32102969 \\
M_2 = 0.16682440 & (q_3)_1 = -0.0020638406 & \sigma_4 = -0.95243589 \\
R_2 = 0.088292236 & (q_0)_2 = -0.019953208 & v_1 = -0.0015006301 \times 10^{-3} \\
T_3 = 0.50179642 & (q_1)_2 = -0.028488696 & w_1 = -0.000066491586 \times 10^{-3} \\
M_3 = -2.7444229 & (q_2)_2 = -0.0013518929 & u_2 = 0.00023987483 \times 10^{-3} \\
R_3 = 0.019316998 & (q_3)_2 = 0.0036772564 & v_2 = 0.0020238958 \times 10^{-3} \\
T_4 = 1.0529797 & (q_0)_3 = -0.046835175 & \theta_2 = -0.00020120508 \times 10^{-3} \\
M_4 = 8.6105814 & (q_1)_3 = 0.024666250 & w_2 = 0.000097962769 \times 10^{-3} \\
 & (q_2)_3 = 0.027570091 & u_3 = -0.0034783675 \times 10^{-3} \\
 & (q_3)_3 = -0.0016133264 & v_3 = 0.0027844979 \times 10^{-3} \\
 & (q_4)_3 = -0.0037883632 & \theta_3 = 0.00016191069 \times 10^{-3} \\
 & & w_3 = 0.00013386935 \times 10^{-3} \\
 & & v_4 = -0.0086417254 \times 10^{-3} \\
 & & w_4 = -0.00039716752 \times 10^{-3}
\end{array}
$$

The error function obtained by substituting the above results back into the matrix is

$$
\begin{array}{lll}
\epsilon_1 = -0.00000071 & \epsilon_{14} = 0.00000021 & \epsilon_{27} = -0.00000006 \\
\epsilon_2 = -0.00000025 & \epsilon_{15} = 0.00000023 & \epsilon_{28} = -0.000000006 \\
\epsilon_3 = 0.000000015 & \epsilon_{16} = -0.000000007 & \epsilon_{29} = -0.0000009 \\
\epsilon_4 = 0.0000000036 & \epsilon_{17} = -0.00000044 & \epsilon_{30} = 0 \\
\epsilon_5 = -0.000000008 & \epsilon_{18} = 0.00000017 & \epsilon_{31} = 0.00000004 \\
\epsilon_6 = -0.00000039 & \epsilon_{19} = 0.00000025 & \epsilon_{32} = -0.00000024 \\
\epsilon_7 = -0.00000019 & \epsilon_{20} = 0.00000001 & \epsilon_{33} = 0 \\
\epsilon_8 = -0.00000013 & \epsilon_{21} = 0.00000052 & \epsilon_{34} = 0 \\
\epsilon_9 = 0.00000035 & \epsilon_{22} = 0.00000007 & \epsilon_{35} = 0 \\
\epsilon_{10} = -0.000000070 & \epsilon_{23} = 0.00000018 & \epsilon_{36} = -0.000000002 \\
\epsilon_{11} = -0.000000047 & \epsilon_{24} = 0 & \epsilon_{37} = 0.00000007 \\
\epsilon_{12} = 0.000000048 & \epsilon_{25} = 0.00000012 & \epsilon_{38} = -0.00000004 \\
\epsilon_{13} = -0.000000027 & \epsilon_{26} = 0.00000039 & \epsilon_{39} = 0.00000014
\end{array}
$$

The worst error is associated with Eq. (29). However, since only eight significant figures have been carried in the computations, the results may be considered very accurate as far as the matrix inversion is concerned. Examination of Figs. 7 and 8 reveals close agreement for the shear flow and very close agreement for the bending moment when compared with the values obtained in reference 4.

## Appendix

The functions, $f$ and $F$, appearing in various equations in the text, are defined as follows:

$$f_1 = \tan\phi; \quad f_2 = -[(F_{R0})_{\kappa=\lambda=1} - 2]f_1; \quad f_3 = \beta - f_2; \quad f_4 = (\tan\phi/\phi) - 1; \quad f_5 = (\tan\phi/\phi)^{-1} - 1$$

$$F_{V1} = 2f_4; \quad F_{V3} = 4 + 6(1 - 2\phi^{-2})f_4; \quad F_{H2} = 2(1 + 2\phi^{-2}f_5)$$

$$F_{H4} = 2[1 - 8\phi^{-2} + 4\phi^{-2}(1 - 6\phi^{-2})f_5]$$

$$F_{R0} = 2 + 2\{(r_o/r_c)\ [\beta(1 + \cos\beta) - 2\sin\beta] - (\kappa - \lambda)\sin\beta\}/\Delta_r$$

$$F_{R2} = \{2(r_o/r_c)\ 8\phi^{-1}\ [\cos\phi - (\sin\phi/\phi)] + 4[\sin\phi - (\phi/3)\cos\phi]\}/\Delta_{r'} +$$
$$\{16\lambda\phi^{-1}\ [\cos - (\sin\phi/\phi)] - 4(\kappa - \lambda)(1 - 2\phi^{-2})\sin\phi\}/\Delta_{r'} - 2(1 - 2\phi^{-2}) - 4(\kappa - \lambda)\phi^{-1}(1 + \beta^{-1}\sin\beta)/\Delta_{r'}$$

$$F_{R4} = 8(r_o/r_c)\{[1 - 12\phi^{-2}(1 - 2\phi^{-2})]\sin\phi - [(\phi/5) - 4\phi^{-1}(1 - 6\phi^{-2})]\cos\phi\}/\Delta_{r'} -$$
$$32\lambda\ [3\phi^{-2}(1 - 4\phi^{-2})\sin\phi - \phi^{-1}(1 - 12\phi^{-2})\cos\phi]/\Delta_{r'} - 4(\kappa - \lambda)\{[1 - 12\phi^{-2}(1 - 2\phi^{-2})] \times$$
$$\sin\phi - 24\phi^{-3}(1 + \beta^{-1}\sin\beta)\}/\Delta_r' - 2[1 - 12\phi^{-2}(1 - 2\phi^{-2})]$$

$$F_{T1} = (F_{T1})_1 + (F_{T1})_2; \quad F_{T3} = (F_{T3})_1 + (F_{T3})_2$$

$$(F_{T1})_1 = 8(r_o/r_c)\left\{\cos\phi + [(\phi^2/3) - 1](\sin\phi/\phi)\right\}/\Delta_t'$$

$$(F_{T1})_2 = 8[-(\kappa - 1)(\sin\phi/\phi) + (1/2)(\kappa - \lambda)\cos\phi]/\Delta_{t'} + (2\phi^{-1})$$

$$(F_{T3})_1 = 4(r_o/r_c)\left\{[(2/5)\phi^2 - 6(1 - 2\phi^{-2})](\sin\phi/\phi) + 2(1 - 6\phi^{-2})\cos\phi\right\}/\Delta_{t'}$$

$$(F_{T3})_2 = 4\left\{2(1 - 6\phi^{-2})(\sin\phi/\phi) - 6\kappa[2\phi^{-2}\cos\phi + (1 - 4\phi^{-2})(\sin\phi/\phi)] + (\kappa - \lambda)(1 - 6\phi^{-2})\cos\phi\right\}/\Delta_{t'} + 6\phi^{-1}(1 - 2\phi^{-2})$$

$$F_{M1} = f_4(F_{T1})_1 + (\beta/3); \quad F_{M3} = (r_c/r_0)[f_4(F_{T3})_2 - 2\phi^{-1}F_{V3}] + f_4(F_{T3})_1 + (\beta/5) \tag{A-1}$$

where
$$\kappa = 1 + (I/r_c^2)(A^{-1} + A^{*-1}); \quad \lambda = 1 + (I/r_c^2)(A^{-1} - A^{*-1}) \tag{A-1a}$$

and
$$\Delta_r = \kappa\beta - \lambda\sin\beta; \quad \Delta_{r'} = \Delta_r \sec\phi \tag{A-1b}$$

$$\Delta_t = \kappa\beta + \lambda\sin\beta - (4/\beta)(1 - \cos\beta); \quad \Delta_{t'} = \Delta_t \sec\phi \tag{A-1c}$$

Numerical values of the various functions are listed in Table 1 for several values of $\varphi$, given in degrees. The functions involving $\kappa$, $\lambda$ and $(r_o/r_c)$ as parameters are presented only for the limiting case of $\kappa = \lambda = (r_o/r_c) = 1$.

***Stiffnesses***

The values of the stiffnesses appearing in Eq. (3) of the text are

$$\begin{bmatrix} S_{mm} & S_{mr} & S_{mt} \\ S_{rm} & S_{rr} & S_{rt} \\ S_{tm} & S_{tr} & S_{tt} \end{bmatrix} = \frac{EI}{r_c^3}\begin{bmatrix} r_c f_4 S_{tt}(r_c^3/EI) & 0 & 0 \\ 0 & S_{rr}(r_c^3/EI) & 0 \\ 0 & 0 & S_{tt}(r_c^3/EI) \end{bmatrix}\begin{bmatrix} r_c f_4 & -f_1 & 1 \\ -r_c f_1 & 1 & f_1 \\ r_c f_4 & -f_1 & 1 \end{bmatrix} + \frac{EI}{r_c}\begin{bmatrix} (1/\varphi) & 0 & 0 \\ 0 & 0 & 0 \\ 0 & 0 & 0 \end{bmatrix} \tag{A-2}$$

where
$$S_{rr}(r_c^3/EI) = 2(1 + \cos\beta)/\Delta_r; \quad S_{tt}(r_c^3/EI) = 2(1 + \cos\beta)/\Delta_t \tag{A-2a}$$

It is to be noted that
$$S_{tm} = S_{mt} \quad \text{and} \quad S_{rt} = -r_c S_{rm} \tag{A-2b}$$

Numerical values are listed in Table 2 for various values of $\varphi$, for the limiting case of $\kappa = \lambda = 1$. To obtain numerical values for other values of $\kappa$ and $\lambda$, multiply $S_{rm}$, $S_{rr}$, and $S_{rt}$ by

$$(\beta - \sin\beta)/(\kappa\beta - \lambda\sin\beta) \tag{A-2c}$$

and the remaining stiffnesses by

$$[\beta + \sin\beta - (4/\beta)(1 - \cos\beta)]/[\kappa\beta + \lambda\sin\beta - (4/\beta)(1 - \cos\beta)] \tag{A-2d}$$

***Force-Displacement Equations for a General Curved Segmental Element***

The equations are derived by the use of the principle of virtual displacements.[5] For each equation a system of self-equilibrating dummy loads is required. The systems chosen consist of a unit positive moment, radial force, and tangential force applied in turn at the end of the element designated $i$ (from which the coordinate $\psi'$ is measured in Fig. 1) with the necessary equilibrating set of forces (and moment) applied at the other end of the element in each case. The work done by the dummy loads in each system must vanish. Internal work is comprised of bending, stretching, shearing, and temperature distortion work of bending and stretching. Mathematically, the three conditions become

$$\theta_i - \theta_{i+1} = \int_0^\beta (r_c M/\overline{EI})d\psi' + \int_0^\beta r_c\left(\int_A \alpha E\Delta\tau y dA/\overline{EI}\right)d\psi' \tag{A-3a}$$

$$v_i - v_{i+1}\cos\beta + (u_{i+1} - r_{c_{i+1}}\theta_{i+1})\sin\beta = \int_0^\beta (Mr_c^2\sin\psi'/\overline{EI})d\psi' + \int_0^\beta (r_c V\cos\psi'/\overline{EA^*})d\psi' - \int_0^\beta (r_c P\sin\psi'/EA)d\psi' + (I_{\Delta\tau})_2 \tag{A-3b}$$

$$u_i - u_{i+1}\cos\beta - \theta_{i+1}(r_{c_i} - r_{c_{i+1}}\cos\beta) - v_{i+1}\sin\beta = \int_0^\beta [r_c^2 M(1 - \cos\psi')/\overline{EI}]d\psi' + \int_0^\beta (r_c V\sin\psi'/\overline{EA^*})d\psi' + \int_0^\beta (r_c P\cos\psi'/\overline{EA})d\psi' + r_{c_i}(I_{\Delta\tau})_1 + (I_{\Delta\tau})_3 \tag{A-3c}$$

where $M$, $V$, and $P$ are the bending moment, shear force, and axial force acting in any cross section of the element, and the integrals are taken from point $i$ to point $i + 1$. It is convenient to add $-r_{c_i}$ times Eq. (A-3a) to Eq. (A-3c). In this manner Eqs. (4) of the text are derived.

***Force-Displacement Equation for a Longeron and Axial Stress-Displacement Equation***

Eqs. (9) and (12) of the text are derived directly from the following basic relations:

$$(dw/dx) - \epsilon_{\Delta\tau} = \sigma/E = P/E.1,$$
$$P = P_i + (x/a)(P_j - P_i), \quad \epsilon_{\Delta\tau} = \alpha\Delta\tau/E \quad \text{(A-4)}$$

For a longeron, $P$ presents the axial load; for a curved panel element, the load per inch is used—i.e., $P = t\sigma$.


### References

[1] Klein, B., *A Simple Method of Matric Structural Analysis*, Journal of the Aeronautical Sciences, Vol. 24, No. 1, pp. 49–46, January, 1957.

[2] Klein, B., *A Simple Method of Matric Structural Analysis: Part II—Effects of Taper and a Consideration of Curvature*, Journal of the Aeronautical Sciences, Vol. 24, No. 11, pp. 813–820, November, 1957.

[3] Hoff, N. J., Boley, B. A., and Klein, B., *Stresses in and General Instability of Monocoque Cylinders With Cutouts—II Calculation of Stresses in a Cylinder With a Symmetric Cutout*, NACA TN 1014, 1946.

[4] Hoff, N. J., Salerno, V. L., and Boley, B. A., *Shear Stress Concentration and Moment Reduction Factors for Reinforced Monocoque Cylinders Subjected to Concentrated Radial Loads*, Journal of the Aeronautical Sciences, Vol. 16, No. 5, pp. 277–288, May, 1949.

[5] Hoff, N. J., *Minimal Principles of Structural Analysis*, John Wiley & Sons, Inc., New York, 1954.


## A Pilot Analog for Airplane Pitch Control

(*Continued from page 379*)


### References

[1] Diamantides, N. D., *Informative Feedback in Jet-Pilot Control-Stick Motion*, AIEE Transactions on Applications and Industry, No. 33, pp. 243–249, November, 1957.

[2] *The Human Pilot*, Northrop Aircraft, Inc., Navy BuAer Report AE-61-4 III, pp. 11–81, Washington, D.C., August, 1954.

[3] Grief, H. D., *Describing Method of Servomechanism Analysis Applied to Most Commonly Encountered Nonlinearities*, AIEE Paper No. 53–524, 1953.

[4] Wiener, Norbert, *Cybernetics or Control and Communication in the Animal and the Machine*, pp. 113–114, 133, John Wiley and Sons, Inc., New York, 1948.

[5] Tustin, A., *The Nature of the Operator's Response in Manual Control and Its Implications for Controller Design*, Journal, Institution of Electrical Engineers, Vol. 94, Part IIa, No. 2, pp. 190–202, London, 1947.

[6] Sziglc, C. H., and Stubbs, G. S., *Transport Delay Simulation Circuit*, Report WAPD-T-39, Westinghouse Electric Corp., Pittsburgh, Pa.

[7] *Final Report Human Dynamics Study*, BuAer Contract NOa(s)-51-083-c, GER-4750, Goodyear Aircraft Corp., Akron, Ohio, April 8, 1952.

[8] *Random Noise Generator for Simulation Studies*, GER-6436, Goodyear Aircraft Corp., Akron, Ohio, December 13, 1954.

[9] Lindsay, R. B., *Introduction to Physical Statistics*, Chapter 2, John Wiley and Sons, Inc., New York, 1941.

[10] Bates, J. A. V., *Some Characteristics of a Human Operator*, Journal, Institution of Electrical Engineers, Vol. 94, Part IIa, pp. 298–304, London, 1957.

[11] Cacippo, A. J., *Pilot Information Utilization: A Study in Human-Response Dynamics*, ASME Paper No. 56-A-149, pp. 25–31, New York, November, 1956.


## Compressive Buckling of a Long Simply Supported Plate

(*Continued from page 384*)

mined by noting that, when the foundation is rigid, the required buckle pattern will be as shown in Fig. 3. The compressive buckling load of this configuration is that of a flat plate with clamped loaded edges and simply supported unloaded edges and is available in reference 1. The lowest value of $k$ compatible with the criterion of no change in sign of the deflection function is

$$k = 16/3 \quad \text{(13a)}$$

and the corresponding value of $\lambda/b$ is

$$\lambda/b = \sqrt{3}/2 \quad \text{(13b)}$$

The value of $c$ is, of course, zero since the foundation does not deflect.

It can thus be seen that the lack of attachment of the plate to the foundation results in a drastic reduction in the buckling stress coefficient, from a value limited only by the inelastic properties of the plate material to a maximum possible value of 16/3, or only a 33 per cent increase above the plate without a foundation.


### Reference

[1] Timoshenko, S., *Theory of Elastic Stability*, p. 364; McGraw-Hill Book Company, Inc., New York, 1936.



## Water-Based Helicopter Symposium

*Stevens Institute of Technology, Hoboken, N.J., June 27, 1958*

The first Water-Based Helicopter Symposium to be held at Stevens Institute of Technology is being sponsored by the Bureau of Aeronautics, Department of the Navy, and Stevens.

Several papers dealing with the operational concepts and hydrodynamic requirements of water-based helicopters will be presented by representatives of the services, Government, industry, and university.

# Readers' Forum

*BRIEF REPORTS of investigations in the aeronautical sciences and discussions of papers published in the JOURNAL are presented in this special department. Entries must be restricted to a maximum of 1,300 words or the equivalent of one JOURNAL page including formulas and illustrations. Publication is completed as soon as possible after receipt of the material. The Editorial Committee does not hold itself responsible for the opinions expressed by the correspondents.*

## Contents


On a Subsonic Compressibility Correction for Propellers and Rotors ..... SVETOPOLK PIVKO 395

Analysis of a Transpiration-Cooled Hemisphere-Cylinder ..... CHARLES J. SCOTT 397

Note on Mechanical Behavior After Creep ..... GEORGE GERARD 397

Note on the Lift of Slender Nose Shapes According to Newtonian Theory ..... J. D. COLE 399

On the Reduction of Maximum Loads in Nonlinear Viscoelastic Columns ..... HARRY H. HILTON 399

On Heat Transfer in Slip Flow ..... STEPHEN H. MASLEN 400

An Approximate Method for Determining the Wave Drag of Axisymmetric Conical Cowls ..... JOHN W. BROOK 401

The Determination of the Shear Center for a Special Solid Symmetrical Airfoil ..... ALPHONSE J. SISTINO 402

Fundamental Solutions for Heat Transfer From Nonisothermal Flat Plates ..... DONALD C. BAXTER AND WILLIAM C. REYNOLDS 403

Reduction of Ikenberry-Truesdell Equations to Burnett Equations for Slip Flow ..... HSUN-TIAO YANG 404

On Hypersonic Stagnation-Point Flow With a Magnetic Field ..... NELSON H. KEMP 405

Note on the Stabilizing Effect of Centrifugal Forces on the Laminar Boundary Layer Over Convex Surfaces ..... LESTER LEES 407

An Evaluation of the Criticisms by Topping of Marin's Strength Hypothesis ..... JOHN J. COLEMAN 408


## On a Subsonic Compressibility Correction for Propellers and Rotors


Svetopolk Pivko
*Aerotechnical Institute, Beograd-Žarkovo, Yugoslavia*


January 24, 1958


THE EFFECT of compressibility for propellers can be approximately predicted by applying the blade-element theory, and a general subsonic compressibility correction can be obtained in the form of a ratio of the thrust and torque coefficient values in subsonic flow to the corresponding values in incompressible flow. The effect of compressibility for each section of the propeller blade can be approached by the linearized Prandtl-Glauert correction for two-dimensional subsonic flow. As the actual varying inflow velocity distribution has a negligible effect in predicting the ratio of the propeller characteristics, the constant inflow can be assumed as given by the Theodorsen theory[1] and the momentum theory for compressible fluid.[2]

The thrust and torque of a blade element at radius $r$ can be expressed as follows:

$$dT = (1/2)B\rho_1 W^2 C_L(\cos\phi - \sin\phi \tan\epsilon)c\, dr \qquad (1)$$

$$dQ = (1/2)B\rho_1 W^2 C_L(\sin\phi + \cos\phi \tan\epsilon)c\, r\, dr \qquad (2)$$

where

$$W^2 \approx [V_0 + (w/2)]^2 + r^2\omega^2 = R^2\omega^2(\lambda_1^2 + x^2)$$

$$\phi = \tan^{-1}\{[V_0 + (w/2)]/r\omega\} = (\lambda/x)[1 + (\bar{w}/2)] = \lambda_1/x$$

$$x = r/R, \quad \bar{w} = w/V_0, \quad \lambda = V_0/R\omega, \quad \lambda_1 = \lambda[1 + (\bar{w}/2)]$$

In these expressions, $B$ is the number of blades, $\rho_1$ = air density at propeller, $R$ = propeller radius, $c$ = blade-section chord, $\tan\epsilon = C_D/C_L$ = ratio of section drag and lift coefficients, $W$ = resultant local velocity relative to the propeller blade element, assuming constant inflow and neglecting the slipstream rotation, $V_0$ and $\omega$ = propeller axial advance and angular velocity, respectively, and $w$ = increase of the axial velocity in the slipstream.

### Contributors Please Note

Readers' Forum items must be confined to the equivalent of one page in the *Journal*. Contributions that exceed this limit will be returned to the authors for condensation and rewrite. To avoid inconvenience and delay, please adhere to the following specifications:

(1) Five, double-spaced, typewritten, manuscript pages ($8\frac{1}{2}$ by 11 in.), including wide margins, formulas, and headings equal one printed page.

(2) For every illustration deduct at least one-half or as much as one manuscript page, depending on the size of the illustration.

Substituting these expressions into Eqs. (1) and (2), and setting

$$C_L \approx (C_L)_{inc}/[1 - (W/a_1)^2]^{1/2} \tag{3}$$

where $a_1$ is the velocity of sound at the propeller, the values $T$ and $Q$ can be found by integrating Eqs. (1) and (2), assuming a constant $w$, constant chord $c$, and constant lift coefficient for incompressible flow $(C_L)_{inc}$ along the entire radius. For the corresponding incompressible case, the integration of Eqs. (1) and (2) for the same propeller gives $T_{inc}$ and $Q_{inc}$. Thus, one obtains the ratios

$$T/T_{inc} = C_T/(C_T)_{inc} = (\rho_1/\rho_0)\,[(A - B\tan\epsilon)/(A_0 - B_0\tan\epsilon)] \tag{4}$$

$$Q/Q_{inc} = C_Q/(C_Q)_{inc} = C_P/(C_P)_{inc} = (\rho_1/\rho_0)\,[(C + D\tan\epsilon)/(C_0 + D_0\tan\epsilon)] \tag{5}$$

where $A$, $A_0$, $B$, $B_0$, $C$, $C_0$, $D$, and $D_0$ are functions of

$$M_1 = (V_0/a_1)\,[1 + (\bar{w}/2)], \quad M_{R1} = R\omega/a_1$$

and

$$M_{W1} = (M_1^2 + M_{R1}^2)^{1/2}$$

If one is justified in neglecting the term $\tan\epsilon = C_D/C_L$, Eqs. (4) and (5) reduce to

$$\frac{C_T}{(C_T)_{inc}} = \frac{C_Q}{(C_Q)_{inc}} = \frac{C_P}{(C_P)_{inc}} = \frac{\rho_1}{\rho_0}\frac{A}{A_0} = \frac{\rho_1}{\rho_0}\cdot\frac{3}{2}\left[\frac{\sin^{-1}M_{W1} - \sin^{-1}M_1 - M_{W1}(1 - M_{W1}^2)^{1/2} + M_1(1 - M_1^2)^{1/2}}{M_{W1}^3 - M_1^3}\right] \tag{6}$$

It is interesting to note that in this case the propeller efficiency is not dependent upon Mach Number,

$$\eta = \eta_{inc} \tag{7}$$

The first-order effects of density $\rho_1$ and velocity of sound $a_1$ at the propeller[2] may be easily obtained as functions of $M_0 = V_0/a_0$; thus,

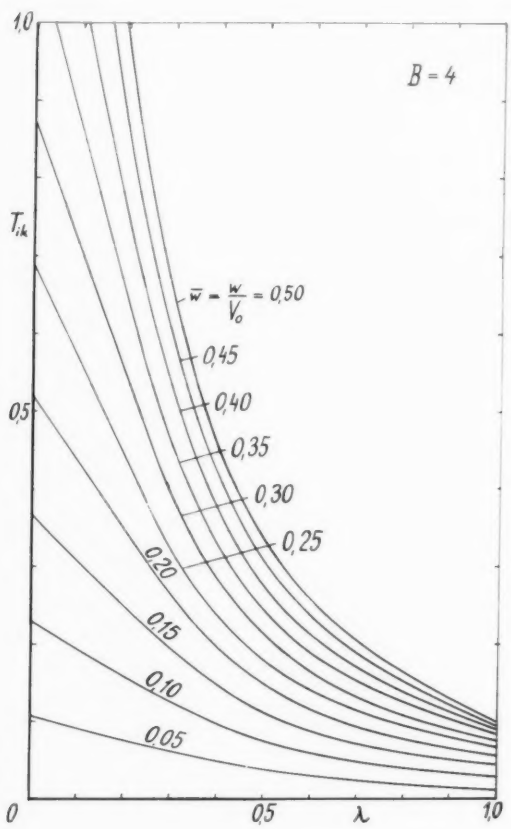


FIG. 1.

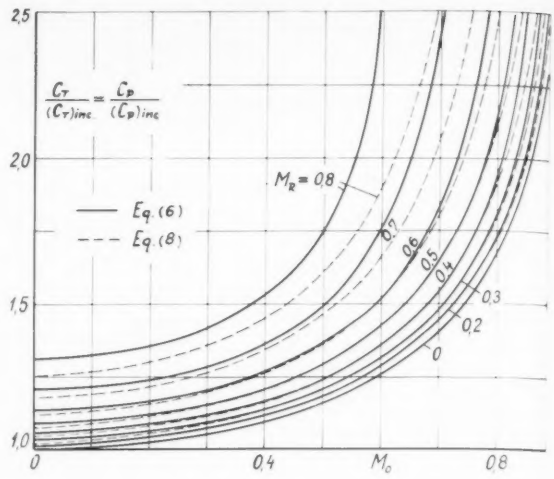


FIG. 2.

$$\rho_1/\rho_0 \approx 1 - 0.5\bar{w}M_0^2, \quad a_1/a_0 \approx 1 - 0.1\,\bar{w}M_0^2$$

where $\bar{w}$ is approximately given by

$$\bar{w} = w/V_0 \approx T_k/2 = (1/2)\,[T/(\rho_0/2)V_0^2\pi R^2]$$

The more exact magnitude of $\bar{w}$ can be evaluated from the data measured by Theodorsen[1] using an electrical-analogy method. Fig. 1 shows a graph for a four-bladed single-rotating propeller from which the values of $\bar{w}$ can be read directly without any laborious calculations. Since the effect of $a_1$ is very small, and if one is interested in only the first-order compressibility corrections, the substitutions

$$M_1 \approx M_0 = V_0/a_0, \quad M_{R1} \approx M_R = R\omega/a_0$$

and

$$M_{W1} \approx M_W = (M_0^2 + M_R^2)^{1/2}$$

where $a_0$ is the velocity of sound of undisturbed flow, may be introduced into Eq. (6). Fig. 2 shows a plot of Eq. (6) with these substitutions, with $\rho_1 = \rho_0$ and for constant values of $M_R$. The dotted lines shown for comparison are those given by the simple Prandtl-Glauert rule[2]

$$C_T/(C_T)_{inc} \approx 1/(1 - M_{3/4}^2)^{1/2} \tag{8}$$

using the helical Mach Number occurring at the three-quarter radius

$$M_{3/4} = \{M_0^2 + [(3/4)M_R]^2\}^{1/2}$$

From Fig. 2 it is evident that this simple compressibility correction provides a satisfactory approximation as long as the Mach Number remains less than 0.6.

Since the blade-section compressibility correction as given by Eq. (3) is restricted by the limitations of the linearized subsonic flow theory, it may be assumed that the corrections evaluated by Eqs. (4), (5), and (6) are limited by the critical Mach Number of 0.8 or less. A comparison with available experimental data[2] proves that the derived theoretical results are valid as long as the Mach Number of 0.8 is not exceeded. These experimental results prove also that the compressibility has a negligible effect on the propeller efficiency [see Eq. (7)].

## REFERENCES

[1] Theodorsen, T., *Theory of Propellers*, McGraw-Hill Book Company, Inc., New York, 1948.

[2] Laitone, E., and Talbot, L., *Subsonic Compressibility Corrections for Propellers and Helicopter Rotors*, Journal of the Aeronautical Sciences, Vol. 20, No. 10, pp. 683–690, October, 1953.

[4] Stack, J., Draley, E., Delano, J., and Feldman, L., *Investigation of the NACA 4-308-03 and NACA 4-308-045 Two-Blade Propellers at Forward Mach Numbers to 0.725 to Determine the Effects of Compressibility and Solidity on Performance*, NACA Report 999, 1950.

## Analysis of a Transpiration-Cooled Hemisphere-Cylinder*

Charles J. Scott
*Rosemount Aeronautical Laboratories, University of Minnesota, Minneapolis, Minn.*
January 24, 1958

An extension of the analysis of Stine and Wanlass[1] is presented, which predicts the effect of air injection on the heat-transfer distribution over isothermal blunt-nosed bodies of revolution. Only advance knowledge of the surface pressure distribution is required. Results are presented for a transpiration-cooled hemisphere-cylinder at a free-stream Mach Number of 3.6.

The Mangler transformation and the Stewartson-Illingworth transformation were used to relate the problem in axisymmetric compressible flow to two-dimensional compressible flow (+ superscript) and then to an approximately equivalent two-dimensional incompressible flow (* superscript) where the thermal solutions of the Falkner-Skan wedge-flow cases presented in reference 2 were applied. The effects of the major assumptions—constant Prandtl Number, small temperature differences, and local application of the Falkner-Skan solutions—have been discussed in reference 3. No additional assumptions were required to extend the analysis to the case of air injection.

Writing a heat balance over an element of the surface, the equation

$$q = h\,(T_{aw} - T_w) = \rho_w v_w c_{p_w}\,(T_w - T_c) \qquad (1)$$

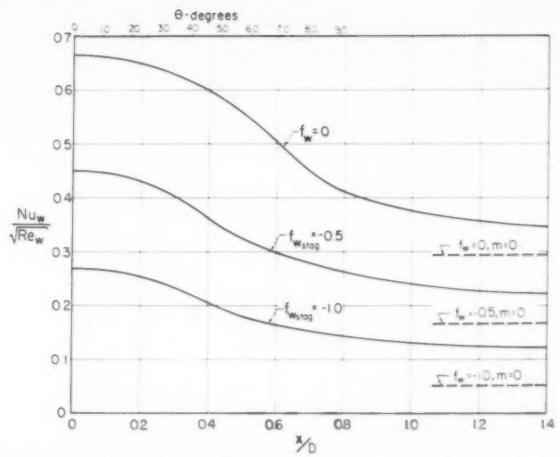


Fig. 1. Distribution of local heat-transfer parameter for three values of the blowing parameter $f_w$.

defines the heat-transfer coefficient for this case. Introducing the relations

$$\left.\begin{aligned} f_w &= -[2v_w/(m+1)]\sqrt{\rho_w x/\mu_w U_\delta};\\ Nu_w &= hx/k_w; \quad U_\delta = C x^m \end{aligned}\right\} \qquad (2)$$

then for constant coolant and wall temperature, $(T_c, T_w)$, we may write

$$(f_w/f_{w_{stag.}}) = [(Nu/\sqrt{Re})/(Nu/\sqrt{Re})_{stag.}]\cdot[2/(m+1)] \qquad (3)$$

Mangler's transformation results in

$$(Nu/\sqrt{Re})/(Nu/\sqrt{Re})^+ = \sqrt{x r_0^2 \Big/ \int_0^x r_0^2\,dx} =$$

$$\sqrt{m/m^+} = (f_w/f_w^+)\cdot[(m+1)/(m^+ + 1)] \qquad (4)$$

The Stewartson-Illingworth transformation for $\gamma = 1.4$ produces

$$[(Nu/\sqrt{Re})^+/(Nu/\sqrt{Re})^*] = \sqrt{x^+(a_\delta/a_0)^8 \Big/ \int_0^{x^+} (a_\delta/a_0)^8 dx^+} = \sqrt{[1 + (M\delta^2/5)]\,(m^+/m^*)} = (f_w^+/f_w^*)[(m^* + 1)/(m^+ + 1)] \qquad (5)$$

In applying these equations to a hemisphere-cylinder the local Mach Number and Euler Number $(m)$ may be evaluated from the modified Newtonian law, $C_p/C_{p_{max}} = \cos^2\theta$, if the flow just outside the boundary layer is taken to be isentropic. Once Eqs. (4) and (5) are solved, the solution of Eq. (3) is found by a trial-and-error procedure using the tabulated solutions of reference 2. The results presented in Fig. 1 display the distribution of the local heat-transfer parameter along the isothermal surface. The uniform decrease in local heat-transfer coefficients with air injection is apparent. The value of the blowing parameter, $f_w$, varies with angular location and approaches asymptotically, as does the heat-transfer parameter, the corresponding flat-plate values.

### References

[1] Stine, H. A., and Wanlass, K., *Theoretical and Experimental Investigation of Aerodynamic-Heating and Isothermal Heat Transfer Parameters on a Hemispherical Nose with Laminar Boundary Layer at Supersonic Mach Numbers*, NACA TN 3344, 1954.

[2] Livingood, J. N. B., and Donoughe, P. L., *Summary of Laminar-Boundary-Layer Solutions for Wedge-Type Flow Over Convection- and Transpiration-Cooled Surfaces*, NACA TN 3588, 1955.

[3] Lees, Lester, *Laminar Heat Transfer Over Blunt-Nosed Bodies at Hypersonic Flight Speeds*, Jet Propulsion, Vol. 26, No. 4, pp. 259–269, 274, April, 1956.

[4] Scott, C. J., *Analysis of a Transpiration-Cooled Hemisphere-Cylinder*, University of Minnesota, Rosemount Aeronautical Laboratories Engineering Memorandum 74, December, 1957.

* This research was partially supported by the Air Force Office of Scientific Research under Contract AF 18 (600)-1226.

## Note on Mechanical Behavior After Creep

George Gerard
*Assistant Director of Research, College of Engineering, New York University*
February 21, 1958

### Introduction

For aircraft or missiles operating in a thermal environment, it is of interest to consider the mechanical properties of materials at elevated temperatures after creep has occurred. For example, in the superposition of a sudden maneuver upon steady-state loading, such data would be of interest.

### Commercially Pure Aluminum

To obtain some information on the short-time characteristics of materials after prior creep, the following tests were conducted on 3003-0 aluminum (commercially pure). The tests utilized round tubes at 650°F. under compression or torsion and were conducted in three parts, as follows.

(a) To establish the basic short-time stress-strain characteristics of 3003-0 at 650°F., load was applied at a strain rate of approximately 0.002 min.$^{-1}$ after soaking at temperature for 1

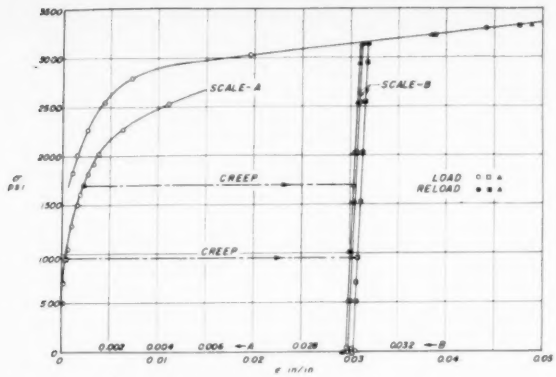


FIG. 1. Effect of prior compressive creep on the short-time elevated-temperature compressive properties of 3003-0 aluminum after exposure at 650°F.

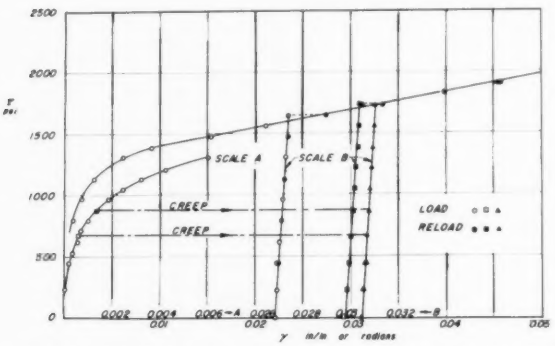


FIG. 2. Effect of prior shear creep on the short-time elevated temperature shear properties of 3003-0 aluminum after exposure at 650°F.

hour. At a strain of approximately 0.03 the specimen was unloaded and then reloaded to a strain of approximately 0.06.

(b) In the first prior creep strain experiment, a specimen identical to that used in (a) was loaded to a stress level in the neighborhood of the proportional limit after soaking at 650°F. for 1 hour. The specimen was then allowed to creep under this constant stress until a strain of approximately 0.03 had been reached. The specimen was then unloaded and reloaded to a strain of approximately 0.06 in order to obtain the short-time stress-strain characteristics after prior strain.

(c) The second prior strain experiment was identical to (b) except that the stress level under creep conditions was roughly half way between the proportional limit and the 0.002 offset yield stress.

The results of the experiments on 3003-0 aluminum at 650°F. are shown in Fig. 1 for compression loading and in Fig. 2 for shear loading. An examination of these Figures reveals the highly significant fact that for commercially pure aluminum at 650°F. under exposure times up to 80 hours, *the path of prior creep straining has no significant influence upon the reloading path.* This is vividly demonstrated in Figs. 1 and 2, where all reloading paths at approximately 0.03 strain, regardless of the path of prior straining, follow an elastic path until the original short time stress-strain curve is reached and then follow essentially the same plastic path.

## Aluminum Alloy

The above results apply to a simple material which is highly suitable for fundamental creep studies. In structural applications, it is pertinent to consider the behavior of the more complex alloys under prior strain conditions similar to those considered above. Here the effects of aging and deterioration depend significantly upon exposure time and it is possible that the behavior after prior straining may differ from that observed on the 3003-0 aluminum.

For this purpose, test data of Beck[1] on the tensile properties of Alclad 2024-T3 aluminum alloy sheet after prior tensile creep at 500°F. are significant. The results shown in Fig. 3 for 2 hours exposure indicate a possible strengthening of the material due to aging. Those shown in Fig. 4 are definitely indicative of the deterioration of this material after 90 hours exposure.

It is significant to note that, in all cases shown in Figs. 3 and 4, the short-time reloading path following prior creep is always elastic for an appreciable stress range beyond that corresponding to the creep stress level. However, the deterioration in properties shown in Fig. 4 indicates that under sufficient exposure times, the short-time reloading path may not be elastic beyond the prior creep stress level.

To conclude, it appears that for 3003-0 aluminum the short-time reloading path is independent of the prior strain path under the conditions of the experiments. For an alloy such as 2024-T3 under the test conditions of reference 1, the more restrictive conclusion, that the short-time reloading path after prior straining is elastic considerably beyond the creep stress level, can be made. However, there are indications that for an alloy under sufficient exposure times the short-time reloading path may not be elastic beyond the prior creep stress level.

## Reference

[1] Beck, C. E., *The Effect of Prior Creep on the Mechanical Properties of Alclad 2024-T3 Aluminum Alloy Sheet*, WADC TN 55-49, September, 1955

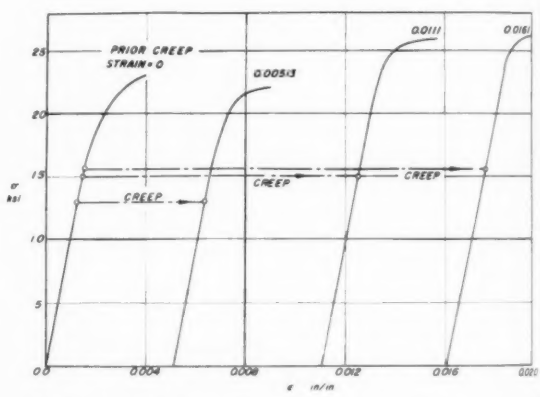


FIG. 3. Effect of prior tensile creep on the short-time elevated-temperature tensile properties of Alclad 2024-T3 aluminum alloy sheet after 20 hours' exposure at 500°F.

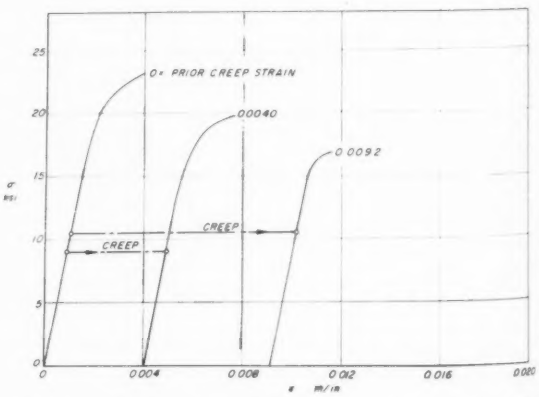


FIG. 4. Effect of prior tensile creep on the short-time elevated-temperature tensile properties of Alclad 2024-T3 aluminum alloy sheet after 90 hours' exposure at 500°F.

## Note on the Lift of Slender Nose Shapes According to Newtonian Theory

J. D. Cole
Consultant, The RAND Corporation, Santa Monica, Calif.
February 24, 1958

NEWTONIAN THEORY for slender bodies of revolution (thickness ratio $\delta$) at zero incidence predicts a pressure coefficient $0(\delta^2)$ and similar flows for a given value of the Newtonian parameter

$$N = (\gamma + 1)/(\gamma - 1)M_\infty^2\delta^2$$

(See reference 1). The pressure on the surface is independent of $N$.

A calculation based on the same idea can be carried out for angle of attack $\alpha$ where the part of the pressure coefficient which contributes to lift is $0(\delta\alpha)$. The problem is considered as a small perturbation on the solution at zero incidence. The following form of expansion is assumed:

$$\bar{q}(\bar{x}, \bar{r}, \theta; M_\infty, \delta, \alpha)/U = \vec{i} + \delta\{F' + \lambda\bar{v}_0(\bar{x}, \bar{r}; N) + \lambda\alpha^*\bar{v}_1(\bar{x}, \bar{r}, \theta; N)\} + \delta\alpha^*\vec{i}_\theta[w_1(\bar{x}, \bar{r}, \theta; N) - \sin\theta]$$

$$\rho/\rho_\infty = [\sigma_0(\bar{x}, \bar{r}; N)/\lambda]\{1 + \alpha^* s_1(\bar{x}, \bar{r}, \theta; N)\}$$

$$(P - P_\infty)/\rho_\infty U^2 = \delta^2\{p_0(\bar{x}, \bar{r}; N) + \alpha^* p_1(\bar{x}, \bar{r}, \theta; N)\}$$

The body shape is

$$\bar{r} = \sqrt{\bar{y}^2 + z^2} = \delta F(\bar{x}), \quad F(1) = 1$$

and the coordinates

$$\bar{x} = \bar{x}, \quad \bar{r} = (1/\lambda)[(\bar{r}/\delta) - F(\bar{x})]$$

The small parameters are $\delta$ and $\lambda = (\gamma - 1)/(\gamma + 1)$. Subscript zero refers to the perturbations at zero incidence and subscript one to angle of attack. For angle of attack, linear equations are obtained with variable coefficients depending on the zero incidence solution.

Two first integrals of these equations can be found and the pressure on the body determined. As in the case of zero incidence, the surface pressure is independent of the shock shape or $N$. The results are

$$dC_L/d\alpha = (4/3)\{1 + F'(1)\int_0^1 F(x)dx\}$$

$$x_{c.p.} = 1 - \left[(4/3)\int_0^1 F(x)dx \Big/ (dC_L/d\alpha)\right]$$

Details of the calculation are presented in reference 2.

### REFERENCES

[1] Cole, J. D., *Newtonian Flow Theory for Slender Bodies*, Journal of the Aeronautical Sciences, Vol. 24, No. 6, pp. 448–455, June, 1957.
[2] Cole, J. D., *Lift of Slender Nose Shapes According to Newtonian Theory*, The RAND Corporation, Paper P-1270, February 4, 1958.

## On the Reduction of Maximum Loads in Nonlinear Viscoelastic Columns*

Harry H. Hilton
Professor of Aeronautical Engineering, University of Illinois, Urbana, Ill., and Consultant, Hughes Aircraft Company, Culver City, Calif.
February 24, 1958

THE PROBLEM of creep buckling of linear and nonlinear viscoelastic columns has been treated extensively in the literature.[1–4] Kempner and Pohle[2] have shown that a linear viscoelastic column will not creep buckle in a finite time, and other writers[4, 5] have proposed additional creep-buckling criteria in order to overcome this difficulty. Nonlinear viscoelasticity, on the other hand, has been believed to be free of the inability to predict finite creep-buckling times.[1, 3]

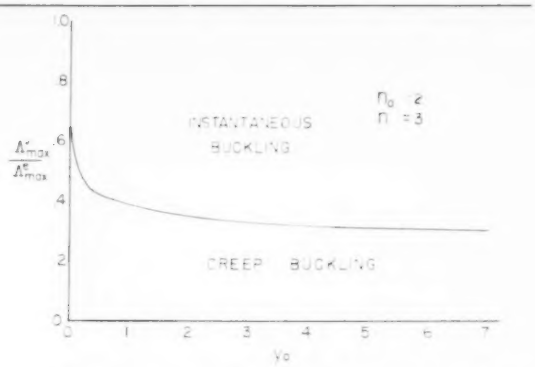


FIG. 1. Reduction of maximum load with amplitude of initial curvature.

However, two interesting phenomena associated with nonlinear creep buckling have escaped attention so far and are the subjects of this paper—i.e., the reduction of the maximum nonlinear viscoelastic load as compared to the maximum load of an equivalent elastic column, and the nonoccurrence of finite buckling time under some conditions. The author[6] has already noted a reduction of the maximum viscoelastic Mach Number over the corresponding elastic and the partial nonexistence of finite divergence times in the nonlinear creep divergence problem, which basically is similar to creep buckling.

The present analysis will be restricted to Odqvist's[3] results since for the purposes of this paper they can be handled in a simpler fashion than those of Hoff[1] and his coworkers, although a similar discussion is applicable to the latter works. Odqvist considers an I-section column obeying a stress-strain relation

$$d\epsilon/dt = k_0\sigma^{n_0-1}(d\sigma/dt) + k\sigma^n \tag{1}$$

Equilibrium of forces and moments and the assumption that the lateral deflection is in the form $w = a(t)\sin\xi$ plus the use of collocation method yields

$$[1 - \Lambda(1 + a)^{n_0-1}](da/dt) + \Pi[(1 - a)^n - (1 + a)^n] = 0 \tag{2}$$

where $\Lambda$ and $\Pi$ are parameters depending upon the load, material properties, and geometry of the column.[3]

While this last equation cannot be readily integrated for arbitrary values of the exponents, certain observations are pertinent. The integration of Eq. (2) leads to a relation between the time $t$ and the amplitude $a$. If one defines the time corresponding to creep buckling as the value of $t$ when $a(t_{cr}) \to \infty$, then for finite creep buckling times the values of the exponents must be limited to

$$n > 2, \quad n_0 < n \tag{3}$$

A closer examination of the case $n_0 = 2$ and $n = 3$ will reveal an additional restriction. In this instance, the creep buckling time will be

$$(3\Pi/2)t_{cr} = [(1 - \Lambda)/8]\ln[(4 + a_0^2)/a_0^2] - (4\Lambda/3\pi)\tan^{-1}(2/a_0) \tag{4}$$

where $a_0$ is the initial amplitude of the deflection of an equivalent elastic column obeying the stress-strain relation

$$\epsilon = (k_0/n_0)\sigma^{n_0} \tag{5}$$

and having an initial curvature

$$w_0 = y_0\sin\xi \tag{6}$$

Following the same procedure as was used in obtaining Eq. (2),

* The analysis described in this paper was performed under the sponsorship of the Systems Development Laboratories, Hughes Aircraft Company, and the author is grateful to them for permission to publish this article.

one finds that for the elastic column

$$(\Lambda/n_0)\,[(1 - a_0)^{n_0} - (1 + a_0)^{n_0}] = y_0 - a_0 \qquad (7)$$

For the present case, $n_0 = 2$, Eq. (7) yields

$$a_0 = y_0/(1 - 2\Lambda), \quad \Lambda = 2k(L/\pi n)^2\,(P/A)^n \qquad (8)$$

It is apparent that the maximum or critical value of the elastic load is achieved when

$$\Lambda^c{}_{max} = 1/2 \quad (n_0 = 2) \qquad (9)$$

Since this elastic case forms the initial conditions for the viscoelastic problem, $\Lambda$ in Eq. (4) must be less than 1/2, otherwise instantaneous elastic buckling would take place. A meaningful physical $t_{cr}$ must obviously be positive which implies that

$$\Lambda^c{}_{max} = \left(1 + \tfrac{1}{3}2 \tan^{-1}(2/a_0)/3\pi \ln[(4 + a_0^2)/a_0^2]\right)^{-1} \qquad (10)$$

Fig. 1 has been computed using Eqs. (8) to (10) and illustrates the reduction in maximum load for a viscoelastic column of this type.

A similar analysis for the cases $n = 3$ and $n_0 = 0$ and 1, respectively, reveals no reduction in maximum viscoelastic loads. Hoff[7] has shown that the elastic term in the stress-strain relation (1) seems of little importance in creep analysis and can be neglected ($k_0 = 0$) after a moderately large amount of creep has taken place. However, it would appear that initial elasticity strongly affects stability considerations—i.e., the reduction of the maximum load.

The present analysis further indicates that the mere use of a nonlinear viscoelastic stress-strain law, such as Eq. (1), gives no a priori guarantee that a finite creep buckling time can be achieved. Unless the inequalities (3) are satisfied, this particular stress-strain law will not be of any more value than linear viscoelasticity. It is difficult to say, at this point, whether or not other more nonlinear viscoelastic laws possess similar restrictions, because, in general, closed-form solutions such as Eq. (4) cannot be obtained. However, it must be remembered that when use is made of Eq. (1), the constants, $k$, $k_0$, $n$, and $n_0$ are determined by fitting this equation to experimental data. Such approximations might introduce restrictions into the problem because of the aforementioned properties of the stress-strain law rather than because of inherent characteristics of the physical problem.

### References*


[1] Hoff, N. J., *Buckling and Stability*, 41st Wilbur Wright Memorial Lecture, Royal Aero. Soc. Reprint No. 123, January, 1954.

[2] Kempner, J., and Pohle, V., *On the Nonexistence of a Finite Critical Time for Linear Viscoelastic Columns*, Journal of the Aeronautical Sciences, Vol. 20, No. 8, pp. 572, 573, August, 1953.

[3] Odqvist, F. K. G., *Influence of Primary Creep on Column Buckling*, J. Appl. Mech., Vol. 21, p. 295, September, 1954.

[4] Hilton, H. H., *Creep Collapse of Viscoelastic Columns with Initial Curvatures*, Journal of the Aeronautical Sciences, Vol. 19, No. 12, pp. 844–846, December, 1952.

[5] Gerard, G., *A Creep Buckling Hypothesis*, Journal of the Aeronautical Sciences, Vol. 23, No. 9, pp. 879–882, 887, September, 1956.

[6] Hilton, H. H., *Pitching Instability of Rigid Lifting Surfaces on Viscoelastic Supports in Subsonic or Supersonic Potential Flow*, Hughes Aircraft Co. Technical Report SRSM7-194, January, 1957, and Proc. Third Midwestern Conf. on Appl. Mech., pp. 1–19, 1957.

[7] Hoff, N. J., *Approximate Analysis of Structures in the presence of Moderately Large Creep Deformations*, Quart. of Appl. Math., Vol. 12, No. 1, p. 49, April, 1954.


* The reader is referred to reference 1 for a comprehensive bibliography.

## On Heat Transfer in Slip Flow


Stephen H. Maslen
*Lewis Flight Propulsion Laboratory, NACA, Cleveland, Ohio*

February 24, 1958

A NUMBER OF AUTHORS have considered the effect of slip on the heat transfer and skin friction in a laminar boundary layer over a flat plate. Reference 1 considers this by a perturbation on the usual laminar boundary-layer analysis while some other studies—e.g., reference 2—have proceeded through consideration of the Rayleigh problem of the impulsive motion of an infinite plate.

In all these cases, there appears to be an error in the calculation of the heat transfer to the wall. When there is slip, this transfer has two parts. One is the usual contribution due to conduction ($kT_y$) while there is a second part due to "sliding friction" ($\mu u u_y$). This term, heretofore omitted, represents the work done directly on the wall by the shear. This latter term is nonzero only if there is some slip at the wall. Then the heat transfer, $q$, into the wall is

$$q = (kT_y + \mu u u_y)_{y=0} \qquad (1)$$

In reference 1, a solution is given for the slip flow over a flat plate. The solution can be found in closed form for almost any condition of the gas provided only that the corresponding continuum solution is known. For a perfect gas having constant specific heats but whose viscosity and conductivity are arbitrary functions of temperature, the velocity and temperature profiles are given by

$$\left.\begin{aligned} u/u_\infty &= u_0(\eta) - \epsilon_x\left\{u_{0\eta}\left[A + \int_0^\eta f(\eta)d\eta\right]\right\} \\ T/T_\infty &= T_0(\eta) - \epsilon_x\left\{T_{0\eta}\left[A + \int_0^\eta f(\eta)d\eta\right] - F(\eta)\right\} \end{aligned}\right\} \qquad (2)$$

where

$$\eta = (y/\sqrt{x})\,\sqrt{\mu_\infty \rho_\infty}/\rho_\infty$$

$$f(\eta) = [(\eta - b)/\mu_0 u_{0\eta}] + (d\mu_0/dT_0)\,[F(\eta)/\mu_0]$$

$$F(\eta) = (\mu_0/k_0)e^{Pr\int_0^\eta [(\mu_0 u_{0\eta})_\eta d\eta/k_0 u_{0\eta}]}\left\{B + \int_0^\eta [(\eta - b)/\mu_0] \times [(\gamma - 1)M^2 Pr\, u_0 + (k_0 T_{0\eta}/\mu_0 u_{0\eta})]e^{-Pr\int_0^\eta [(\mu_0 u_{0\eta})_\eta d\eta/k_0 u_{0\eta}]} d\eta\right\} \qquad (3)$$

and where, for supersonic flow

$$\epsilon_x = (\delta^*/x)/4\sqrt{M^2 - 1}$$

$$A = -\left[4M\sqrt{\gamma(M^2 - 1)}/b\right](\mu_0 a_1 \sqrt{T_0})_{\eta=0}$$

$$b = \sqrt{Re_x}(\delta^*/x)$$

In these expressions $\delta^*$ is the continuum displacement thickness, and $a_1$ is related to the reflection coefficient, $\bar{a}$, by $a_1 = \sqrt{\pi/2}\,[(2 - \bar{a})/\bar{a})]$. $M$, $\gamma$, $Pr$, and $Re_x$ have their usual definitions in terms of free-stream conditions and distance along the plate.

In these equations, all the required boundary conditions have been satisfied except that on the wall temperature or heat transfer. Thus, the coefficient $B$ of Eq. (3) is undetermined. Regarding conditions far from the plate, the displacement effect of the boundary layer on the external stream has been allowed for and the profiles given go exponentially to the required limit for all values of $B$.

From these expressions, the wall values of most interest can be found. The temperature, shear, and Nusselt Number are, using Eq. (1),

$$T_w/T_\infty = T_0 + \epsilon_x\left\{(\mu_0 B/k_0) + 4M\sqrt{\gamma(M^2 - 1)} \times [\mu_0(a_1 - c_1)\sqrt{T_0}/b]\; T_{0\eta}\right\}_{\eta=0} \qquad (4)$$

$$\left.\begin{aligned} C_f\sqrt{Re_x} &= [(\mu u_y)_{y=0}\sqrt{Re_x}/(1/2)\rho_\infty u_\infty{}^2] = \\ &\quad 2\mu_0 u_{0\eta} + \epsilon_x\left[2\sqrt{Re_x}\,(\delta^*/x)\right] \\ Nu_x/\sqrt{Re_x} &= x(kT_y + \mu u u_y)_{y=0}/k_\infty(T_a - T_w)\sqrt{Re_x} = \\ &\quad [T_\infty/(T_a - T_w)]\,[k_0 T_{0\eta} + \epsilon_x(0)]_{\eta=0} \end{aligned}\right\} \qquad (5)$$

$T_a$ is the continuum value of the adiabatic wall temperature, and $c_1$ is related to the accommodation coefficient, $c$, by

$$c_1 = [2/(\gamma + 1)]\,\sqrt{\pi/2}[(2 - \bar{c})/Pr\bar{c}]$$

These relations follow from Eqs. (2) and (3). However, Eqs. (5) can be shown to be much more generally valid, requiring neither equilibrium nor any particular assumption regarding the state equation or the transport properties. It has, however, been assumed that the external stream is a perfect gas and that external forces and diffusion and radiation effects do not occur.

Several results are at once apparent from Eqs. (4) and (5). If the thermal boundary condition specifies the wall temperature, then $B$ is determined and the solution is completely defined. On the other hand, if the condition is one on the heat transfer, then $B$ cannot be found. Fortunately, however, this uncertainty affects neither the shear nor the heat transfer. As was pointed out before, no condition far from the plate is of use because the effect of this term decays exponentially in the usual manner for large distances. In this connection it might be observed that, for an insulated plate and a constant $Pr$ of unity, $F(\eta)$ in Eq. (3) becomes simply

$$F(\eta) = B\mu_0 u_{0\eta}/(\mu_0 u_{0\eta})_{\eta=0}$$

To the extent that this term is nonzero, the temperature distribution differs from the familiar exact integral of the energy equation—namely,

$$T/T_\infty = 1 + [(\gamma - 1)/2]M^2(1 - u^2/u_\infty{}^2)$$

This ambiguity is not related to the slip phenomenon but really occurs in the continuum hypersonic analyses (reference 3, for example) although the author apparently did not notice it. Stewartson[4] found a similar effect arising in terms of the next order higher than considered in the present study. He examined only the momentum equation after reducing it to the incompressible case by the familiar Howarth transformation. However, it is seen here that compressibility effects introduced by the energy equation cause the trouble to arise even sooner. It appears that some upstream condition is required in order to choose the appropriate value for $B$ if a heat-transfer boundary condition is used. In any case, there is no effect on the shear and heat transfer although, for example, the recovery factor cannot be found.

The slip effect (which vanishes if $a_1$ and $c_1$ are set equal to zero) does not influence either the shear or the heat transfer to this order. (However this conclusion holds only for the flat-plate case.) The shear is increased over its continuum value. This effect has nothing to do with slip but is caused by the external pressure gradient induced by the boundary layer. The heat transfer is unchanged from the continuum value. The heat flow due to the sliding friction exactly compensates for the reduced conduction to the wall.

### References


[1] Maslen, S. H., *Second Approximation to the Laminar Compressible Boundary in Slip Flow*, NACA TN 2818, November, 1952.

[2] Martino, R. L., *Heat Transfer in Slip Flow*, UTIA Report No. 35, University of Toronto, October, 1955.

[3] Kuo, Y. H., *Viscous Flow Along a Flat Plate Moving at High Supersonic Speeds*, Journal of the Aeronautical Sciences, Vol. 23, No. 2, pp. 125–136, February, 1956.

[4] Stewartson, K., *On Asymptotic Expansions in the Theory of Boundary Layers*, J. Math. & Phys., Vol. 36, No. 3, pp. 173–191, October, 1957.


## An Approximate Method for Determining the Wave Drag of Axisymmetric Conical Cowls


John W. Brook

*Research Department, Grumman Aircraft Engineering Corporation, Bethpage, N.Y.*


February 27, 1958

It is assumed that the stream tube captured by the cowl is cylindrical and that the flow is uniform and steady. Therefore, at the cowl lip, the flow is taken to be two dimensional while conical flow will be reached asymptotically as the cowl length increases indefinitely. Thus

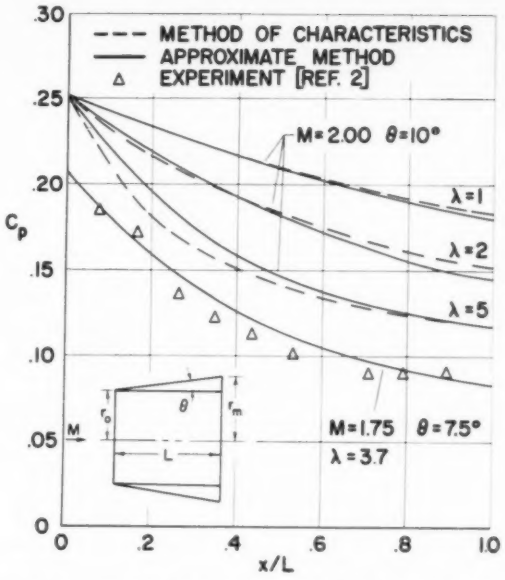


FIG. 1. Comparison between pressure distributions obtained from characteristics, experiment, and approximate method.

$$C_{p_{x=0}} = C_{p_{2D}}, \quad C_{p_{x\to\infty}} = C_{p_c} \tag{1}$$

where $C_{p_{2D}}$ is the two-dimensional pressure coefficient and $C_{p_c}$ the conical pressure coefficient for the cowl angle. In order to satisfy Eqs. (1) the pressure distribution on the cowl surface is assumed to be of the form

$$C_p = A - Be^{-a(x/r_0)} \tag{2}$$

where $a$ is a free constant and $r_0$ is the cowl radius at the lip. Then, from Eqs. (1)

$$C_p = C_{p_c} - [C_{p_c} - C_{p_{2D}}]e^{-a(x/r_0)} \tag{3}$$

Setting $x' = x/L$, $\Delta = C_{p_c} - C_{p_{2D}}$, and $\lambda = L/r_0$, one obtains

$$C_p = C_{p_c} - \Delta e^{-a\lambda x'} \tag{4}$$

The constant $a$ may be determined by differentiating Eq. (4) with respect to $x'$, resulting in

$$d\,C_p/dx' = a\lambda\Delta e^{-a\lambda x'} \tag{5}$$

If this derivative is evaluated at $x' = 0$, the following result is obtained:

$$a = [dC_p/dx']_{x'=0}/\Delta\lambda \tag{6}$$

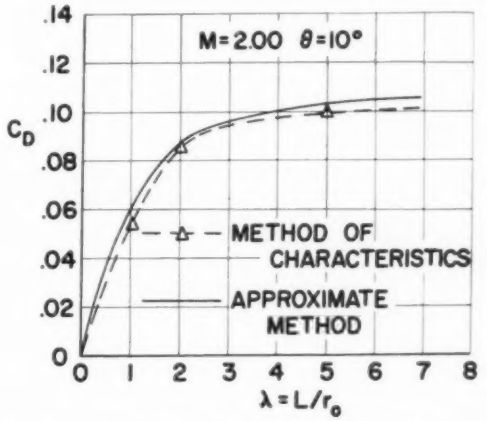


FIG. 2. Comparison of wave drags obtained by characteristics and approximate method.

In order to determine this constant, it is only necessary to determine the derivative $[dC_p/dx']_{x'=0}$ since $\lambda$ depends on the geometry and $\Delta$ may be found readily. This derivative can be evaluated by using a simple three-point method-of-characteristics solution.[1] The value of the derivative will be a function of the mesh size of the characteristic net, but it has been found that it does not vary appreciably if small mesh sizes are used.[1]

Therefore, it is seen that the determination of the pressure distribution on the cowl has been reduced from a lengthy characteristics solution to one involving only three points. Furthermore, the constant $a$ may be initially computed for several families of cowls and presented in chart form, thereby allowing specific configurations to be calculated rapidly and easily.[1]

By integrating the known pressure distribution over the cowl surface, the wave-drag coefficient may be obtained. In cylindrical coordinates, the equations of the cowl are:

$$r = r_0 + \delta x, \quad dr = \delta dx \tag{7}$$

Here, $\delta = \tan\theta$, where $\theta$ is the cowl angle. For a body of revolution, the drag coefficient may be written

$$C_D = (2/r_m^2)\int_{r_0}^{r_m} C_p r\, dr \tag{8}$$

based on maximum frontal area $= \pi r_m^2$. Thus, substituting Eqs. (4) and (7) into Eq. (8)

$$C_D = (2/r_m^2)\int_0^L [C_{p_c} - \Delta e^{-a(x/r_0)}][r_0 + \delta x|\delta dx \tag{9}$$

Integrating and employing the notation $\lambda = L/r_0$

$$C_D = [2\delta/(1+\delta\lambda)^2]\{\lambda C_{p_c} + (1/2)\delta\lambda^2 C_{p_c} - (\Delta/a)[1 - e^{-a\lambda}] + (\Delta\delta/a^2)[e^{-a\lambda}(1 + a\lambda) - 1]\} \tag{10}$$

This equation is valid for all values of $\lambda$ between 0 and $\infty$, and it can be shown to be valid at the two limits.[1] Some values of $C_D$ have been plotted in reference (1) for various values of $\theta$, $M$, and $\lambda$.

The present method has been compared to the complete method-of-characteristics solution for $M = 2.00$, $\theta = 10°$, and $\lambda = 1$, 2, and 5. Also, the method has been compared with experimental results obtained in Convair's Daingerfield, Texas, wind tunnel.[2] In both cases the agreement is good. Fig. (1) compares the pressure distributions obtained using the approximate method with those from the method of characteristics and the experimental values. Fig. (2) compares the wave-drag variation obtained using the present method with that obtained from the method of characteristics.

### References

[1] Brook, John W., *A Rapid Method for the Determination of the Pressure Distribution and Wave Drag of Conical Inlet Cowls of Circular Cross Section*, Grumman Aircraft Engineering Corp., Research Dept. Report RE-91, January, 1958.

[2] *Tests on the Series C Ducted Body Pressure Model for Johns Hopkins University*; Convair Aircraft Corp., CVAC-858, January, 1948.

## The Determination of the Shear Center for a Special Solid Symmetrical Airfoil

Alphonse J. Sistino
*Analytical Engineer, Fairchild Engine Division, Fairchild Engine and Aircraft Corporation, Deer Park, N.Y.*

March 12, 1958

### Symbols

$x, y, z$ = Cartesian coordinates as shown in Fig. 1
$P$ = a force in the $xy$ plane and parallel to the $x$ axis
$\tau_{xz}$ = shear stress on the $xy$ plane with the force in the $x$ direction
$\tau_{yz}$ = shear stress on the $xy$ plane with the force in the $y$ direction
$\varphi$ = St. Venant stress function
$I$ = area moment of inertia about the $y$ axis
$\nu$ = Poisson's ratio

In the study of the deflections of a solid airfoil cantilever beam (such as a compressor or turbine blade) the location of the shear center plays an important role. In general, the shear centers for symmetrical solid airfoils are not readily available due to the difficulty of finding exact analytical solutions to Eq. (5) (see below). In this paper a special symmetrical solid airfoil has been chosen such that Eq. (5) will have an exact analytical solution. This result may serve to check approximate methods for obtaining shear centers of airfoils. In Fig. 1 the special airfoil and its shear center is plotted.

The shear center is defined by the following equation:

$$d = |M_z|/P \tag{1}$$

Where $$M_z = \int\int (\tau_{xz}y - \tau_{yz}x)\, dxdy$$

For a concentrated loaded cantilever beam, the equilibrium equation leads to the following shear-stress distribution:[1]

$$\tau_{xz} = (\partial\varphi/\partial y) - (Px^2/2I) + f(y) \tag{2}$$

$$\tau_{yz} = -(\partial\varphi/\partial x) \tag{3}$$

where $f(y)$ is a function such that

$$(Px^2/2I) - f(y) = 0 \tag{4}$$

at the boundary of the cross section.[1]

By considering the compatibility equation, the following equation is derived:[1]

$$(\partial^2\varphi/\partial x^2) + (\partial^2\varphi/\partial y^2) = [\nu/(1+\nu)](Py/I) - (df/dy) \tag{5}$$

Now if an airfoil section is chosen whose boundary curve is given by

$$x = \pm h\sqrt{y(1-y)}$$

then, by Eq. (4)

$$f(y) = (Ph^2/2I)y(1-y)^2 \tag{6}$$

where $h$ is an arbitrary constant to be determined by additional conditions.

By substitution of Eq. (6) into Eq. (5), Eq. (5) becomes

$$(\partial^2\varphi/\partial x^2) + (\partial^2\varphi/\partial y^2) = [\nu/(1+\nu)](Py/I) - (Ph^2/2I)\{1 - 4y + 3y^2\} \tag{7}$$

Now since $\varphi$ must vanish at the boundary[1] and must satisfy Eq. (7), the following function is assumed:

$$\varphi = \{x^2 - h^2y(1-y)\}(sy + r) \tag{8}$$

where $h$, $s$, and $r$ are constants.

In substituting the assumed $\varphi$ function into Eq. (7) the constants $h$, $s$, and $r$ are so adjusted as to satisfy Eq. (7). For $\nu = 0.3$ the following values satisfy Eq. (7):

$h = 0.202$
$s = 0.125\,(P/I)$
$r = -0.0045\,(P/I)$

Having now completely defined $f(y)$ and $\varphi(x, y)$, $\tau_{xz}$ and $\tau_{yz}$

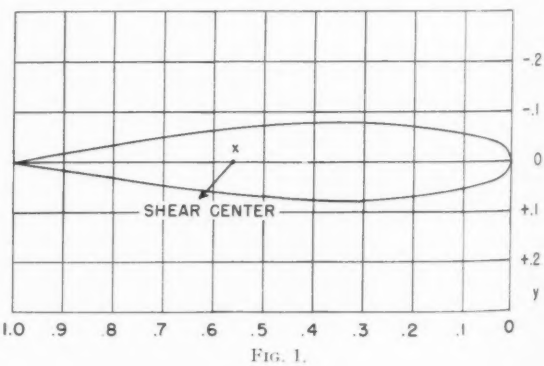


Fig. 1.

are determined by Eqs. (2) and (3), and the results are substituted into Eq. (1). For $h = 0.202$, $d = 0.561$. In Fig. 1 the airfoil cross section is plotted and its shear center noted.

### Reference

(1) Timoshenko, S. and Goodier, J. N., *Theory of Elasticity*, 2nd. Ed., Chap. 12, McGraw-Hill Book Co., Inc., New York, 1951.

## Fundamental Solutions for Heat Transfer From Nonisothermal Flat Plates

Donald C. Baxter and William C. Reynolds
*National Research Council of Canada, Ottawa, and Stanford University, Stanford, Calif., Respectively*

March 3, 1958

In recent years there has been considerable interest in the influence that the temperature distribution along a heated surface has upon the convective heat-transfer coefficient.[3] Of particular interest is the case of the flat plate; for incompressible flow, both the laminar and turbulent variable-wall-temperature problems have been treated approximately by integral methods, and the results of these analyses may be expressed concisely. The laminar analysis has been substantiated by comparison with numerical calculation,[1] and the turbulent analysis has been thoroughly verified experimentally.[2] The purpose of this note is to summarize the results of the analyses and to present certain special fundamental examples which illustrate the effects.

Table 2
Incomplete Beta Function Ratios $I_z(\alpha, \beta)$

| z | $\alpha=1/3$ $\beta=2/3$ | $\alpha=1/3$ $\beta=3/3$ | $\alpha=1/3$ $\beta=4/3$ | $\alpha=2/3$ $\beta=3/3$ | $\alpha=2/3$ $\beta=4/3$ | $\alpha=2/3$ $\beta=5/3$ | $\alpha=3/3$ $\beta=4/3$ | $\alpha=3/3$ $\beta=5/3$ |
|---|---|---|---|---|---|---|---|---|
| 0 | 0 | 0 | 0 | 0 | 0 | 0 | 0 | 0 |
| .020 | .1094 | .2065 | .4007 | .0211 | .0346 | .0588 | .0421 | .0711 |
| .040 | .1558 | .2919 | .5007 | .0422 | .0656 | .1113 | .0841 | .1391 |
| .060 | .1909 | .3574 | .5804 | .0633 | .0948 | .1597 | .1261 | .2047 |
| .080 | .2204 | .4130 | .6496 | .0843 | .1227 | .2057 | .1680 | .2681 |
| .100 | .2464 | .4619 | .7109 | .1053 | .1496 | .2500 | .2098 | .3295 |
| .120 | .2697 | .5058 | .7663 | .1262 | .1757 | .2929 | .2516 | .3891 |
| .140 | .2911 | .5458 | .8171 | .1471 | .2012 | .3347 | .2933 | .4469 |
| .160 | .3110 | .5827 | .8641 | .1679 | .2262 | .3756 | .3350 | .5030 |
| .180 | .3298 | .6171 | .9079 | .1888 | .2508 | .4158 | .3767 | .5575 |
| .200 | .3476 | .6494 | .9490 | .2096 | .2751 | .4553 | .4183 | .6104 |
| .220 | .3647 | .6799 | .9877 | .2304 | .2991 | .4943 | .4599 | .6619 |
| .240 | .3811 | .7088 | 1.0243 | .2512 | .3230 | .5328 | .5015 | .7120 |
| .260 | .3970 | .7363 | 1.0590 | .2720 | .3467 | .5709 | .5431 | .7608 |
| .280 | .4125 | .7626 | 1.0920 | .2928 | .3703 | .6086 | .5847 | .8084 |
| .300 | .4276 | .7878 | 1.1234 | .3136 | .3939 | .6461 | .6263 | .8548 |
| .320 | .4424 | .8120 | 1.1534 | .3344 | .4175 | .6833 | .6679 | .9002 |
| .340 | .4570 | .8354 | 1.1821 | .3552 | .4411 | .7203 | .7095 | .9446 |
| .360 | .4714 | .8580 | 1.2096 | .3760 | .4648 | .7572 | .7511 | .9881 |
| .380 | .4857 | .8799 | 1.2361 | .3968 | .4886 | .7940 | .7927 | 1.0307 |
| .400 | .5000 | .9012 | 1.2616 | .4176 | .5125 | .8308 | .8343 | 1.0725 |
| .420 | .5143 | .9220 | 1.2863 | .4384 | .5366 | .8676 | .8759 | 1.1135 |
| .440 | .5286 | .9423 | 1.3102 | .4592 | .5609 | .9045 | .9175 | 1.1538 |
| .460 | .5430 | .9622 | 1.3334 | .4800 | .5854 | .9415 | .9591 | 1.1934 |
| .480 | .5574 | .9817 | 1.3560 | .5008 | .6102 | .9787 | 1.0007 | 1.2324 |
| .500 | .5720 | 1.0008 | 1.3780 | .5216 | .6353 | 1.0160 | 1.0423 | 1.2708 |
| .520 | .5867 | 1.0196 | 1.3995 | .5424 | .6608 | 1.0536 | 1.0839 | 1.3087 |
| .540 | .6016 | 1.0381 | 1.4205 | .5632 | .6867 | 1.0915 | 1.1255 | 1.3461 |
| .560 | .6167 | 1.0563 | 1.4411 | .5840 | .7131 | 1.1297 | 1.1671 | 1.3830 |
| .580 | .6321 | 1.0743 | 1.4613 | .6048 | .7400 | 1.1683 | 1.2087 | 1.4195 |
| .600 | .6477 | 1.0921 | 1.4812 | .6256 | .7675 | 1.2073 | 1.2503 | 1.4556 |
| .620 | .6636 | 1.1097 | 1.5008 | .6464 | .7957 | 1.2468 | 1.2919 | 1.4913 |
| .640 | .6799 | 1.1272 | 1.5202 | .6672 | .8246 | 1.2869 | 1.3335 | 1.5267 |
| .660 | .6966 | 1.1446 | 1.5394 | .6880 | .8544 | 1.3277 | 1.3751 | 1.5618 |
| .680 | .7138 | 1.1619 | 1.5585 | .7088 | .8852 | 1.3693 | 1.4167 | 1.5966 |
| .700 | .7316 | 1.1792 | 1.5775 | .7296 | .9172 | 1.4119 | 1.4583 | 1.6312 |
| .720 | .7501 | 1.1965 | 1.5964 | .7504 | .9505 | 1.4557 | 1.4999 | 1.6656 |
| .740 | .7694 | 1.2139 | 1.6153 | .7712 | .9854 | 1.5009 | 1.5415 | 1.6999 |
| .760 | .7897 | 1.2314 | 1.6343 | .7920 | 1.0222 | 1.5479 | 1.5831 | 1.7341 |
| .780 | .8112 | 1.2491 | 1.6534 | .8128 | 1.0612 | 1.5971 | 1.6247 | 1.7683 |
| .800 | .8342 | 1.2671 | 1.6726 | .8336 | 1.1030 | 1.6490 | 1.6663 | 1.8025 |
| .820 | .8592 | 1.2855 | 1.6921 | .8544 | 1.1482 | 1.7044 | 1.7079 | 1.8368 |
| .840 | .8866 | 1.3045 | 1.7120 | .8752 | 1.1977 | 1.7643 | 1.7495 | 1.8712 |
| .860 | .9172 | 1.3243 | 1.7325 | .8960 | 1.2527 | 1.8302 | 1.7911 | 1.9059 |
| .880 | .9520 | 1.3452 | 1.7539 | .9168 | 1.3147 | 1.9041 | 1.8327 | 1.9410 |
| .900 | .9926 | 1.3677 | 1.7766 | .9376 | 1.3860 | 1.9888 | 1.8743 | 1.9768 |
| .920 | 1.0417 | 1.3928 | 1.8013 | .9584 | 1.4702 | 2.0894 | 1.9159 | 2.0136 |
| .940 | 1.1048 | 1.4222 | 1.8291 | .9792 | 1.5750 | 2.2150 | 1.9575 | 2.0519 |
| .960 | 1.1940 | 1.4595 | 1.8624 | .9900 | 1.6375 | 2.2900 | 1.9783 | 2.0717 |
| .980 | 1.3477 | 1.5199 | 1.9161 | .9960 | 1.6722 | 2.3317 | 1.9887 | 2.0819 |
| 1.000 | 1.0000 | 1.0000 | 1.0000 | 1.0000 | 1.0000 | 1.0000 | 1.0000 | 1.0000 |
| $B_z(\alpha,\beta)$ | 1.4677 | 1.5499 | 2.0155 | 1.4694 | 2.1963 | 3.0459 | 2.4019 | 3.4006 |

These fundamental solutions involve the *step* and *ramp* distributions defined by Table 1. These solutions are also useful as building blocks either in predicting the heat flux $q''$ B.t.u./hour ft.$^2$ where the wall temperature $T_w$°F. is prescribed or in predicting the wall temperature when the heat flux is given. In addition, certain integrals which appear repeatedly in these problems are tabulated.

For problems of specified wall temperature, the heat-transfer rate may be written as

$$q''(x) = \rho U c_p St_{\bar{T}} F_T(x)$$

while for cases of specified heat flux the wall temperature is given by

$$T_w(x) - T_e = F_q(x)/(\rho U c_p St_{\bar{T}})$$

Here $T_e$ denotes the free-stream temperature; $St_{\bar{T}}$ represents the Stanton number for *constant wall temperature*, and can be thought of as simply an abbreviation:

*for laminar flow* $St_{\bar{T}} = 0.332\, Pr^{-2/3} Re_x^{-1/2}$

Table 1
Table of Fundamental Solutions

| | LAMINAR FLOW<br>$St_{\bar{T}} = 0.332\ Pr^{-2/3}\ Re_x^{-1/2}$<br>$r = 1 - (a/x)^{3/4}$ | TURBULENT FLOW<br>$St_{\bar{T}} = 0.0296\ Pr^{-0.4}\ Re_x^{-0.2}$<br>$s = 1 - (a/x)^{3/10}$ |
|---|---|---|
| Specified Temperature | Wall Temperature Function, $F_T(x)$, °F | |
| Arbitrary Temperature | $\int_0^x [1 - (\xi/x)^{3/4}]^{-1/3}\, dT_w(\xi)$ | $\int_0^x [1 - (\xi/x)^{9/10}]^{-1/9}\, dT_w(\xi)$ |
| Constant Temperature | b | b |
| Step Temperature | $0 \quad x<a$<br>$b(r)^{-1/3} \quad x>a$ | $0 \quad x<a$<br>$b(s)^{-1/9} \quad x>a$ |
| Ramp Temperature | $0 \quad x<a$<br>$1.612\ mx\ I_r(2/3,4/3) \quad x>a$ | $0 \quad x<a$<br>$1.134\ mx\ I_s(8/9,10/9) \quad x>a$ |
| Specified Heat Flux | Heat Flux Function, $F_q(x)$, Btu/hrft$^2$ | |
| Arbitrary Heat Flux | $(0.207/x) \int_0^x [1 - (\xi/x)^{3/4}]^{-2/3}\, q(\xi)\, d\xi$ | $(0.0975/x) \int_0^x [1 - (\xi/x)^{9/10}]^{-8/9}\, q(\xi)\, d\xi$ |
| Constant Heat Flux | 0.730 c | 0.959 c |
| Step Heat Flux | $0 \quad x<a$<br>$0.730\ c\ I_r(1/3,4/3) \quad x>a$ | $0 \quad x<a$<br>$0.959\ c\ I_s(1/9,10/9) \quad x>a$ |
| Ramp Heat Flux | $0 \quad x<a$<br>$0.555\ n[\ xI_r(1/3,8/3) - 1.316\ aI_r(1/3,4/3)\ ] \quad x>a$ | $0 \quad x<a$<br>$0.865\ n[\ xI_s(1/9,20/9) - 1.108\ aI_s(1/9,10/9)\ ] \quad x>a$ |

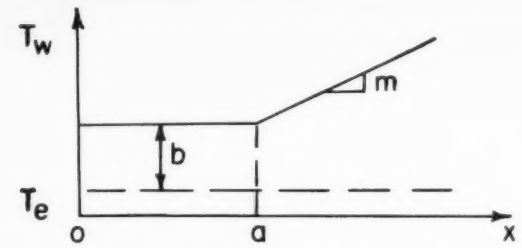


FIG. 1. A wall temperature distribution.

TABLE 3

| Characteristic | Laminar, $StPr^{2/3}Re_x^{1/2}$ | Turbulent, $StPr^{0.4}Re_x^{0.2}$ |
|---|---|---|
| Constant temperature | 0.332 | 0.0296 |
| Ramp temperature from leading edge | 0.535 | 0.0336 |
| Constant heat flux | 0.455 | 0.0309 |
| Ramp heat flux from leading edge | 0.598 | 0.0342 |

*for turbulent flow*

$$St_{\bar{T}} = 0.0296\ Pr^{-0.4}Re_x^{-0.2}$$

Here $Pr$ denotes the Prandtl Number, $Pr = \mu c_p/k$, and $Re_x$ the local Reynolds Number based on distance from the leading edge, $Re_x = \rho Ux/\mu$. $F_T(x)$ and $F_q(x)$ are the wall-temperature and heat-flux functions which describe the nonisothermal influence, values of which are given by Table 1.

The solutions in Table 1 are written in terms of *ratios of incomplete beta function* defined by

$$I_z(\alpha, \beta) = B_z(\alpha, \beta)/B_1(\alpha, \beta)$$

where the *incomplete* beta function is defined as

$$B_z(\alpha, \beta) = \int_0^z \sigma^{\alpha-1}(1-\sigma)^{\beta-1}d\sigma$$

The *complete* beta function is related to the gamma function by

$$B_1(\alpha, \beta) = \Gamma(\alpha)\Gamma(\beta)/\Gamma(\alpha+\beta) = B_1(\beta, \alpha)$$

The arguments of the *incomplete* beta function may be shifted using the relation

$$B_z(\alpha, \beta) = B_1(\alpha, \beta) - B_{1-z}(\beta, \alpha)$$

The pertinent functions have been determined numerically and are presented in Table 2.

For the simplest cases the results in Table 3 may be obtained.

Any problem where the wall temperature or heat flux is specified may be handled simply by replacing the given distribution by a succession of steps or ramps, and superimposing the effects of each. This is permissible because the energy equation is *linear*.[3] For example, consider Fig 1. For laminar flow the superposition results in

$$q''(x) = 0.332\ \rho U c_p Pr^{-2/3}Re_x^{-1/2}b, \quad 0 < x < a$$

$$q''(x) = 0.332\ \rho U c_p Pr^{-2/3}Re_x^{-1/2}[b + 1.612\ mxI_r(2/3, 4/3)], \quad x > a$$

Specified heat-flux problems may be treated in a similar manner.

## REFERENCES

[1] Baxter, D. C., and Flügge-Lotz, I., *The Solution of Compressible Laminar Boundary Layer Problems by a Finite Difference Method. Part 2.* Tech. Rep. 110, Div. of Engrg. Mech., Stanford Univ., Stanford, Calif., October 15, 1957. (Prepared under ARDC Contract AF 18(600)-1488.)

[2] Reynolds, W. C., Kays, W. M., and Kline, S. J., *Heat Transfer in the Turbulent Incompressible Boundary Layer with Arbitrary Wall Temperature and Heat Flux*, Final Report, Part III, Contract NAw-6494, Dept. of Mech. Engrg., Stanford Univ., Stanford, Calif., July, 1957.

[3] Tribus, M., and Klein, J., *Forced Convection Through a Laminar Boundary Layer over an Arbitrary Surface with an Arbitrary Temperature Variation*, Journal of the Aeronautical Sciences, Vol. 22, No. 1, pp. 62–64, January, 1955.

# Reduction of Ikenberry-Truesdell Equations to Burnett Equations for Slip Flow†

Hsun-Tiao Yang*
*Institute for Fluid Dynamics and Applied Mathematics, University of Maryland, College Park, Md.*
March 4, 1958

THE PURPOSE of the present note is to establish the exact equivalence of the second iterates of the Ikenberry-Truesdell Equations[1] with the Burnett Equations[2, 3] for slip flow. The second-order expression for the stress tensor given by Eq. (2.18) of reference 1 is

$$P_{ij}^{(2)} = -2\mu E_{ij} + (2\mu/p)(\mu E_{ij})^{\cdot} + (2\mu^2/p)EE_{ij} + (4\mu^2/p)E_k(_iu_j)_{.k} - (4\mu^2/3p)E_{kl}E_{kl}\delta_{ij} + (\mu/\rho\theta)[3(\mu\theta_{,(i})_{,j)} - (\mu\theta_{,k})_{,k}\delta_{ij}] \quad (1)$$

where

$$\left.\begin{aligned} P_{ij} &\equiv p_{ij} - p\delta_{ij} = \text{stress tensor} \\ \mu &= \text{coefficient of dynamic viscosity} \\ p &= \text{hydrostatic pressure} \\ \rho &= \text{density} \\ \theta &= \text{temperature} \\ u_i &= \text{gas velocity vector} \\ E &\equiv u_{k,k} \equiv (\partial u_k/\partial x_k) \\ E_{ij} &\equiv (1/2)(\mu_{i,j} + u_{j,i}) - (1/3)u_{k,k}\delta_{ij} \equiv \overline{\partial u_i/\partial x_j} \\ (^{\cdot}) &\equiv D(\ )/Dt \equiv (\partial/\partial t)(\ ) + (\ )_{,i}u_i \end{aligned}\right\} \quad (2)$$

and a parenthesis around $s$ subscripts indicates a sum over the $s!$ permutations of the indices, divided by $s!$. Thus, Eq. (1) may be rewritten in more familiar notation as

$$P_{ij}^{(2)} = -2\mu\overline{\frac{\partial u_i}{\partial x_j}} + 2\frac{\mu}{p}\frac{D}{Dt}\left(\mu\overline{\frac{\partial u_i}{\partial x_j}}\right) + 2\frac{\mu^2}{p}\overline{\frac{\partial u_k}{\partial x_k}}\overline{\frac{\partial u_i}{\partial x_j}} + 2\frac{\mu^2}{p}\left(\overline{\frac{\partial u_k}{\partial x_i}}\overline{\frac{\partial u_j}{\partial x_k}} + \overline{\frac{\partial u_k}{\partial x_j}}\overline{\frac{\partial u_i}{\partial x_k}}\right) - \frac{4\mu^2}{3p}\overline{\frac{\partial u_k}{\partial x_l}}\overline{\frac{\partial u_k}{\partial x_l}}\delta_{ij} + 3\frac{\mu}{\rho\theta}\overline{\frac{\partial}{\partial x_i}\left(\mu\frac{\partial\theta}{\partial x_j}\right)} \quad (3)$$

According to the kinetic theory of gases, viscosity depends only on temperature. Noting also that

$$P_{ij}^{(1)} = -2\mu(\overline{\partial u_i/\partial x_j}) \quad (4)$$

is the first-order Navier-Stokes approximation for the stress tensor, one rewrites Eq. (3) as

$$P_{ij}^{(2)} - P_{ij}^{(1)} = 2\frac{\mu^2}{p}\frac{D}{Dt}\left(\overline{\frac{\partial u_i}{\partial x_j}}\right) + 2\frac{\mu^2}{p}\frac{\theta}{\mu}\frac{du}{d\theta}\frac{D\theta}{Dt}\overline{\frac{\partial u_i}{\partial x_j}} + 2\frac{\mu^2}{p}\overline{\frac{\partial u_k}{\partial x_k}}\overline{\frac{\partial u_i}{\partial x_j}} + 2\frac{\mu^2}{p}\left(\overline{\frac{\partial u_k}{\partial x_i}}\overline{\frac{\partial u_j}{\partial x_k}} + \overline{\frac{\partial u_k}{\partial x_j}}\overline{\frac{\partial u_i}{\partial x_k}}\right) - \frac{4\mu^2}{3p}\overline{\frac{\partial u_k}{\partial x_l}}\overline{\frac{\partial u_k}{\partial x_l}}\delta_{ij} + 3\frac{\mu^2}{\rho\theta}\overline{\frac{\partial^2\theta}{\partial x_i\partial x_j}} + 3\frac{\mu^2}{\rho\theta^2}\frac{\theta}{\mu}\frac{d\mu}{d\theta}\overline{\frac{\partial\theta}{\partial x_i}}\overline{\frac{\partial\theta}{\partial x_j}} \quad (5)$$

Now, all terms in Eq. (5) are of the second order—namely, $\mu^2$. To be consistent, one introduces the zero-order Euler Equations to compute $(D/Dt)(\partial u_i/\partial x_j)$ and $D\theta/Dt$ in the first and second terms of Eq. (5). From the momentum equation

$$(\partial u/\partial t) + u_k(\partial u_i/\partial x_k) + (1/\rho)(\partial p/\partial x_i) = 0$$

we have

$$D/Dt(\overline{\partial u_i/\partial x_j}) = -\overline{(\partial/\partial x_i)[(1/\rho)(\partial\rho/\partial x_j)]} - \overline{(\partial u_k/\partial x_j)(\partial u_i/\partial x_k)} \quad (6)$$

From the continuity equation,

† This work was carried out under Contract AF 18(600)993, sponsored by the Office of Scientific Research, Air Research and Development Command, and under the supervision of Professor J. M. Burgers.

* Research Associate.

The author wishes to thank Dr. F. S. Sherman for indicating minor errors in the computation.

$$(\partial\rho/\partial t) + (\partial/\partial x_k)(\rho u_k) = 0$$

the energy equation for a monatomic gas,

$$(\partial p/\partial t) + u_k(\partial p/\partial x_k) + (5/3)p(\partial u_k/\partial x_k) = 0$$

and the equation of state, with $R$ denoting the gas constant, $p = \rho R\theta$, we have

$$(D\theta/Dt) = -(2/3)\theta(\partial u_k/\partial x_k) \tag{7}$$

The fourth and fifth terms in Eq. (5) may be combined as

$$\left.\begin{aligned} &2(\mu^2/p)\,[\overline{(\partial u_k/\partial x_i)}\,\overline{(\partial u_j/\partial x_k)} + \overline{(\partial u_k/\partial x_j)}\,\overline{(\partial u_i/\partial x_k)}] - (4\mu^2/3p)\,\overline{(\partial u_k/\partial x_l)}\,\overline{(\partial u_k/\partial x_l)}\delta_{ij} \\ &= 4(\mu^2/p)\,\overline{(\partial u_k/\partial x_i)}\,\overline{(\partial u_j/\partial x_k)} + (4\mu^2/9p)\,\overline{(\partial u_k/\partial x_k)}\,\overline{(\partial u_l/\partial x_l)}\delta_{ij} \\ &= 4(\mu^2/p)\,\overline{(\partial u_k/\partial x_i)}\,\overline{(\partial u_j/\partial x_k)} \\ &= (\mu^2/p)\,[8\overline{(\partial u_k/\partial x_i)}\,\overline{(\partial u_k/\partial x_j)} + (8/3)\,\overline{(\partial u_i/\partial x_j)}\,\overline{(\partial u_k/\partial x_k)} - 4\overline{(\partial u_i/\partial x_k)}\,\overline{(\partial u_k/\partial x_j)}] \end{aligned}\right\} \tag{8}$$

since $\overline{\partial u_k/\partial x_k} = 0$.

Substituting Eqs. (6)–(8) into Eq. (5) and rearranging terms, we finally have

$$P_{ij}^{(2)} - P_{ij}^{(1)} = \frac{4}{3}\left(\frac{7}{2} - \frac{\theta}{\mu}\frac{du}{d\theta}\right)\frac{\mu^2}{p}\overline{\frac{\partial u_k}{\partial x_k}\frac{\partial u_i}{\partial x_j}} + 2\frac{\mu^2}{p}\left[-\overline{\frac{\partial}{\partial x_i}\left(\frac{1}{\rho}\frac{\partial p}{\partial x_j}\right)} - \overline{\frac{\partial u_k}{\partial x_i}\frac{\partial u_j}{\partial x_k}} - 2\overline{\frac{\partial u_i}{\partial x_k}\frac{\partial u_k}{\partial x_j}}\right] +$$
$$3\frac{\mu^2}{\rho\theta}\overline{\frac{\partial^2\theta}{\partial x_i\partial x_j}} + 0\,\frac{\mu^2}{\rho p\theta}\overline{\frac{\partial p}{\partial x_i}\frac{\partial\theta}{\partial x_j}} + 3\frac{\theta}{\mu}\frac{d\mu}{d\theta}\frac{\mu^2}{\rho\theta^2}\overline{\frac{\partial\theta}{\partial x_i}\frac{\partial\theta}{\partial x_j}} + 8\frac{\mu^2}{p}\overline{\frac{\partial u_i}{\partial x_k}\frac{\partial u_k}{\partial x_j}} \tag{9}$$

which is exactly the Burnett expression for the stress tensor for Maxwellian molecules given in references 2 and 3.

The second-order expression for the heat flux, $h_i$, given by Eq. (11.1) of reference 1 is

$$h_i^{(2)} = -\alpha\mu\theta_{,i} + (3\alpha\mu/2p)\,(\mu\theta_{,j})^{\cdot} + (\alpha\mu^2/2p)\,(5\theta_{,i}E + 3\theta_{,j}u_{i,j} + 8\theta_{,j}E_{ij}) + 3(\mu/\rho)\,(\mu E_{ij})_{,j} -$$
$$3(\mu^2/p\rho)\,E_{ij}p_{,j} + (15\mu/2\rho\theta)\,(\mu\theta\dot{\beta})_{,i} + (12\mu/7p)\,[(\mu^2/\rho)E_{ij}E_{jk}]_{,k} + (3\mu/7p)\,[(\mu^2/\rho)E_{jk}E_{jk}]_{,i} + (6\mu^2/p\rho)E_{ij}(\mu E_{jk})_{,k} \tag{10}$$

where

$$\alpha \equiv (15/4)R$$
$$\beta \equiv (3/2)\ln p\rho^{-5/3}$$

Noting that

$$h_i^{(1)} = -\alpha\mu\theta_{,i} = -(15/4)R\mu(\partial\theta/\partial x_i) \tag{11}$$

is the first-order Navier-Stokes approximation for the heat flux, $\dot{\beta} = (3/2)\,(D/Dt)\ln p\rho^{-5/3} = 0$ in Euler's approximation, and that the last three terms of Eq. (10) are of the third order we rewrite Eq. (10) as, keeping only $\mu^2$ terms,

$$h_i^{(2)} - h_i^{(1)} = \frac{45}{8}\frac{\mu^2}{\rho\theta}\left[\frac{D}{Dt}\left(\frac{\partial\theta}{\partial x_i}\right) + \frac{1}{\mu}\frac{d\mu}{d\theta}\overline{\frac{D\theta}{Dt}\frac{\partial\theta}{\partial x_i}}\right] +$$
$$\frac{15}{8}\frac{\mu}{\rho\theta}\left(5\overline{\frac{\partial\theta}{\partial x_i}\frac{\partial u_j}{\partial x_j}} + 3\overline{\frac{\partial\theta}{\partial x_j}\frac{\partial u_i}{\partial x_j}} + 8\overline{\frac{\partial\theta}{\partial x_j}\frac{\partial u_i}{\partial x_j}}\right) +$$
$$3\frac{\mu^2}{\rho}\left[\frac{\partial}{\partial x_j}\left(\frac{\partial u_i}{\partial x_j}\right) + \frac{1}{\mu}\frac{d\mu}{d\theta}\overline{\frac{\partial\theta}{\partial x_j}\frac{\partial u_i}{\partial x_j}}\right] - 3\frac{\mu^2}{p\rho}\overline{\frac{\partial u_i}{\partial x_j}\frac{\partial p}{\partial x_j}} \tag{12}$$

Now

$$(D/Dt)\,(\partial\theta/\partial x_i) = (\partial/\partial x_i)\,(D\theta/Dt) - (\partial u_j/\partial x_i)\,(\partial\theta/\partial x_j) \tag{13}$$

$$(1/2)\,[(\partial u_j/\partial x_i) + (\partial u_i/\partial x_j)]\,(\partial\theta/\partial x_j) =$$
$$\overline{(\partial u_i/\partial x_j)}\,\overline{(\partial\theta/\partial x_j)} + (1/3)\,\overline{(\partial u_j/\partial x_j)}\,\overline{(\partial\theta/\partial x_i)} \tag{14}$$

Substituting Eqs. (7) and (13) into Eq. (12), we have finally, using Eq. (14) and rearranging terms,

$$h_i^{(2)} - h_i^{(1)} = (15/4)\,[(7/2) - (\theta/\mu)\,(d\mu/d\theta)] \times$$
$$(\mu^2/\rho\theta)\,\overline{(\partial u_j/\partial x_i)}\,\overline{(\partial\theta/\partial x_i)} - (45/8)\,(\mu^2/\rho\theta) \times$$
$$\{(2/3)\,(\partial/\partial x_i)\,[\theta(\partial u_j/\partial x_j)] + 2\overline{(\partial u_j/\partial x_i)}\,\overline{(\partial\theta/\partial x_j)}\} +$$
$$\{-3(\mu^2/p\rho)\,(\partial p/\partial x_i) + 3(\mu^2/\rho)\,(\partial/\partial x_i) +$$
$$3[(35/4) + (\theta/\mu)\,(d\mu/d\theta)]\,(\mu/\rho\theta)\,\overline{(\partial\theta/\partial x_j)}\}\,\overline{(\partial u_j/\partial x_i)} \tag{15}$$

which is exactly the Burnett expression for the heat flux for Maxwellian molecules given in references 2 and 3.

At this point, it is of interest to mention that the Grad thirteen-moment equations[4] can also be shown to include the exact Burnett expressions (9) and (15). This was first established by S. A. Schaaf and F. S. Sherman by the method of iteration and was carried out independently by T. Y. Li and the present author by the method of series expansion.

Based on the above observations, the Burnett equations may be considered as an approximation to the Ikenberry-Truesdell equations as well as to the Grad equations. It may then be concluded that the latter two systems are better fitted to describe the slip flow regime than the Burnett equations. However, to apply the Ikenberry-Truesdell equations to problems in rarefied gas dynamics, the appropriate boundary conditions must first be developed.

### References


[1] Ikenberry, E., and Truesdell, C., *On the Pressures and the Flux of Energy in a Gas According to Maxwell's Kinetic Theory, I*, J. Rational Mech. & Analysis, Vol. 5, No. 1, pp. 1–54, January, 1956.

[2] Wang Chang, C. S., and Uhlenbeck, G. E., *On the Transport Phenomena in Rarefied Gases*, CM-443, Appl. Phys. Lab., The Johns Hopkins Univ., February, 1948; Correction by Wang Chang, CM-467, May, 1948.

[3] Lin, T. C., and Street, R. E., *Effect of Variable Viscosity and Thermal Conductivity on High-Speed Flow between Concentric Cylinders*, NACA TR1175, 1954.

[4] Grad, H., *On the Kinetic Theory of Rarefied Gases*, Communications on Pure & Applied Math., Vol. 2, No. 4, pp. 331–407, December, 1949.


## On Hypersonic Stagnation-Point Flow With a Magnetic Field*


Nelson H. Kemp
*Senior Scientist, Avco Research Laboratory, Everett, Mass.*


March 5, 1958

### Introduction

Interest has recently arisen in magnetohydrodynamic effects in high-speed flight, especially at the nose of blunt bodies where ionization and gas conductivity are likely to be large enough so that a magnetic field can affect the flow. That these effects might be useful in decreasing heat transfer and increasing pressure drag for re-entry bodies was suggested in reference 1 and pointed out again in reference 2. In reference 3 the reduction in heat-transfer rate to a plane stagnation point with a normal magnetic field in a conducting compressible flow is investigated. There it is shown that for a given inviscid flow the presence of a moderate magnetic field causes the heat-transfer rate *in the viscous layer* to increase, but only by a few per cent. The change in the

* This work was sponsored by the U.S. Air Force, ARDC, partly under Contract AF 04(645)-18 with the Ballistic Missile Division and partly under Contract AF 49(638)-61 with the Office of Scientific Research.

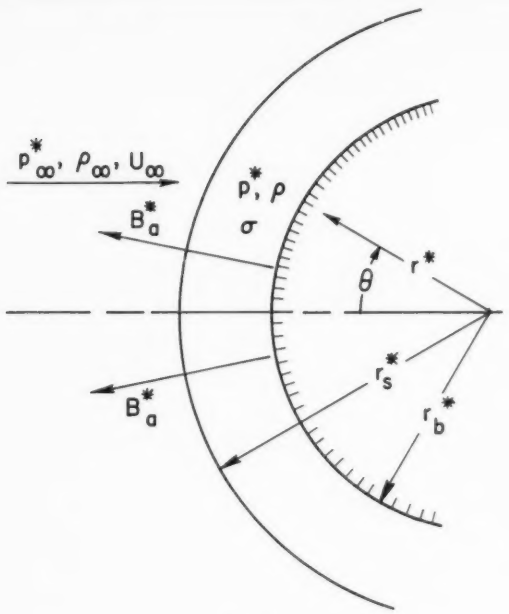


FIG. 1.

*inviscid flow* due to a magnetic field is investigated for large magnetic Reynolds Number $R_m$ and is found to lead to decreases of heat-transfer rate up to 30 per cent. However, the practically interesting case for hypersonic flight is the opposite one of small $R_m$, which is mentioned but not considered in reference 3. In reference 4 a similar problem is investigated for incompressible flow, but only shear stress is found. Unfortunately, the results of reference 4 are clouded because the authors compared the case with a magnetic field to the case without a field but with the same *inviscid pressure distribution*. This comparison is not realistic, since for given flight conditions, the field definitely changes the pressure distribution, as will be shown below.

The purpose of this note is to present the effect of a magnetic field on the inviscid flow at the stagnation point of a blunt axisymmetric body in the practical case of small magnetic Reynolds Number. In view of the conclusions of reference 2, that the main effect of the field is to change the inviscid rather than the viscous flow, this will make possible a prediction of the change in heat transfer and pressure drag caused by the field. The method used to analyze the flow is that introduced by Lighthill,[5] where a spherical shock shape and incompressible flow are assumed.

## ANALYSIS

The blunt body is shown in Fig. 1 in a stream of velocity $U_\infty$ and density $\rho_\infty$. Near the stagnation point it is taken as a sphere of radius $r_b^*$, producing a spherical shock of radius $r_s^*$, behind which there is an incompressible flow of density $\rho$ and constant conductivity $\sigma$. The applied magnetic field $\boldsymbol{B}_a^*$ is taken to be in the radial direction only and spherical coordinates $r^*$ and $\theta$ are used.

The governing magnetohydrodynamic equations relate the magnetic field $\boldsymbol{B}^*$, velocity $\boldsymbol{q}^*$, pressure $p^*$, electric-current density $\boldsymbol{j}^*$, electric field $\boldsymbol{E}^*$, and vorticity $\Omega^* = \nabla \times \boldsymbol{q}^*$. They may be found, for example, in references 2 or 4. If the equations are made dimensionless, using a length $L$, velocity $U_\infty$, density $\rho_\infty$, field $B_0^*$, and conductivity $\sigma$, we find the following steady-state equations for the dimensionless quantities (without asterisks):

$$\nabla(kp + q^2/2) - \boldsymbol{q} \times \Omega = Sk\boldsymbol{j} \times \boldsymbol{B} \tag{1a}$$

$$\nabla \cdot \boldsymbol{q} = 0 \tag{1b}$$

$$= \boldsymbol{E} + \boldsymbol{q} \times \boldsymbol{B} \tag{2a}$$

$$\nabla \cdot \boldsymbol{j} = 0 \tag{2b}$$

$$\nabla \times \boldsymbol{E} = 0 \tag{3a}$$

$$\nabla \cdot \boldsymbol{B} = 0 \tag{3b}$$

$$\nabla \times \boldsymbol{B} = R_m \boldsymbol{j} \tag{3c}$$

The dimensionless numbers $k$, $R_m$ and $S$ are

$$k \equiv \rho_\infty/\rho, \qquad R_m \equiv \mu_e \sigma U_\infty L, \qquad S \equiv \sigma(B_0^*)^2 L/\rho_\infty U_\infty \tag{4}$$

Here $\mu_e$ is the magnetic permeability, and $k$ is the density ratio across the shock, which is the only parameter in the case of zero field. $R_m$ is called the magnetic Reynolds Number, in analogy with the usual viscous Reynolds Number. It is discussed, for example, in references 2 and 3, where it is shown to be of order 0.1 or less for hypersonic flight conditions. $S$ is a frequently used but as yet nameless quantity representing the ratio of the magnetic body force to the dynamic pressure.[2] Unlike $R_m$, it contains the field strength and so its magnitude depends on the applied field.

For the practically important case of small $R_m$, Eq. (3c) may be written $\nabla \times \boldsymbol{B} = 0$, indicating that the currents flowing in the gas do not affect the magnetic field, and thus the applied magnetic field is undistorted by the flow. Therefore, the $\boldsymbol{B}$ field may be considered given, greatly simplifying the problem. Furthermore, considerations of axial symmetry combined with Eqs. (2) and (3a) show that there is no $\boldsymbol{E}$ field provided the body is an insulator or an equipotential surface. These two results have the effect of completely uncoupling Eqs. (1) from Eqs. (2) and (3), leaving

$$\nabla(kp + q^2/2) - \boldsymbol{q} \times \Omega = Sk(\boldsymbol{q} \times \boldsymbol{B}_a) \times \boldsymbol{B}_a \tag{5a}$$

$$\nabla \cdot \boldsymbol{q} = 0 \tag{5b}$$

where $\boldsymbol{B}_a$ is the applied field, which in the region of the stagnation point consists of only one component $B_r$, in the $r$ direction. To satisfy $\nabla \cdot \boldsymbol{B}_a = 0$ it must have the form $B_r = C/r^2$ where $C$ is a constant.

The pressure is eliminated by taking the curl of Eq. (5a), and a stream function identical to Lighthill's[5] is introduced to satisfy Eq. (5b). When $B_r$ and this stream function are put into the curl of Eq. (5a) the following differential equation results:

$$2 \sin\theta \cos\theta \Psi \, (d/dr)\{(1/r^2)\,[(2\Psi/r^2) - \Psi'']\} = -kSC^2 \sin\theta (d/dr)(\Psi'/r) \tag{6}$$

The primes denote differentiation with respect to $r$.

In the nonmagnetic case $S = 0$, Eq. (6) becomes an ordinary linear equation for $\Psi(r)$ for all $\theta$ and can be solved explicitly.[5] In the present case it becomes an ordinary nonlinear equation at the stagnation point, $\theta = 0$.

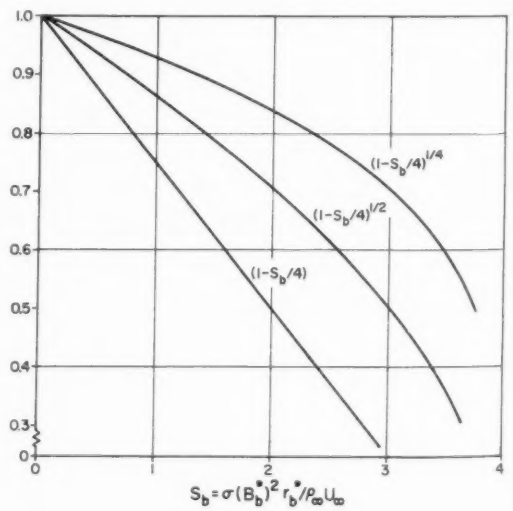


FIG. 2.

The boundary conditions are found from the ordinary Rankine-Hugoniot equations and the $\theta$ component of Eq. (5a) at the spherical shock $r = r_s$.

A numerical solution of Eq. (6) for $\theta = 0$ could be found. However, in order to illustrate the effect of moderate fields, a series solution was found in powers of the small density ratio $k$. If we assume that

$$S_b \equiv \sigma(B_b^*)^2 r_b^*/\rho_\infty U_\infty^* = 0(1)$$

we find, for detachment distance $\delta$ and stagnation-point velocity gradient,

$$(\delta/kr_b) - 1 = -\tfrac{1}{4}(8/3)k[1 - (1/4)S_b]^{-1/2} \quad (7a)$$

$$(\partial v_\theta/\partial\vartheta)_{s\ell} = +(\Psi_b'/r_b) = [(8/3)k[1 - (1/4)S_b]^{1/2} \quad (7b)$$

For $S_b = 0$ this agrees with Lighthill's results to this order in $k$.

The pressure on the body is obtained by returning to Eqs. (5a) and using Eq. (7b). The result is

$$p_b - p_{s\ell} = -(1/2)(\Psi_b'/r_b)^2 k^{-1}[1 + (kS_b/r_b^{-1}\Psi_b')] \sin^2\theta = -(4/3)[1 - (1/4)S_b](1 + \lambda)\sin^2\theta \quad (8)$$

where $\lambda \equiv \sigma(B_b^*)^2/\rho(\partial v_\theta/\partial\theta)_{s\ell}$ is the same parameter used by Meyer[3] and denoted in reference 4 by $h^2(0)/\gamma$. The stagnation pressure $p_{s\ell}$ is, of course, not affected by the field, since along the stagnation streamline from the shock to the body the field and velocity are parallel, so the induced current and, therefore, the magnetic body force are zero. The form of Eq. (8) is the same as that given for pressure in reference 4, but here we have calculated the velocity gradient from the given flow conditions instead of relating it to some unknown nonmagnetic flow.

## Discussion

The results in Eqs. (7) and (8) show to what extent a moderate magnetic field normal to the body can affect the stagnation-point flow. The shock is pushed outward, but only in the second term in $k$. The detachment distance is still of basic order $k$, as it must be from continuity considerations. The velocity gradient is decreased in its lowest order by the factor $(1 - S_b/4)^{1/2}$. Since the heat-transfer rate depends primarily[5] on the square root of the velocity gradient, we see that it can be reduced by a factor $(1 - S_b/4)^{1/4}$. These two factors are plotted in Fig. 2.

To orient oneself, note that for a typical missile case of flight at satellite velocity at 100,000 ft, with a field of $10^4$ gauss, a radius of 1 meter, and a conductivity of 100 mho/m, $S_b = 2/3$. The reduction in stagnation-point heat-transfer rate is then only about 5 per cent. It therefore appears that very large fields would be necessary to give appreciable reductions in heat transfer for missiles. The pressure increase is somewhat larger, being proportional to $(1 - S_b/4)$. This factor is also shown in Fig. 2. A rough estimate of the pressure-drag change, obtained by integrating Eq. (8) for a sphere up to the angle where $p_b$ vanishes, shows that the drag increases by a factor $[(1 - S_b/4)(1 + \lambda)]^{-1}$. For the missile case quoted above, where $k = 1/15$, this factor is only 1.05, so again the pressure-drag increase is quite small, though the calculation is admittedly very crude since the present theory does not extend far from the stagnation point. All in all, it would not appear that the sort of geometry considered here is suitable for obtaining significant effects near the stagnation points of missiles. The situation is, of course, more favorable for larger bodies at higher altitudes, where $S_b$ can be larger. Fields may be useful for returning satellites, for example. Also, it should be noted that the field geometry of this present theory may not be best for obtaining overall changes in heat transfer and drag.

## References


[1] Rosa, R. J., *Engineering Magneto-Hydrodynamics*, Part 2 of Ph.D. Thesis, Cornell University, 1956 (available from University Microfilms, Ann Arbor, Mich.).

See also Patrick, R. M., *Magneto-Hydrodynamics of Compressible Fluids*, Ph.D. Thesis, Cornell University, 1956 (available from University Microfilms, Ann Arbor, Mich.).

[2] Resler, E. L., Jr., and Sears, W. R., *The Prospects for Magneto-Aerodynamics*, Journal of the Aeronautical Sciences, Vol. 25, No. 4, pp. 235–245, April, 1958.

[3] Meyer, R. C., *On Reducing Aerodynamic Heat Transfer Rates by Magneto-hydrodynamic Techniques*, Preprint No. 816, Institute of the Aeronautical Sciences, January, 1958.

[4] Neuringer, J. L., and Mellroy, W., *Incompressible Two-Dimensional Stagnation-Point Flow of an Electrically Conducting Viscous Fluid in the Presence of a Magnetic Field*, Journal of the Aeronautical Sciences, Vol. 25, No. 3, pp. 194–192, March, 1958.

[5] Lighthill, M. J., *Dynamics of a Dissociating Gas. Part I: Equilibrium*, Journal of Fluid Mechanics, Vol. 2, Part 1, pp. 28–31, January, 1957.


# Note on the Stabilizing Effect of Centrifugal Forces on the Laminar Boundary Layer Over Convex Surfaces*


Lester Lees

*Professor of Aeronautics, California Institute of Technology, Pasadena, Calif., and Consultant, The Ramo-Wooldridge Corporation, Los Angeles, Calif.*


March 7, 1958

At high supersonic flight speeds or with a highly cooled surface, there is a strong density gradient across the boundary layer. Close to the surface the gas is cool and of low-temperature molecular weight; at the outer edge of the boundary layer, the gas is hot and may be partially dissociated so that its density is lower by a factor of 10–20. At the same time a strong centrifugal acceleration is produced by the body curvature (see Fig. 1), and this outward acceleration acts in the direction of decreasing density. The question arises whether this destabilizing effect of the acceleration field in a density gradient is sufficient to overcome the stabilizing effect of the increasing angular momentum of the fluid in the outward direction. The conclusion of this brief note is that the strong stabilizing effect of the outward increase in angular momentum is always dominant in the laminar boundary layer.

First of all, we recognize that the gravitational field is so much smaller than the centrifugal acceleration field that it may safely be neglected. For example, even if the velocity along the surface is as small as 100 ft./sec. and the body radius is 1 ft., the centrifugal acceleration is $10^4$ ft./sec.$^2$, or about 300g. Therefore, this analysis is confined to the effect of centrifugal forces alone. A similar remark applies to the acceleration or deceleration experienced by the body in flight.

Von Kármán[1] gave a very clear physical description of the stability or instability of revolving fluids. In the steady state, the centrifugal force $(\rho_1 u_1^2)/(r_1)$ at each location must be balanced by the radial pressure gradient. If a fluid particle at $r_1$ is displaced to a larger radius $r_2$, the centrifugal force acting on the particle becomes $(\tilde{\rho}_1 \tilde{u}_1^2)/r_2$, where $\tilde{\rho}_1$ and $\tilde{u}_1$ are the new values of density and tangential velocity for the fluid particle. But

* Originally issued for limited distribution as Ramo-Wooldridge Report No. GM-TR-118, December 14, 1956.

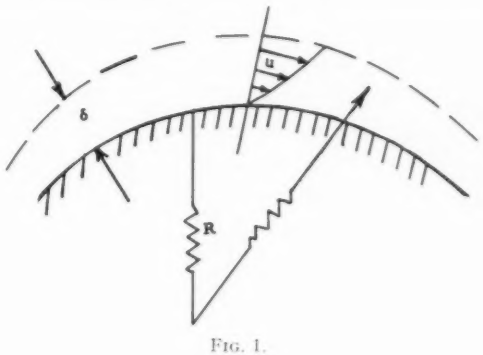


Fig. 1.

the angular momentum of a fluid particle is preserved so that $r_2\tilde{u}_1 = r_1 u_1$, and the centrifugal force is now $\tilde{\rho}_1[(r_1^2 u_1^2)/r_2^3]$. If this force is larger than the prevailing pressure gradient $\rho_2(u_2^2/r_2)$, or if $\tilde{\rho}_1 r_1^2 u_1^2 > \rho_2 u_2^2 r_2^2$, the fluid element will continue its motion outward and the motion is unstable. On the other hand, if $\tilde{\rho}_1 r_1^2 u_1^2 < \rho_2 u_2^2 r_2^2$, the motion is dynamically stable.

In von Kármán's original analysis the density of the fluid is uniform, so that $\tilde{\rho}_1 = \rho_2 = \rho_1$, and the famous Rayleigh criterion is obtained—i.e.,

$$\begin{matrix} dk^2/dr < 0 & \text{unstable} \\ > 0 & \text{stable} \end{matrix}$$

where $k^2 = (ru)^2$ is the square of the angular momentum. In general, the new density of the fluid particle $\tilde{\rho}_1$ is almost certainly different from $\rho_1$, but the strongest destabilizing effect is obtained if we take $\tilde{\rho}_1 = \rho_1$, because $\rho_1 > \rho_2$ here. *Then the new criterion reads*

$$\begin{matrix} d/dr(\rho\, u^2 r^2) < 0 & \text{unstable} \\ > 0 & \text{stable} \end{matrix}$$

or

$$\rho\, ur^2\left\{2[(\partial u/\partial r) + (u/r)] + (u/\rho)(\partial\rho/\partial r)\right\} \begin{matrix} <0 & \text{unstable} \\ >0 & \text{stable} \end{matrix} \quad (1)\dagger$$

In the case of the laminar boundary layer over a highly cooled, blunt, convex body, the radial coordinate is $r = R + y$ where $y$ is the distance normal to the surface and $\delta/R \ll 1$. (See Fig. 1.) Now the density in the boundary layer is given approximately by $\rho_e/\rho \cong h/h_e$, where $h$ is the enthalpy, or

$$(u/\rho)(\partial\rho/\partial r) = -(u/h)(\partial h/\partial r)$$

But when $\rho_e/\rho_w \ll 1$, a good approximation to the enthalpy distribution is given by the simple relation $h \cong h_w + (h_e - h_w)(u/u_e)$ where the subscript $w$ refers to surface conditions, and the subscript $e$ refers to conditions at the outer edge of the boundary layer. Therefore,

$$(u/h)(\partial h/\partial r) = (u/h)(\partial h/\partial y) = \left\{(h_e - h_w)(u/u_e)/[h_w + (h_e - h_w)(u/u_e)]\right\}(\partial u/\partial y)$$

and the quantity in the braces in Eq. (1) becomes

$$\left[\frac{\partial u}{\partial y}\left\{2 - \frac{(h_e - h_w)(u/u_e)}{h_w + (h_e - h_w)(u/u_e)}\right\} + \frac{2u}{R + y}\right]$$

Now the quantity

$$(h_e - h_w)(u/u_e)/[h_w + (h_e - h_w)(u/u_e)]$$

is never larger than unity, so long as $h_w < h_e$, and the quantity $2u/(R + y)$ is always positive (but negligibly small). Also $\partial u/\partial y > 0$. We conclude therefore that the criterion for dynamic stability given by Eq. (1) is always satisfied in this case.

It must be emphasized that this analysis is not meant to apply in the immediate vicinity of the forward stagnation point where the streamline curvature of the inviscid flow outside the boundary layer is concave, and the dynamic instability may be significant.

### References


[1] von Kármán, Th., *Some Aspects of the Turbulence Problem*, Proc. 4th International Congress for Applied Mechanics, Cambridge, England, pp. 54–91, July 3–9, 1934.

[2] Synge, J. L., *The Stability of Heterogeneous Liquids*, Trans. Roy. Soc., Canada, Vol. 27, Section 3, Series 3, pp. 1–18, May, 1933.

[3] Lessen, M., *On the Hydrodynamic Stability of Curved Laminar Compressible Flows*, Paper presented at the Aerodynamics Session, IAS 26th Annual Meeting, N.Y., January 27–30, 1958. IAS Preprint No. 812.


† This criterion is identical with the result obtained by Synge[2] for liquids by applying the Sturm-Liouville oscillation theorem to the differential equation for small disturbances in a laminar motion. In his case $d\rho/dt = 0$, and $\tilde{\rho}_1$ is in fact equal to $\rho_1$. An analysis for a gas with arbitrary Mach Number is now being made but is not expected to change these results very much. This result can also be shown to be identical with Eq. (35) of the recent paper by M. Lessen.[3]

## An Evaluation of the Criticisms by Topping of Marin's Strength Hypothesis


John J. Coleman

*Mathematical Analysis and Operations Research Group, Electro Dynamics Staff, Transport Division, Boeing Airplane Company, Renton, Wash.*


March 7, 1958

PROFESSOR MARIN STATED that his proposed theory of failure of materials under combined stress was a generalization of the octahedral shear stress theory[2]

$$(\sigma_1 - \sigma_2)^2 + (\sigma_1 - \sigma_3)^2 + (\sigma_3 - \sigma_1)^2 = 9\tau_0^2 \quad (1)$$

where $\sigma_1$, $\sigma_2$, $\sigma_3$ are principal stresses and $\tau_0$ is the octahedral shear stress.

Marin's relation states

$$(\sigma_1 - a)^2 + (\sigma_2 - b)^2 + (\sigma_3 - c)^2 + q[(\sigma_1 - a)(\sigma_2 - b) + (\sigma_2 - b)(\sigma_3 - c) + (\sigma_3 - c)(\sigma_1 - a)] = \sigma_0^2 \quad (2)$$

where $\sigma_0^2$ is a constant of the material, and $a$, $b$, $c$, and $q$ are also constants.

In his note,[1] Topping tried to show, by demonstrating its shortcomings, that Marin's proposal is untenable for various values of $q$. Unfortunately, all present theories of failure for combined stress have shortcomings of one kind or another.

Topping's insistence that Marin's Eq. (2) fit all the restrictions imposed from known behavior of materials under all conditions of failure seems overcritical. However, the imposed restrictions mentioned by Topping do restrict the value of $q$ to less than $-1$. In general, Marin's formula then satisfies the conditions for unequal tensile and compressive strengths, anisotropy, and the features that the limiting failure surfaces must be open at the compression end and closed at the tension end of the hydrostatic stress axis. The last set of features also include the fact that failure is affected by hydrostatic pressure.

Strictly speaking, if all points on the yield surface represented by Marin's Equation for $q < -1$ represent the condition of yielding, it appears to contradict the experimental facts because the state of hydrostatic tension of three equal tensile stresses, under which a material cannot yield, would correspond to such a point. However, a second surface, distinct from the yielding surface, must exist—namely, the surface of rupture. One can assume that the yield surface encloses the rupture surface beyond a common intersection curve in the positive quadrant. A geometrical situation such as this would account for rupture occurring before yielding in the case of triaxial tension. Consequently, the hyperboloid of one sheet, defined by $q < -1$, may be applicable after all.

In conclusion, one must say that Topping performed a service for Professor Marin in determining the restrictions on $q$. However, Topping's arguments did not make Eq. (2) untenable for the case $q < -1$. In fact, this case demands the existence of two limiting surfaces for triaxial tension. Similar mathematical expressions might be used to define both. The seriousness of any shortcomings should be judged in the light of the usefulness of the proposed theory in providing adequate design criterion. Furthermore, the proposed theory should be compared with test results before any final judgment can be made.

### References


[1] Topping, A. D., *Marin's Strength Hypothesis*, Journal of the Aeronautical Sciences, Readers' Forum, Vol. 25, No. 1, pp. 59, 60, January, 1958.

[2] Marin, J., *Theories of Strength for Combined Stresses and Nonisotropic Materials*, Journal of the Aeronautical Sciences, Vol. 24, No. 4, pp. 265–268, 274, April, 1957.



**Change of Address**

It is important that the Institute be notified of changes in address 30 days in advance of publishing date to ensure receipt of every issue of the JOURNAL and AERO/SPACE ENGINEERING. Notices should be sent directly to:

**Institute of the Aeronautical Sciences, Inc.**
**2 East 64th Street, New York 21, N.Y.**